Max-Planck Institut für Kolloid- und Grenzflächenforschung
Theorie und Bio-Systeme

Cooperative behavior of motor proteins

Dissertation
zur Erlangung des akademischen Grades
"doctor rerum naturalium"
(Dr. rer. nat.)
in der Wissenschaftsdisziplin Analytische Biochemie

eingereicht an der
Mathematisch-Naturwissenschaftlichen Fakultät
der Universität Potsdam

von
Janina Beeg

Potsdam, im April 2007

Zusammenfassung

Kinesin-1 (konventionelles Kinesin) ist ein Motorprotein des Zytoskeletts, das für den schnellen intrazellulären Lastentransport auf Mikrotubuli verantwortlich ist. Das Hauptinteresse vieler Studien lag bisher auf der Erforschung der Transporteigenschaften von Einzelmotormolekülen. Der Transport in der Zelle erfordert aber gewöhnlich kollektive Arbeit von mehreren Motoren.

In dieser Arbeit wurde die Bewegung von Kugeln als Modell für Zellorganellen, die von Kinesin-1 Molekülen gezogen werden, in Anhängigkeit von der Motorendichte auf der Kugeloberfläche und unterschiedlichen Kugeldurchmessern *in vitro* untersuchten. Die Transportparameter Weglänge, Geschwindigkeit und die erzeugte Kraft wurden gemessen.

Die Ergebnisse zeigen, dass die Transportgeschwindigkeit leicht abnimmt, wohingegen die Weglänge und die erzeugten Kräfte mit steigender Molekülkonzentration zunehmen. Die tatsächliche Anzahl der Motoren, die aktiv am Transport der Kugeln beteiligt sind, wurde bestimmt, indem die Änderung des hydrodynamischen Durchmessers der mit Kinesin bedeckten Kugeln mittels dynamischer Lichtstreuung gemessen wurde. Außerdem wurden sterische Effekte des verwendeten Transportsystems in die Berechnung einbezogen. Damit werden Ergebnisse vergleichbar, die für unterschiedliche Kugeldurchmesser und Motorkonzentrationen ermittelt wurden. Zusätzlich wurden die Verteilungen der Weglängen für die kleinste Kugelgröße mit theoretisch ermittelten Verteilungen verglichen. Letzteres ergab durchschnittliche Anzahlen der aktiv am Transport beteiligten Motormoleküle, die mit den experimentell bestimmten Ergebnissen übereinstimmen.

Abstract

The cytoskeletal motor protein kinesin-1 (conventional kinesin) is the fast carrier for intracellular cargo transport along microtubules. So far most studies aimed at investigating the transport properties of individual motor molecules. However, the transport in cells usually involves the collective work of more than one motor.

In the present work, we have studied the movement of beads as artificial loads/organelles pulled by several kinesin-1 motors *in vitro*. For a wide range of motor coverage of the beads and different bead (cargo) sizes the transport parameters walking distance or run length, velocity and force generation are measured.

The results indicate that the transport parameters are influenced by the number of motors carrying the bead. While the transport velocity slightly decreases, an increase in the run length was measured and higher forces are determined, when more motors are involved. The effective number of motors pulling a bead is estimated by measuring the change in the hydrodynamic diameter of kinesin-coated beads using dynamic light scattering. The geometrical constraints imposed by the transport system have been taken into account. Thus, results for beads of different size and motor-surface coverage could be compared. In addition, run length-distributions obtained for the smallest bead size were matched to theoretically calculated distributions. The latter yielded an average number of pulling motors, which is in agreement with the effective motor numbers determined experimentally.

Content

Chapter 1

Introduction

1.1 Organization and function of the cytoskeleton

The cytoskeleton is an important complex and highly dynamic three-dimensional cellular system of fibers extended throughout the cytoplasm of most eukaryotic cells. It provides cellular scaffolding and is essential for cell motility. This internal framework is responsible, e.g. for maintaining cell shape and mechanical strength, separation of chromosomes in mitosis and meiosis during cell division, and muscle contraction. In addition, it provides the machinery for intracellular movements like organelle transport. The three primary types of fibers are actin filaments, intermediate filaments and microtubules, see Figure 1.1-1. They are formed by different proteins.

Actin filaments, also called microfilaments are cable like, thin and flexible two-stranded helical polymers built from actin subunits. The monomeric actin is a globular protein (G-actin) and polymerizes in a uniformly oriented fashion to F-actin (filamentous actin). F-actin has a polar structure with a slow and a fast growing end. Within a cell, the assembly is regulated through actin-regulatory proteins such as actin bundling and actin cross-linking proteins. F-actin is responsible for cell shape changes, cell locomotion, and chemotactic migration and is most highly concentrated in the cell cortex. In addition, the filaments participate in muscle contraction, too.

Intermediate filaments (IFs), named because its diameter of approximately 10 nm is intermediate between the smaller actin filament (about 6 nm in diameter) and the lager microtubules, which are stable, rope-like structures composed of several intertwined protein strands. In contrast to the highly conserved globular actin and tubulin with nucleotide-binding and hydrolyzing activity, the intermediate filament protein (IFP) monomers are elongated fibrous molecules with no known enzymatic activity. IFs surround the nucleus in most animal cells and build a network throughout the periphery of the cell to interact with the plasma membrane. They are well expressed in cells that are exposed to mechanical stress and provide cell integrity.

Figure 1.1-1: The three types of filaments that form the cytoskeleton. The structure of each filament is shown in a schematic picture and in an electron micrograph. In addition, the distribution of each filament type throughout a certain type of epithelial cell is shown. [adapted from Alberts et al. 2002]

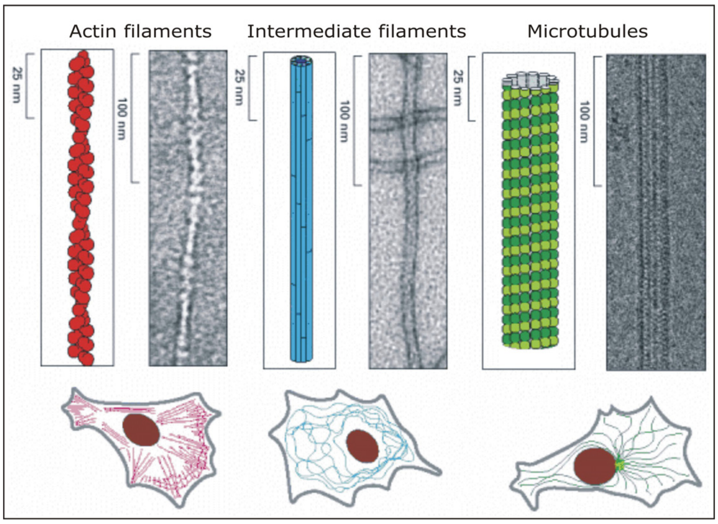

Microtubules have a polar structure like actin filaments and assemble in a uniform fashion from α/β-tubulin heterodimers (see Figure 1.1-2). The tubulin subunit is a GTPase that polymerizes to microtubules in the presence of guanosin triphosphate (GTP) and Mg^{2+}-ions that are catalyzing the GTPase. The tubulin dimers polymerize into linear protofilaments (head-to-tail interaction), which gives the polarity to the filaments. *In vivo*, most often 13 protofilaments associate laterally to form the microtubule [Tilney et al. 1973]. *In vitro* assembled microtubules possess a protofilament-diversity from 8 to 15 protofilaments per microtubule with a maximum in the frequency distribution of 14, 13, or 12 protofilaments in dependency on the assembly conditions [Unger et al. 1990]. In the case of 13 protofilaments per microtubule, they are arranged parallel to each other and to the long microtubule axis. The tubulin monomers in neighboring protofilaments are positioned in an α-to-α and β-to-β tubulin fashion, the so-called B lattice, with a relative shift of approximately 1 nm between the monomers. Observations of microtubule assembly *in vitro* have shown that elongated protofilament sheets close to form a cylindrical wall [Heald et al. 1996], which is required for the unidirectional transport. The microtubule has an outer diameter of 25 nm, an inner diameter of 14 nm and, depending on the reaction conditions, a typical length of 1 - 10 μm. In neuronal cells they can be even longer [Bray and Brunge 1981, Burton 1987]. Within the axons of nerve cells a high density of microtubules is found, because microtubules are required for axonal transport of cell organelles. In axons, the polymers are uniformly oriented in the same direction with their β-tubulin-terminated end pointing towards the axon terminals [Heidemann et al. 1981]. Thus, they build the tracks for long distance transport of cell organelles realized by the two microtubule-associated motor proteins kinesin and dynein.

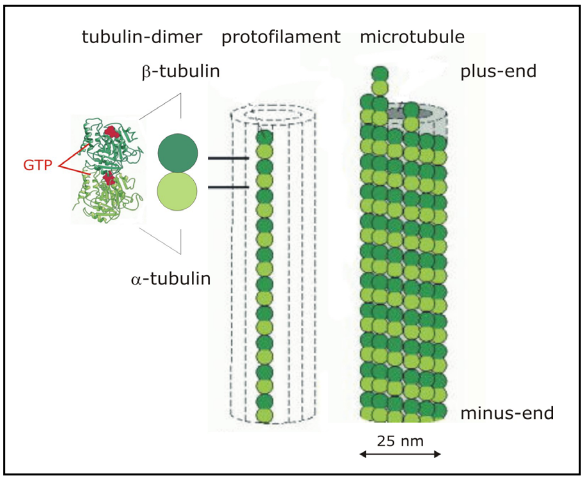

Figure 1.1-2: Structure of a microtubule and its subunit, the α/β-tubulin dimer. The tightly bound α/β-tubulin heterodimer builds the subunit of a microtubule, where the β-tubulin only hydrolyses the GTP during microtubule assembly. A protofilament is formed by adjacent tubulin dimers in a polar fashion. *In vivo*, 13 protofilaments build the hollow and tubelike microtubule. [adapted from Alberts et al. 2002]

In vitro, the purified tubulin polymerizes more quickly from the β-tubulin site, the so called "plus-end" of the microtubules (kinetically more dynamic end). The opposite and thus slow-growing site is terminated by the α-tubulin [Fan et al. 1996]. In cells the α-subunits are generally anchored to the microtubule-organizing centre (MTOC). The two main types of MTOCs are the basal bodies associated with cilia, and centrosomes. From the MTOC the microtubules grow out with their plus ends leading into the cytoplasm. This occurs for example during the assembly of the mitotic spindle during cell division [Heald et al. 1996].

Microtubule polymerization is a very dynamic process, characterized by constant elongation and rapid shrinking processes [Mitchison and Kirschner 1984]. During the growing phase, the tubulin dimers are added to the end of the polymer much faster than GTP-hydrolysis is triggered. In the opposite case, at faster GTP-hydrolysis a bend within the otherwise straight subunit is induced and the resulting GDP-microtubule becomes very unstable. The depolymerization process is initiated and tubulin subunits curl away from the filament [Mueller-Reichert et al. 1998, Wang and Nogales 2005].

Microtubule associated proteins (MAPs) promote the assembly and are known to stabilize microtubules both thermodynamically and kinetically. However, the MAPs bind to the microtubule wall and therefore interfere with the motor protein-transport. Thus, microtubule polymerization in the absence of MAPs is preferred for the observation of kinesin movement, *in vitro*. Consequently, the microtubules necessary for investigation of kinesin transport properties have to be stabilized, which is done usually by taxol or aldehyde fixation (for chemical fixation see section 2.2.3.2). The anticancer drug taxol was found to be an effective substance to promote the assembly of pure tubulin [Schiff et al. 1979] and to reduce the critical concentration of microtubule formation. Taxol also interferes with microtubule dynamic instability by preventing the filaments from shrinking and thus stabilizing them in their polymerized lengths. The feature characteristics of microtubule assembly and disassembly are used for protein purification and sample preparation (see chapter 2.1).

1.2 Force generation and motility

Maintenance of cell shape, cell division, and cell motility, all involve the cytoskeleton. They depend on dynamic assembly and disassembly processes of the cytoskeletal polymers, the regulation and modification of their structure by polymer-associated proteins and motor protein movement along the polymers. Whereas the most important function of the intermediate filaments is to reinforce cells and to organize cells into tissues, actin filaments, microtubules and their associated proteins are know to be mainly involved in cell motility.

Motility is defined as the ability to move spontaneously and independently. The basis for all cell movement arises from the cytoskeleton, which undergoes constant rearrangement and thus can produce movement. Within cells, there are two basic mechanisms for generating forces. One is due to the structural changes of the microfilaments and microtubules. The cell shape changes by assembly/disassembly processes of these two filaments and affiliation of filamentous structures. The other motion is caused by motor proteins. Cell movements are affected by both actions the movement of molecular motors, and the rearrangement of the cytoskeleton, e.g. during the assembly of sarcomeres, that contractile units of a muscle cell [Pizon et al. 2002].

Polymerization-driven motility. Motilities of intracellular viruses and bacteria are examples for movement due to actin polymerization. For instance, *Listeria monocytogenes* are actin-moved bacteria. The bacterium propels itself through the cytoplasm of the host cell by the assembly of bundles of actin filaments behind it. Even after the bacterium collides with the plasma membrane of an infected cell, it keeps on moving and thus, creates thin, spiky extensions on the cell surface. When such microspikes with a bacterium on its tip are engulfed by a neighboring cell the bacteria can spread out [Tilney and Portnoy 1989]. Longer versions of microspikes, called filopodia, are found, e.g. on the growing edge of a nerve cell axon. Such structures make a cell more sensitive towards external stimuli.

Migration of animal cells, like fibroblasts, macrophages, and motile white blood cells (*neutrophils*), is also driven by actin-polymerization. All of these cells have in common a leading edge enriched in assembling actin filaments. The movement can be triggered by certain chemicals in the cell environment (chemotaxis).

A process which involves microtubule polymerization is the anaphase, a later phase of mitosis. In the early anaphase (anaphase A) separated chromatids are moved towards the spindle poles with the help of microtubules which shorten the spindle. After complete chromatide separation in the anaphase B the elongation of astral microtubules drives spindle poles further apart.

Many activities concerning cell movements are related to the interaction of both microfilaments and microtubules, e.g. the polarization of cytotoxic T-cells during immune response to invading organisms and the toxic molecules produced by them.

Motor protein-driven motility. Molecular motors are striking biological "nano-machines" responsible for the movement inside cells. They are characterized by their motion along a filament powered by adenosine 5′-triphosphate (ATP) hydrolyses and Mg^{2+}/Ca^{2+}-ions catalyzing the ATPase. ATP is the chemical energy source that is converted by the motor proteins into mechanical work or motion [Howard 2001, Schliwa 2003], where the direction is dependent on the track polarity.

Motor proteins have been divided into three superfamilies: myosin, which moves along actin filaments, and the microtubule-based motors, dynein and kinesin, which are differentiated by their amino acid sequence in the active domain. In recent years, many motors have been identified and sorted into different families of each superfamily depending on their modular design (e.g. N-/C-terminal or monomeric/dimeric motors) and function (e.g. fast and slow motors). For instance, at least 18 protein families of myosin and two families of dynein are known [Schliwa and Woehlke 2003]. The superfamily of kinesin comprises more than 200 molecules that have been classified into 14 different groups [Lawrence et al. 2004]. Among the three superfamilies of linear motors several proteins are classified according to their cellular function (see Table 1.2-1):

- they generate force either towards the fast ("plus-end" motor) to the slow growing end ("minus-end" motor) of the particular filament;
- they perform single steps (non-processive) or processive transport, where processivity is defined as the ability of an enzyme to repetitively continue its catalytic function without dissociating from its substrate;
- they work as individuals or cooperate in groups.

Molecular motors either slide or walk along filaments.

Filament sliding. The motor protein discovered first was the skeletal muscle myosin, myosin II. Studies began in the 19th century. It is the most famous member of the non-processive motors. Sliding is achieved because many motors are "marching" on the filament and contractile forces can be generated.

The protein of the dynein superfamily that was discovered first is the axonemal dynein in cilia (early 1960s). Microtubule doublets are the structural components of an axoneme, the inner core of cilia. Cilia are finger-like protrusions of cell membranes connected to the basal body. Axonemes bend when the microtubule doublets stay partly cross-linked and partly slide against each other. The sliding is caused by the dynein motor and ATP. Such *motile cilia* constantly beat in one direction and thus move substances over or around the surface of the cell or move the cell itself through the liquid.

Cytoskeletal motors. The common feature of cytoskeletal motors is the unidirectional transport of cargos such as vesicles, organelles or possibly even chromosomes along the polar structure of the cytoskeletal filaments.

Actin-based vesicle trafficking is known for, for instance, the monomeric myosin I, which is involved in crawling processes of the slime mold, a protist that takes the form of an amoebae. Dimeric myosins, such as myosin V and VI are motor proteins with two identical motor heads that carry cargoes along actin filaments. Compared to the muscle myosin, these cytoplasmatic motors have a much higher duty free ratio. The latter means that the motors are bound to the filament during almost the whole ATP cycle and thus, they can individually transport their membrane cargoes processively.

The cytoplasmatic dynein is an ATPase with two active domains that walks continuously to the "minus-end" of microtubules [King and Schroer 2000]. The protein is important for the retrograde transport towards the cell body in axons. Its counter partner is kinesin-1, which is a "plus-end" motor. Kinesin-1, is the most prominent processive working motor and the protein of the kinesin superfamily identified first (mid 1980s). Nowadays, it is the best understood molecular machine (see following chapter). A monomeric motor protein can also realize persistent movement. An example is the one-headed motor KIF1A of the kinesin family. A mobile tether of a positively charged loop of the motor domain interacts with the negatively charged C-terminus of the tubulin. In this way it allows 1D diffusion along the microtubule to the next binding site [Okada and Hirokawa 1999a/b].

Motor family		F	Dr	Pr	Biological activity
Myosins		actin			
Myosin I (•)	monomer		plus	yes	Amoeboid motility, epithelial development
Myosin II (*)	dimer		plus	no	
- muscle					Muscle contraction
- cytoplasmatic					Cytokinesis, phagocytosis, cell shape/polarity
Myosin V (i)	dimer		plus	yes	Transport of melanosomes, mRNA, neuronal vesicles
Myosin VI	dimer		minus	yes	Vesicle transport, hair cell function, epithelia function
Dyneins		MT			
axonemal (*)	heteromer		minus	no	Cilia and sperm motility
cytoplasmatic (i)	dimer		minus	yes	Retrograde axonal transport, mitosis, transport in flagella

Kinesins		MT			
Kinesin-1 (^{i})	dimer		plus	yes	Anterograde axonal transport
Ncd ($^{\bullet}$)	monomer		minus	no	Meiosis and mitosis
KIF 1A (^{i})	monomer		plus	yes	Transport of synaptic vesicle precursors and mitochondria

Table 1.2-1: Properties of linear molecular motors. (F) filament; (Dr) direction of movement; (Pr) processivity, (*) works in large groups (10^6 - 10^9 motors), ($^{\bullet}$) works in small groups (10-1000), (^{i}) individualist or a group less than 10 motors acting together. [Howard 2001, Kreis and Vale 1999, Schliwa 2003]

1.3 The motor protein kinesin-1

1.3.1 Structure of the motor protein kinesin-1

In 1985 a novel brain ATPase, which is involved in neuronal microtubule-based motility, was identified in a biochemical fractionation of squid and mammalian nervous tissue. Based on the Greek word for "to move", the protein was named kinesin [Brady 1985, Vale et al. 1985]. In resent years, the kinesin superfamily has become very large. On the bases of the new kinesin nomenclature the protein we used throughout this work is now termed kinesin-1 [Lawrence et al. 2004] and includes sequences of proteins known as conventional kinesin, KHC (kinesin heavy chain) and kinesin-I. We follow the new notation (or referred to it simply as kinesin).

Kinesin-1 is a dimeric motor protein possessing two kinesin heavy chains (KHC, 110 - 113 kDa). Mammalian brain KHCs are isolated together with two kinesin light chains (KLC, 60 - 70 kDa), see Figure 1.3-1. The total length of the molecule is approximately 80 nm [Bloom et al. 1988, Scholey et al. 1989].

The functional motor domains include the two N-terminal globular heads. Each head contains the catalytic core (ATP-binding site) and a microtubule-binding site. The neck- (about 50 amino acids) and the hinge regions are found to be involved in the determination of directionality of the movement along the microtubules, in the processivity and the mechanochemical coupling [Case et al. 1997, Romberg et al. 1998, Grummt et al. 1998], see following sections. The two stalks dimerize and form an α-helical coiled coil. The hinge and kink regions give flexibility to the otherwise stiff stalk [Hirokawa et al. 1989, Yang et al. 1989]. Part of the following tail domain is also known as cargo domain because it binds the transported material and interacts with the KLCs [Vale et al. 1997]. KLCs are believed to have regulatory functions and are involved in cargo binding in vivo [Verey et al. 1998].

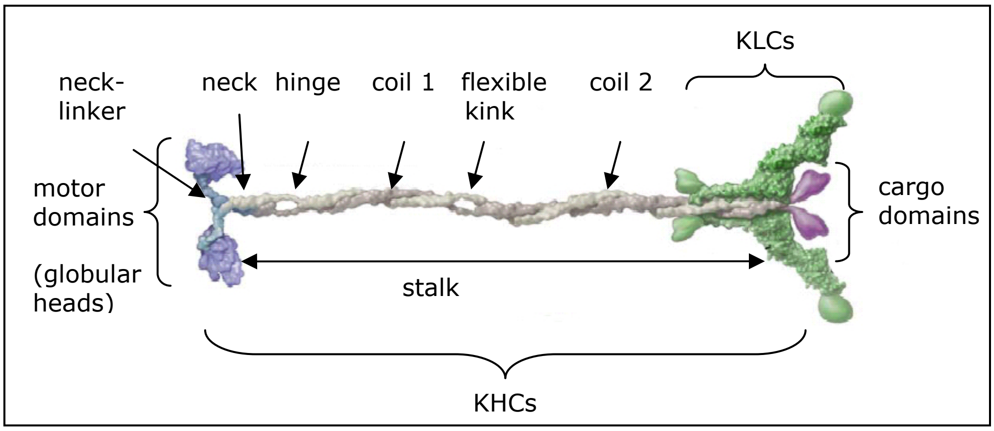

Figure 1.3-1: Structure of kinesin-1, former notated as conventional kinesin, KHC or kinesin-I. The tetrameric mammalian kinesin is comprised by the two kinesin heavy chains (KHCs) and the two kinesin light chains (KLCs). [adapted from Vale 2003]

1.3.2 Mechanochemistry of a single kinesin molecule.

The walking direction of the kinesin-1 molecules is stringent and highly processive to the fast growing end of the microtubule. The motor is involved in transport processes like moving of cell organelles (e.g. mitochondria) and vesicles (e.g. precursors of synaptic vesicles formed in the Golgi) from the cell body toward the effector cells, or towards other neuronal cells realizing fast axonal transport [Schnapp et al. 1985, Vale et al. 1985, Goldstein and Yang 2000].

The motor protein binds with its motor domains preferentially to the β-tubulin of the microtubule. Thus, the step distance is defined by the length of a tubulin dimer, which is about 8 nm. At low loads (almost zero) one molecule of ATP is hydrolyzed for every 16-nm turn (one 8-nm step) [Svoboda et al. 1993, Hua et al. 1997, Schnitzer and Block 1997, Coy et al. 1999]. Before the molecule dissociates from its track it performs about one hundred steps [Howard et al. 1989, Block et al. 1990], which implies an approximate run length of 1 µm. Overall, the processive movement depends on both the structure of the microtubule and the intrinsic properties of the motor protein itself as well as on chemical and physical reaction conditions.

Motor movement is strongly dependent on conformational changes in the motor domains and the flexible neck regions (neck-linker) which follow the motor domains. Crystallographic analysis of the head domains reveal that these regions appear in two different structures [Kull et al. 1996]. Furthermore, cryo-electron microscopy (cryo-EM) studies of kinesins [Kozielski et al. 1997] combined with spectroscopy studies such as electron paramagnetic resonance (EPR) and fluorescence resonance energy transfer (FRET) of truncated kinesin monomers [Rice et al. 1999] have shown different nucleotide-dependent structural conformations in the neck-linker. These findings led to the molecular movement model called "hand-over-hand"-model, which is similar to human walk and includes major nucleotide-dependent steps, see Figure 1.3-2 [Vale and Milligan 2000, supported by Tomishige et al. 2006].

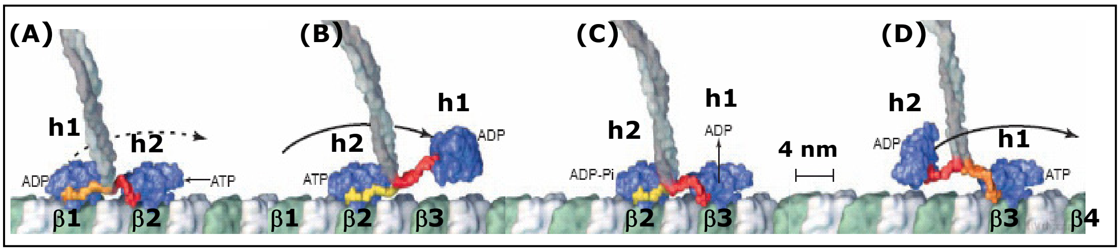

Figure 1.3-2: "Hand-over-hand" model of kinesin stepping. In the presence of ATP kinesin-1 moves towards the "plus-end" of the microtubule binding only to the β-tubulin (green) of the protofilament-subunit of a microtubule. (A) Both heads are bound to two adjacent β-tubulins of one protofilament of a microtubule. The neck-linker of the tailing head (h1, orange) is close to the catalytic core (blue) but only loosely attached (ADP-state). At the leading head, ATP-binding causes a tight docking and zipping of the neck-linker (red—›yellow) to the core. (B) Next, the nucleotide binding provokes the tailing head (h1) to be thrown forward towards the next free binding place (towards the β3-tubulin), and becomes the leading head. (C) After a diffusion-process (16 nm) this head (h1) binds to the filament causing the 8-nm shift (center-of-mass) of the load and ADP unbinding is accelerated. In the now tailing head (h2) the ATP is hydrolyzed to ADP + Pi. (D) The release of the phosphate (Pi) opens a 0.5-nm space in the motor domain, the neck-linker (red) detaches and the process of head forward-movement (toward β4-tubulin) starts, while the now leading head (h1) binds ATP and thus the neck-linker docks to the catalytic core again. [adapted from Vale and Milligan 2000]

Further studies are regarded as support for the "hand-over-hand" model. One group measured single stepping of different dimeric kinesin constructs with an optical force-clamp apparatus. Results showed "limping" motors with stepwise motion that alternates between two different sizes [Asbury et al. 2003]. Yildiz et al.

(2004) observed single molecule movement using fluorescence imaging with one-nanometer accuracy (FIONA). An organic dye was bound to one of the motor domains of a motor molecule. The movement, recorded over minutes, showed alternating 0-nm and 16.6-nm shifts.

The chemo-mechanical transduction causes motor binding and strains the elastic neck-linker within the motor. This stress and the entropy resulting from the kinesin/microtubule interaction are thought to be the driving force for motion [Taniguchi et al. 2005]. The kinesin movement is coupled to the chemical cycle. Thus the transport velocity depends on the rate at which each head hydrolysis the ATP-molecule. At experimental conditions of low load, excess of ATP and room temperature, *in vitro* transport velocities are observed to vary between 0.5 and 1 µm/s [Howard et al. 1989, Coy et al. 1999]

The force exerted by a single kinesin molecule has been measured by several groups in different ways. Hunt et al. (1994) recorded microtubule gliding while increasing the viscosity of the surrounding medium up to 200-fold. Linear decrease of the gliding velocity was observed with increasing buffer-viscosity. The calculated drag force resulted in maximum forces between 4 - 5 pN from extrapolation to zero speed. Similar force values (4 - 8 pN) were obtained using optical tweezers that impose an elastic load onto bead-transporting motors [Svoboda and Block 1994, Kojima et al. 1997, Visscher et al. 1999, Kawaguchi and Ishiwata 2000]. Other groups have used a force-fiber apparatus as an external load on the motion of a single kinesin molecule obtaining an average stall force of 5.4 pN [Meyhofer and Howard 1995]. By measuring the bending of microtubules [Gittes et al. 1996] determined forces were in the range of 4-6 pN consistent with measured kinesin stalling forces.

1.4 Experimental approaches to study the dynamics in a many - motors system

Since the discovery of the motor protein kinesin-1, a lot of experiments have been carried out to understand its mechano-chemical behavior. The mechano-chemical properties and transport parameters are well known by now (see previous section). In cells, cooperative transport of several motors is important and rather common.

The cytoplasmatic architecture is highly complex. Whereas small molecules easily diffuse within the highly viscous cytoplasm, macromolecule transport is affected by the filamentous network that extends throughout. Thus, larger particles experience an effective viscosity [Luby-Phelbs 2000]. In such cases, fast transport is realized by several motors that are cooperatively transporting the cargo and thus generate higher forces than a single molecule. Electron microscopy images show that cargos, like mitochondria, vesicles and membranous organelles, are linked to the microtubules by more than one molecule [Miller and Lasek 1985, Ashkin et al. 1990, Hirokawa 1996]. Observations of cargo transport in vivo [Gross et al. 2002, Hill et al. 2004, Kural et al. 2005, Levi et al. 2006] and in vitro [Coy et al. 1999, Hunt et al. 1994, Seitz and Schliwa 2006] resulted in different velocity-, run length- and force distributions for different kinesin concentrations.

Furthermore, a theoretical model on motor cooperativity suggests a strong increase in the run lengths of cargoes with increasing number of motors actively pulling [Lipowsky et al. 2001, Klumpp and Lipowsky 2005].

1.5 Overview

This thesis is organized as follows. The performed experiments and techniques used are explained in chapter 2. The results obtained are discussed in chapter 3. Transport parameters and their dependence on the kinesin concentration and various sizes are studied *in vitro*. While the bead concentration is kept constant different motor numbers on the bead surface are realized by changing the motor concentration in solution. We have explored how several motors that are pulling a load together change the transport parameters run length, velocity and force exertion. Additional experiments are performed to characterize the active motor number. The results, together with included geometrical constraints inherent to the transport system, have allowed us to estimate a range for the number of motors pulling on the load. We finish with a conclusion and outlook, pointing out possible experiments and raising a few open questions in chapter 4.

Chapter 2

Experimental Methods and Materials

First, the purification procedures of microtubules (chapter 2.1.1) and kinesin-1 (chapter 2.1.2) out of porcine brain and the analyses of the proteins (chapter 2.1.3) are explained. Optical microscopy methods are the basic tools to determine kinesin properties like run length and force exertion. Microtubules (25 nm in diameter) are objects that are about one order of magnitude smaller than the diffraction-limited resolution of light (in the order of 250 nm). To observe these filaments in real time, video-enhanced microscopy combined with phase contrast and differential interference contrast microscopy is used (chapter 2.2.1). The experimental setup is explained in chapter 2.2.3. Force measurements were performed with a single optical trap (chapter 2.2.2). The third section of the chapter deals with the kinesin-to-bead binding. Using carboxylated polystyrene beads, an unspecific covalent binding of kinesin was expected. Keeping the bead concentrations constant and changing the kinesin concentrations in the bead assay the amount of molecules attached to a bead varies. Methods like Isothermal titration calorimetry (ITC; chapter 2.3.1) and Dynamic light scattering (DLS; chapter 2.3.2) were applied in an attempt to determine the kinesin molecule-to-bead ratio.

2.1 Protein purification and analysis

The highest concentration of tubulin is found in the mammalian brain. Therefore mammalian brain is a preferred tissue for the isolation of tubulin. The tubulin, the main component of microtubules, combined with microtubule-associated proteins (MAPs), such as kinesin, was purified from fresh porcine brain provided by a local slaughterhouse.

The isolation steps were performed in a cold room at 4° C if not otherwise stated. The system of the fast protein liquid chromatography, FPLC, was performed in a cold cell at 4 - 8° C.

To determine the size, purity and concentrations of the proteins gel electrophoresis and Lowry assay were carried out. Performing the microtubule-turbidity assay the activity of tubulin was tested. The activity of kinesin can be observed using the gliding assay.

2.1.1 Tubulin purification

Microtubules were obtained by two cycles of temperature-dependent disassembly/reassembly *in vitro* according to the method of Shelanski et al. (1973). The reassembly steps were performed in the presence of 4 M glycerol to reduce the amount of MAPs, that are co-purifying with tubulin and to slow down the inactivation of tubulin over time [Vater et al. 1986]. MAP-free tubulin is needed to perform motility assays. MAPs are separated from the tubulin by ion exchange chromatography on phosphocellulose [Weingarten et al. 1975]. Whereas MAPs are absorbed to the phosphocellulose tubulin does not bind because of its acidic domains. They can be eluted using 0.8 M NaCl. Final microtubule concentrations were found to be between 8 - 12 mg/ml. The detailed protocol to obtain MAP-free tubulin is described in Table 2.1-1.

Buffer systems (pH 6.8):
BufferA: 50 mM imidazole, 0.5 mM EGTA, 0.1 mM EDTA, 0.5 mM $MgCl_2$, 0.5 mM DTT
BufferB: 50 mM imidazole, 50 mM KCl, 1 mM EGTA, 0.5 mM $MgCl_2$, 0.5 mM DTT
BufferB + 10 M glycerol (assembly buffer)

1. **Removal of cell compartments**

- Porcine brain was homogenized in bufferA combined by protease blocker 0.5 mM Pefabloc (Pe) at a ratio of 3:2 wt/vol and followed by two centrifugations.
- First centrifugation at 27500 g and 2° C for 30 min.
- After adding 0.5 mM Pe to the supernatant the 2. centrifugation was carried out at 125000 g and 2° C for 45 min.

2. **First assembly**

- At a ratio of 1:4 vol/vol assembly buffer combined by the cofactor GTP (0.56 mM) was added to the supernatant (final concentration: 2 M glycerol).
- Assembly of microtubules at 37° C for about 30 min.
- Centrifugation: 125000 g at 30° C for 60 min (removal of not active dimers)

3. **First disassembly**

- Discard the supernatant and dissolve the pellet of MTs in 40 ml of bufferB (cold room).
- Disassembly takes place at 4° C for about 30 min.
- Centrifugation: 145000 g, 45 min, 2° C.

4. **Second assembly**

- 4:1 vol/vol supernatant to assembly buffer and 0.56 mM GTP (final conc.: 2 M glycerol).
- Assembly at 37° C for about 30 min.
- Centrifugation: 110000 g, 60 min, 30° C.

5. **Second disassembly**

- Discard the supernatant and dissolve the pellet in 12 ml of bufferB.
- Disassembly at 4° C for about 30 min.
- Centrifugation: 125000 g, 45 min, 4° C.

6. **Ion exchange chromatography on phosphocellulose at 4° C**

- About 10 ml supernatant (~ 30 mg/ml) was applied to 180 ml of an activated phosphocellulose P11 (Fa. Whatmann) using a peristaltic pump (flow: 0.5 ml/min).
- Chromatography was carried out at a flow rate of 2 ml/min with elution bufferB. The fraction volume was 2 ml.

7. **Storage**

- After adding 1 M glycerol and 0.5 mM GTP to the tubulin suspension the protein (about 10 mg/ml) was stored in liquid nitrogen (- 80° C).

Table 2.1-1: Purification of PC-tubulin for gliding assay and microtubule alignment. Porcine brain microtubules are obtained by two cycles of the temperature-dependent disassembly/reassembly. Microtubules associated proteins (MAPs) were removed via ion exchange chromatography on phosphocellulose.

The activation of the phosphocellulose (P11, Whatman Int. Ltd. Maidstone, UK) is based on the company instruction and had to be performed one day in advance. It consists of soaking the resin in 0.5 M NaOH for 5 min, decanting off the supernatant and washing the material with double distilled water (ddH$_2$O) using a glass frit. The preparation was followed by decreasing the pH to less than pH 11 using 0.5 M H$_3$PO$_4$ before soaking the resin was soaked in 0.5 M HCl for 5 min. The supernatant was removed; the resin washed with ddH$_2$O and the pH increased to above pH 3 by rinsing the resin with 0.5 M H$_3$PO$_4$ and ddH$_2$O. Finally, the activated phosphocellulose resin was equilibrated in bufferB and transferred to a glass column.

2.1.2 Kinesin purification

The motor protein kinesin was purified from porcine brain homogenates by the consecutive steps of ion exchange chromatography, microtubule affinity binding, and gel filtration [Kuznetsov et al. 1986]. The procedure lasted two days and was performed as described in Table 2.1-2.

The cation exchange resin diethylaminoethyl cellulose (DEAE-cellulose; DE 52 Whatmam Int. Ldt. Maidstone, UK) had to be equilibrated in 50 mM imidazole buffer to the physiological pH of 6.8. The gel filtration sephacryl resin S-300 high resolution (Amersham Bioscience Uppsala, Sweden) had to be equilibrated in the respective buffer systems. Both resins had to be pretreated one day in advance referring to company instructions. The phosphocellulose was activated as mentioned in chapter 2.1.1. DEAE-cellulose and phosphocellulose were stored in a cold room at 4°. Before utilization, the supernatants were removed and the resins were resuspended in the respective buffer systems. A 26 x 950 mm^2 sized glass column was packed with the Sephacryl S-300 resin and washed with elution bufferA (kinesin purification buffer, see Table 2.1-2 below) of a volume of 520 ml, the volume was equivalent to the resin volume.

Buffer systems (pH 6.8 unless otherwise noted):
BufferA: 50 mM imidazole, 0.5 mM EGTA, 0.1 mM EDTA, 0.5 mM $MgCl_2$, 0.5 mM DTT (kinesin purification buffer)
BufferA + 150, 250 or 700 mM KCl
BufferB: 50 mM imidazole, 50 mM KCl, 1 mM EGTA, 0.5 mM $MgCl_2$, 0.5 mM DTT, 10 M glycerol
BufferB + 10 M glycerol

First day

1. **Removal of cell compartments**

- Porcine brain was homogenized in bufferA (pH 7.2) with protease blocker 0.5 mM Pe at a ratio of 1:1 wt/vol and followed by two centrifugations.
- First centrifugation at 13500 g and 2° C for 40 min.
- After adding 0.5 mM Pe to the supernatant the second centrifugation was carried out at 27500 g and 2° C for 45 min.

2. **First ion exchange chromatography (cation exchange)**

- Supernatant was mixed with 780 ml (340 g DEAE welled in bufferA) equilibrated DEAE cellulose (Whatman).
- Unbound components are washed out with 2.5 l bufferA.
- Elution of kinesin with bufferA + 150 mM KCl + 0.5 mM Pe.

3. **Second ion exchange chromatography**

- Eluate was mixed with activated phosphocellulose (PC) and stirred gently for 45 min followed by batch chromatography (removal unbound materials). The PC was poured into a glass column (200 x 50 mm^2); the protein was eluted with 0.5 mM KCl/bufferA + 0.5 mM Pe.

4. **Kinesin-Elution using FPLC**
- Chromatography was carried out at a flow rate of 2 ml/min with elution bufferA + 0.7 mM KCl + 1mM Pe. The fraction amount was 7 ml. The protein eluted after about 1 hour.
- The protein fractions (120-130 ml) were dialyzed against bufferA + 150 mM KCl (ratio 1:10) for approximately 2 x 45 min. After the eluate reached 150 mM another centrifugation was performed at 45 min, 185000 g, 2° C.

5. **Microtubule-affinity binding**
- The supernatant was stabilized with 1.55 M glycerol in bufferB before approximately 1/3 of the microtubule suspension (see Box 3.1-3) were added combined with 5.42 μM taxol and 2.5 mM TPP in bufferB.
- After 10 min of incubation at 37° C the mixture was sedimented for 70 min, 145000 g, 20° C through a layer of 4 M glycerol in bufferB supplemented with 1.2 mM TPP und 5 μM Taxol in bufferB followed by a protein foam (ratio 1:3 of affinity mixture and protein suspension). Leave the layer mix for 10 min.
- Sediment was resuspended with 5 mM ATP and 20 μM taxol in bufferA + 250 mM KCl and centrifuged at 185000 g, 20° C for 30 min to separate kinesin (supernatant) from microtubules.

6. **Gel filtration** (over night)
- The supernatant (ca. 5-5.3 ml) was applied to a column packed with 530 ml Sephacryl S-300 (Pharmacia) using a peristaltic pump (flow: 0.5 ml/min).
- Chromatography was carried out at a flow rate of 0.42 ml/min with elution bufferA at 4° C.

Second day
- 3 ml fractions were collected, protein fractions detected measuring the UV-absorption of proteins at 280 nm and furthermore analyzed by SDS-Page.

7. **Concentration of kinesin**
- Pool of kinesin fractions (5 fractions) were concentrated by ultracentrifugation (about 15 min, 5000 g, 4° C) using 100K filters (Millipore Amicon Ultra-15) to a final kinesin concentration of 1 mg/ml.

8. **Storage of protein**
- After adding 1 M glycerol and 0.5 mM GTP to the kinesin suspension, 30 μl aliquots of the protein were stored in liquid nitrogen (-80° C).

Table 2.1-2: Purification of porcine brain kinesin. The two days lasting procedure is characterized by consecutive steps of ion exchange chromatography, microtubule affinity binding, and gel filtration.

The isolation of microtubules for kinesin purification is similar to the procedure explained above. They are obtained by only one cycle of temperature-dependent disassembly/reassembly. The isolation process is shown in Table 2.1-3.

Buffer systems (see Table 2.1-1)

1. **Removal of cell compartments**
- Porcine brain was homogenized in bufferA combined by protease blocker 0.5 mM Pe at a ratio of 1:1 wt/vol and followed by two centrifugations.
- First centrifugation at 13500 g and 4° C for 30 min.
- After adding 0.5 mM Pe to the supernatant the second centrifugation was carried out at 125000 x g and 4° C for 45 min.

2. **Assembly**
- At a ratio of 1:4 vol/vol assembly buffer combined by the cofactor GTP (0.56 mM) was added to the supernatant (final concentration: 2 M glycerol).
- Assembly of microtubules at 37° C for about 45 min.
- Centrifugation (125000 g at 30° C for 60 min) to get the microtubules into the pellet and to remove inactive dimers.

3. **Disassembly**
- Discard the supernatant and 2° C dissolve the pellet in 40 ml of bufferB.
- Disassembly takes place at 4° C for about 60 min.
- Centrifugation: 145000 g, 45 min, 2° C.

4. **Ion exchange chromatography on phosphocellulose**
- Supernatant (about 20 - 30 ml) was applied to 20 g of an activated phosphocellulose P11 (FA. Whatmann) using a tube pump (flow: 0.5 ml/min).
- Chromatography was carried out at a flow rate of 1 ml/min with elution bufferB. The fraction amount was 5 ml. 20 µM taxol; 0.5 M glycerol and 0.5 mM GTP were added to the pooled protein fractions.

5. **Preparation for kinesin purification (step 5)**
- Required microtubule concentration was assembled at 37° C for 35 min.

Table 2.1-3: Purification of PC-tubulin for kinesin isolation. This isolation process is characterized by just one cycle of microtubule disassembly/reassembly. MAPs are removed via chromatography on phosphocellulose.

2.1.3 Quantity and quality analysis

2.1.3.1 Electrophoresis-Coomassie staining

The purity of proteins was tested using SDS-polyacrylamide gels (SDS-PAGE) [Laemmli 1970]. This is a method used to separate proteins under denaturated conditions on a support matrix within an electric field. The support matrix used here was polyacrylamide gel, which promotes a separation by size and charge allowing smaller particles to migrate faster while retarting or just obstructing bigger molecules. Sodium dodecyl sulphate (SDS) is an anionic detergent that confers a negative charge to the polypeptide in proportion to the length of the polypeptide. Therefore, the migration is determined by the molecular weight of the polypeptides. The continuous 7.5 % SDS-PAGE were used with Mini-PROTEAN® 3 Cell (BioRad) and run at 20 mA (one gel) for 45 min. Samples of the proteins and the sample of the high molecular weight standard (Sigma) were mixed 5:1 with loading buffer (5 times concentrated) under reducing condition, incubated for 5 min at 96° C and immediately pipetted into the chambers of a gel card. The gels were stained in bromphenole blue staining solution for 25 min, rinsed with ddH$_2$O and destained in a 10 % acetic acid solution. The colored bands were fixated on the gel for 20 min in a 10 % glycerol solution, dried and stored between two cellophane papers. The solutions used are shown in Table 2.1-4.

PAA solution:	30 % acrylamide, 0.8 % bisacrylamide
Running buffer:	1 x SDS (1:10 Roth rotiphorese SDS–Page 10 x/ddH2O)
5 x loading buffer: (pH 6.8)	0.313 M Tris, 10 % SDS, 50 % glycerol, 0.05 % bromphenole blue brilliant blue R 250, Roth), 0.1 M DTT or 5 % β-mecaptoethanol
Staining solution:	0.2 % bromphenole blue (brilliant blue R250, Roth), 40 % ethanol, 10 % acetic acid
Destaining solution:	10 % ethanol, 10 % acetic acid
Fixation buffer:	10 % glycerol, 20 % ethanol

Table 2.1-4: Solutions for gel preparation, running and staining.

Figure 2.1-1 shows a Coomassie blue-stained polyacrylamide gel of kinesin (B) and PC-tubulin (C). The purified kinesin sample consists mainly of kinesin heavy chains (KHCs) and kinesin light chains (KLCs).

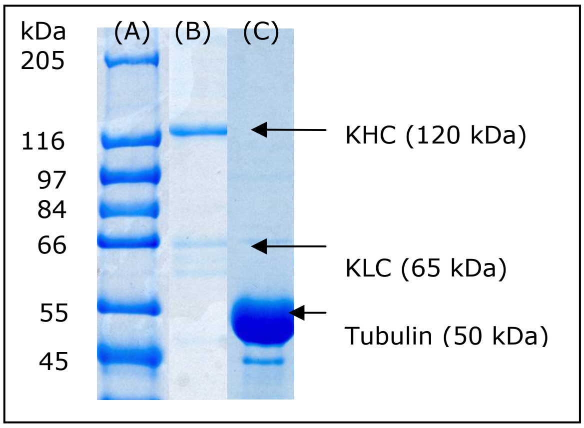

Figure 2.1-1: Coomassie blue-stained polyacrylamide gel of porcine brain kinesin and PC-tubulin. (A) 10 µl color marker (Sigma, wide range) including proteins in the size range of 45 to 205 kDa; (B) 16 µg purified kinesin with the two bands: for kinesin light chain (KLC) and kinesin heavy chain (KHC) and (C) 60 µg isolated PC- tubulin.

2.1.3.2 Western blot

Western blot is a sensitive enzyme immunoassay to detect specific antigens. The system used is based on the combination of streptavidin and biotin, a powerful and sensitive complex in biochemistry to link molecules (e.g. proteins). In this assay monoclonal antibodies are linked to the enzyme phosphatase.

The proteins and antigens are transferred and bound to a nitrocellulose membrane. This is done electrophoretically. The proteins are passively transferred from a 7.5 % SDS-PAGE (see previous chapter, before staining) onto the membrane. After plotting the gel can be stained after the plotting as a control. The remaining unbound sites are removed from the membrane with non-fat dry milk. The bound antigens are incubated with their specific antibody (primary antibody, PA). After removing the unbound antibodies the blot is incubated with biotinylated antibodies (secondary antibody, SA) specific for the first antibodies. After washing the membrane it is incubated with a streptavidin-biotinylated alkaline phosphatase complex, which binds to the biotin of the second antibodies. The target antigens are visualized with the help of a BCIP/NBT (5-bromo-4-chloro-3-indolyl phosphate/nitro blue tetrazolium) substrate provided by Bio-Rad Inc., Richmond. It colors the activated protein bands purple while the background remains white.

The purified porcine brain kinesin stock solution was tested for the motor protein antagonist dynein, for tau, MAPs and tubulin. The electrophoretical blotting was done in Mini-Trans Blot® (Bio-Rad Inc., Richmond). The protocol is based on the manufacturer instructions and listed in Table 2.1-5.

The sample of purified kinesin was shown to be free of the proteins tubulin and dynein. Furthermore, it was shown that the tau-protein and MAPs are co-purified using the purifying procedure described above. Compared to the kinesin the percentage of these two proteins is relatively small. Only weak bands are observed in the polyacrylamide gel, see lane (B) in Figure 2.1-1.

Buffer systems:

Buffer for electrophoreses (see chapter 2.1.3.1)
BufferC: 50 mM TRIS, 40 mM glycine, 1.3 mM SDS dissolved in 20 % methanol (pH 7.5)
Blocking buffer: 1 x PBS, 0.05 % TWEEN 20, 5 mg/ml BSA
BufferD: 20 mM TRIS, 500 mM NaCl, 0.05 % TWEEN 20, pH 7.5
Color solution: one color tablet (4-chloro-1-napthol, Sigma C-6788) dissolved in 10 ml methanol; 0.6 ml of this solution are dissolved in 10 ml bufferD and 10 ml H_2O_2

Primary antibodies (PA, from Sigma): monoclonal anti-kinesin (K1005)
monoclonal anti-τ (T5530)
monoclonal anti-dynein (D1667)
anti-tubulin (T3526)
anti-MAPs (M7273)

Secondary antibodies (SA, from Sigma): anti-mouse IgG (M5899),
anti-rabbit IgG (R1131)

Plotting scheme for one protein:

1.	2.	3.
PA	-	PA
SA	SA	-
SP	SP	SP
CS	CS	CS

1. 7.5 % SDS-PAGE
- Gel was prepared and run as described in the previous chapter. Per slot 16 µg of the kinesin (stock solution) was load onto the gel (15 slots).
2. Electrophoretic transfer to a membrane
- The gel and two nitrocellulose membranes were socked in bufferC.
- The gel is placed on the first membrane and covered with the second membrane. Avoid bubbles!
- The stacked layers are fixed into the electrophoretic transfer system and filled with bufferC.
- The transfer is performed at 9 V for 1 hour and afterwards the membrane is put in the 0.5 % blocking buffer for another hour.
3. Incubation of the primary antibody (PA)
- The membrane is cut in 15 stripes (three for each protein analyzed). They are placed in different boxes. As seen in the plotting scheme 10 stripes are socked in antibody-blocking buffer solution (2 % of the stock solution PA) while shaking over night in the cold room, the other 5 stripes just in the blocking buffer as a control.
4. Incubation of the secondary antibody (SA)
- Removal of the previous solution and washing of the stripes 2 times with the blocking buffer (shaking).
- SA stock solution was diluted 1:2000 in the blocking buffer and added to the stripes (see scheme), 3 h of gentle agitation in the cold room.
5. Incubation of the streptavidin-biotinylated alkaline phosphatase complex (SP)
- Removal of the previous solution and washing of the stripes 2 times with the blocking buffer (shaking).
- SP stock solution was diluted 1:200 in the blocking buffer and added to all stripes for 30 min at room temperature (shaking).
6. Color development
- Removal of the previous solution and washing of the stripes 6 times with bufferD, for 10 min at RT.
- All stripes are socked for 30 min in color solution.
7. Washing and Drying
- Decant the previous solution and wash the stripes with ddH2 for 10 min at RT (gentile agitation).
- Cover the membrane strips and leave them to dry.

Table 2.1-5: Protocol of Western blot. Immunoassay used to analyze the kinesin bulk solution. It was tested for kinesin heavy chain (KHC), dynein, tau protein, MAPS, and tubulin.

2.1.3.3 Lowry Method

The Lowry method [Lowry et al. 1951] is a common method for measuring the amount of protein in a sample. It is based on the formation of a colored copper protein complex, which is subsequently determined by absorption spectroscopy. First, a copper ion complex is formed in alkaline solutions ("Biuret"-chromophore). Second, the reduction of the Folin-Ciocalteu reagent (phosphomolybdate and phosphotungstate) occurs due to tyrosine, tryptophan, cysteine and histidin residues. The reduced solution is blue and therefore detectable with a spectrophotometer (Varian carry 1) at 760 nm. Bovine serum albumin was used as the standard solution in the range of 0 to 0.1 mg/ml.

The kinesin concentration of 1.0 ± 0.05 mg/ml was obtained from two preparations. The PC-Tubulin concentration out of three preparations was 12.0 ± 0.5 mg/ml.

2.1.3.4 Microtubule-turbidity assay

The microtubule-turbidity assay is a time dependent assay. It uses the properties of assembled microtubules that scatter light more than free tubulin dimers because of their differences in size, geometry, and concentration. An increase in the scattering signal means higher microtubule concentration within the solution. With this method the critical concentration of the purified tubulin was determined.

The measurement was carried out using a UV-spectrometer (Varian carry 1) at 360 nm with a temperature controlled cuvette holder. The solutions were prepared on ice to avoid unintentional microtubule assembly. Three microtubule solutions (1.0, 2.0 and 2.5 mg/ml) containing 1 M glycerol and 0.5 mM GTP were mixed in cuvettes with taxol in a ratio of 1 mg/ml tubulin to 10 μM taxol. The cuvette holder was preheated to 37° C before the samples were measured. After 30 min the cuvette holder was cooled down to 0° C to analyze microtubule disassembly, a property describing the extend of microtubule/protein denaturation during microtubule assembly.

2.1.3.5 Gliding assay

The gliding assay was used to check the activity of kinesin. Microtubules are moved by the kinesin motor domains while the kinesin molecules stick to the glass surface with their cargo domains. The concentration of the motor protein was varied in order to select an appropriate kinesin concentration for microtubule alignment within the experimental setup (see section 2.2.3). By measuring the velocities dependence on MgATP (equimolar magnesium ions and ATP) concentration, the Michaelis-Menten constant K_m was determined (chapter 3.1.2).

Microtubules were polymerized by incubating phosphocellulose-purified tubulin (3 mg/ml) for 20 min at 37 °C in the presence of 1 mM GTP and 10 µM taxol acting as assembly promoter. After re-thawing, the purified kinesin had to be stored on ice over night. Otherwise, the velocities could not be reproduced. First, the kinesin (0.125 to 0.25 mg/ml) was incubated for 5 min in bufferA supplemented by 100 mM NaCl and 20 µM taxol. Subsequently, 60 µg/ml assembled microtubules were mixed with MgATP (0.1 to 5 mM). The kinesin/microtubules mixture with a final volume of 10 µl was transferred onto a glass slide pretreated with 5 mg/ml BSA/bufferA and covered by a 10 x 10 mm^2 cover slip. The supplement was observed under the microscope and moving microtubules were analyzed as described in chapter 2.2.3.

2.2 Optical microscopy

The major method used in this work is microscopy. The light microscope is a much-used research tool in biology. It can image the microcosm including entire cells, bacteria, sub-cellular organelles and supra molecular assemblies in their native environment. The light-microscopic visualization of single microtubules is obtained by dark field microscopy, laser scanning microscopy or differential interference microscopy in combination with video-enhanced techniques. This microscopical setup allows real time observations of microtubules [Schnapp 1985]. Force measurements were performed using a singe beam optical trap.

To perform the motility assays *in vitro* and study long range movement a flow cell consisting of a microscopic slide and a cover slip was built. The cell allows solution exchange which was necessary to establish a matrix of isopolar aligned microtubules [Stracke et al. 2000, Boehm et al. 2001]. Such a matrix enables the observation of e.g. beads moving over distances exceeding the length of a microtubule. This case is expected when many kinesin molecules are involved in the bead transport.

2.2.1 Video-enhanced light microscopy (VE-microscopy)

With the development of video-enhanced microscopy during the 1980s [Inoue 1986], light microscopy became a powerful analytic tool. The technique has given access to new visualization possibilities and allows observing dynamics down to the dimensions of the order of 15 nm. The MTs, 25 nm in diameter, are clearly above this limit. The microscope is equipped with a CCD (charged-coupled device) camera, a digital image processor as well as recording and printing devices. Digital processing reduces noise by filtering, averaging and subtracting undesired background patterns. It enhances the contrast and performs measurements like speed and size. It is performed in real time at video frequency and gives electronically optimized images. The enhancement is necessary to follow microtubule movement, to check their assembly and alignment, to visualize the 0.1-µm beads used in the investigation of transport parameters of several motors and to analyze binding rates of beads or the reasons for their unbinding (e.g. end of a microtubule, a barrier or unbinding because of motor protein exhaustion).

2.2.1.1 VE-phase contrast microscopy (VE-Ph)

The technique of phase-contrast microscopy was invented by Zernike in the mid 1930s. The task is to visualize very small phase shifts that can not be detected by the eye which is only able to recognize different intensities and colors. These phase shifts occur, when a light beam passes through a transparent part of an object, where the light travels slower as compared to the uninfluenced one. The optical trick used to translate phase shifts into "grey scales" is the use of a phase stop (a ring shaped mask) in the condenser and a phase ring attached to the objective pupil that matches the incoming light cone. The phase ring induces a shift in the direct light and attenuation relative to the diffracted light. The transparent objects stand out in light colors contrast to its darker surrounding.

Measurements were performed using the inverse transmitted light microscope Axiovert 200M (Zeiss) with a Plan-Apochromat® 100 x oil/1.4 objective (Ph3). The magnification could be increased by using a video zoom multiplier. The generated picture was recorded by a digital camera (C5985, Hamamatsu) and processed by the digitizer Argus 50 (Hamamatsu) following instructions of Weiss and Maile (1992).

In Figure 2.2-1, microscopy pictures that were obtained using the technique of VE-Ph3 microscopy (left figure) and VE-DIC microscopy (right figure) are shown.

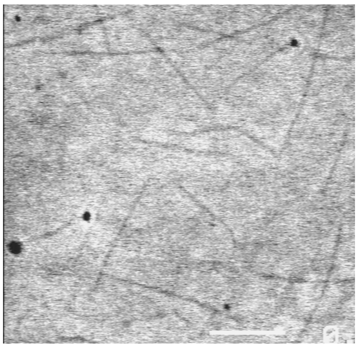

Figure 2.2-1: VE-Ph3 and VE-DIC pictures of gliding microtubules. Left: The VE-Ph3 picture shows random MT gliding (white scale bare equals 7.6 µm). Right: VE-DIC picture taken during microtubule alignment (5.0 µm scale bar).

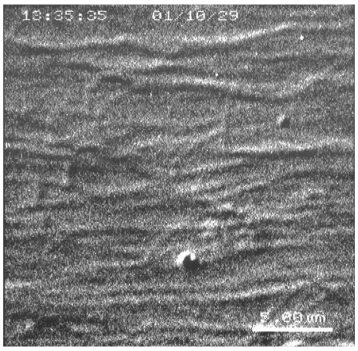

2.2.1.2 VE-differential interference contrast microscopy (VE-DIC)

The concomitant of phase contrast microscopy is the halos of light on structure borders. This implies that the technique is only useful to observe thin objects, as otherwise details may be blended. A technique to overcome this problem is differential interference contrast (DIC) microscopy. The object appears bright and three-dimensional against the dark background. In DIC microscopy the illumination beam of polarized light is separated into two beams by a birefringent Wollaston prism in the condenser. These two beams with the same amplitude are perpendicular to each other. While passing an object, the beams in paths are changed are according to the thickness, slope and refractive index of the specimen. The second Wollaston prism brings the two beams together behind the objective. To obtain interference they need to be in a common vibration plane, which is realized by the analyzer.

Since the invention of differential interference contrast microscopy, individual microtubules can be observed in real time [Allen et al. 1981, 1985].

Measurements were performed using the transmitted light microscope Axiophot (Zeiss) with either a Plan-Neofluar® 63x oil/1.25 or Plan-Neofluar® 100x oil/1.3 objective. The generated pictures were recorded by a Hamamatsu Chalnicon video camera type C2400-0, 1 and image processing system Argus 20 (Hamamatsu). The provided software allowed a direct measurement of the velocity.

2.2.2 Optical trap

Optical Tweezers instruments use light to manipulate microscopic objects. In 1970 Ashkin demonstrated that dielectric particles can be accelerated and trapped by radiation pressure [Ashkin 1970]. Sixteen years later, he discovered a setup that allows trapping of particles via a single, highly focused laser beam, the so called optical trap or optical tweezers [Ashkin et al. 1986]. In this setup the laser light refracts trough a transparent particle where higher forces push the object towards the focal point than pushing it away from it. This occurs if the particle's refractive index is higher than that of the surrounding medium. Optical tweezers are able to catch and hold small particles, and to measure the displacement of objects in the size range from nm to µm. When light is absorbed, reflected or refracted by dielectric material pN-forces are generated. To create a bright laser beam a power in the range of milliwatts is needed, which just allows pN-force measurements.

The Principle is illustrated in Figure 2.2-2. A laser beam, which has a "Gaussian intensity profile", is focused by a microscope objective to a spot in the specimen plane. The light at the centre of the beam is brighter than the light at the edges. The rays travel in the direction of propagation. Any changes in the direction of light, by reflection or refraction due to a bead, will result in a change of the momentum of the light. Two forces arise and act on the bead, the scattering force and the gradient force. The scattering force is proportional to the optical intensity and tends to push the bead along the direction of light propagation. The gradient force is proportional to the intensity gradient, which can be formed near any focus and points toward the centre of the beam, the brighter region of light. The gradient force can overcome the scattering force. It creates an "optical trap", which is able to hold a small particle at its center. A bead is trapped when the gradient force overcomes the propagation force of the laser beam.

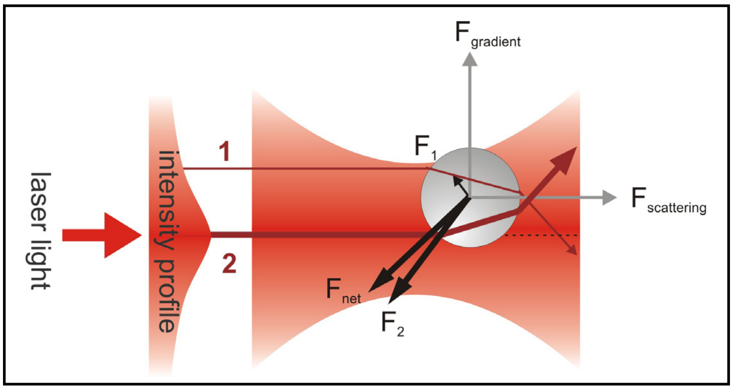

Figure 2.2-2: The principle of optical tweezers. The laser beam is focused by the objective of the microscope to a spot in the observation plane. The bead refracts the two rays shown. The net force on the bead is to the down, in the direction of the intensity gradient (dashed black line). The change in the light intensity is given by the Gaussian distributed light intensity (TEM_{00} beam). Focusing the light, it creates a three-dimensional intensity gradient. The lateral forces balance each other out. The scattering force, which decreases away from the focus, balances the axial force. The net force is towards the focus.

Our optical trap consists of a 5 W infrared laser (1064 nm, TEM_{00} mode, Spectra Physics) combined with a commercial optical microscope (Axiovert 200M, Zeiss). The optical equipment between the laser and the microscope expands and steers the laser beam. A half-wave plate was set in the light path. It acted as a regulator of laser power. Additional power losses are due to the rotation angle of the half-wave plate of 0°, 10° and 15°, where measurements were performed. The microscope objective (Plan-Neofluar® 100x oil/1.3) is used both to focus the beam and to view the trapped object. A high NA-lens is needed for high trapping forces. Trapped beads and their movement out of the trap were monitored via the CCD camera (C5985, Hamamatsu) and recorded on a video tape. Each concentration was analyzed 2 to 5 times and at least 20 beads were observed in each experiment. Force calibration was performed by moving the microscope stage (LStep 13, Maerzhaeuser) at defined velocities, while a bead was trapped. The stage velocity was increased until the bead fell out of the trap. This was repeated three times for each adjusted laser power.

2.2.3 Experimental setup

The experimental setup included a flow chamber with a matrix of isopolar aligned microtubules fixed to the glass surface that constitutes the base for the bead assay.

2.2.3.1 Experimental chamber

The chamber was built using a 76 mm x 26 mm slide (Roth, Karlsruhe) a cover slip sized 24 mm x 50 mm (Roth, Karlsruhe; Menzel, Braunschweig) and double sided adhesive tape (thickness about 0.05 µm). Two 50 mm long stripes of the tape were placed on the slide with a constant distance of either 2.2 or 4 mm between them defining the width of the chamber (see Figure 2.2-3). The different spacing depends on the preparation method used for microtubule alignment (see following section). Although the tape is proved to be inert, the chamber was left to dry over night to avoid effects caused by glue and glue solvents.

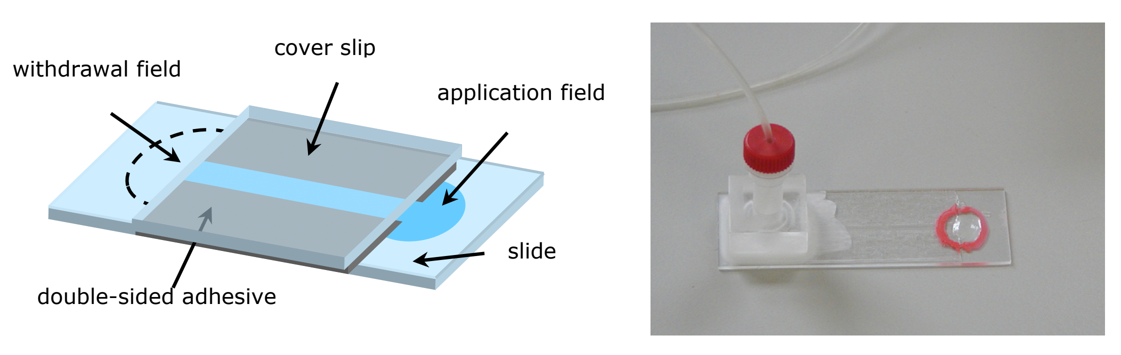

Figure 2.2-3: Flow chamber and chamber with buffer reservoir and tube connection. The chamber was created using double sided adhesive tape fixing a cover slip to a slide. The placement of the two tape stripes and the size of the cover slip define the chamber dimensions. To realize an appropriate flow in a 50 x 4 x 0.05 mm^3 sized chamber a motor-driven syringe is used. The syringe is placed on a punched plastic block which is attached to the flow chamber with paraffin wax. The solutions are placed on the application field (vasiline ring used as a reservoir on the right side of the chamber) and sucked through the chamber.

Before constructing the chamber the glasses, cover slips and slides, had to be pretreated in order to assure effective kinesin binding. First, the microscopic glasses were rinsed with ddH_2O. This was followed by 5 min incubation in ethanol and rinsing with ddH_2O. This procedure was repeated once. The glasses were dried using a pressure airjet. Then, they were placed in a 5 mg/ml BSA/buffer solution for about 7 min, rinsed with ddH_2O and dried again. BSA was used to block unspecific protein binding places at the glass surfaces to avoid nonspecific binding of kinesin (with its motor domain).

2.2.3.2 Microtubule alignment

The run length-experiments were based on matrices of isopolar aligned microtubules. These matrices allow the study of transport distance exceeding the limit of the length of one microtubule [Stracke et al. 2000, Boehm et al. 2001].
The first attempt was to use long microtubules. Therefore, the sample of purified PC-tubulin containing 12 mg/ml tubulin in bufferB (see Table 2.1-3) was incubated at 37° C for one day. The microtubules reached a length of about 100 µm. Then, utilizing the capillary effect, both the microtubules (0.3 to 0.6 mg/ml) and the kinesin (12.5 µg/ml) were transferred into the thin experimental chamber (see above) together with 5 mM ATP, 100 mM NaCl and 20 µM taxol in bufferA (see Table 2.1-2). The conventional gliding assay was realized (chapter 3.1.3.5). While the microtubules were gliding above the kinesin-coated chamber surface a buffer flow was applied to the system to force the microtubules to align in a parallel and isopolar fashion. The used buffer was bufferA supplemented with 1 mM GTP, 0.5 mM ATP and 100 mM NaCl. The microtubules turn with their leading minus-ends into the flow direction. After the alignment, the microtubules were immobilized by 15-min treatment with 0.1% glutardialdehyde in phosphate-buffered saline (PBS). The free aldehyde groups were blocked with 0.1 M glycine/PBS for another 15 min. Unbound glycine was removed by washing the chamber with bufferA. To prevent any buffer flow during the walking distance and force experiments, both ends of the chamber were sealed with rubber cement (Marabu, Tamm).
Within the $50 \times 2.2 \times 0.05\ mm^3$ chamber size, the buffer flow was induced by a motor-driven syringe (50 ml, B. BRAUN, Melsungen) connected to a buffer reservoir on one end of the chamber with a modified tube (Twist top vial, Roth), see Figure 2.2-3. The buffer reservoir was attached to the slide with paraffin wax (Granopent® "P", Roth, Karlsruhe). A simplified method is to simply replace the syringe with filter paper (filter circles ∅ 55 mm, Roth, Karlsruhe). In such a way

generated flow rates were sufficient for the microtubule alignment within the 50 x 4.0 x 0.05 mm^3 chamber size.

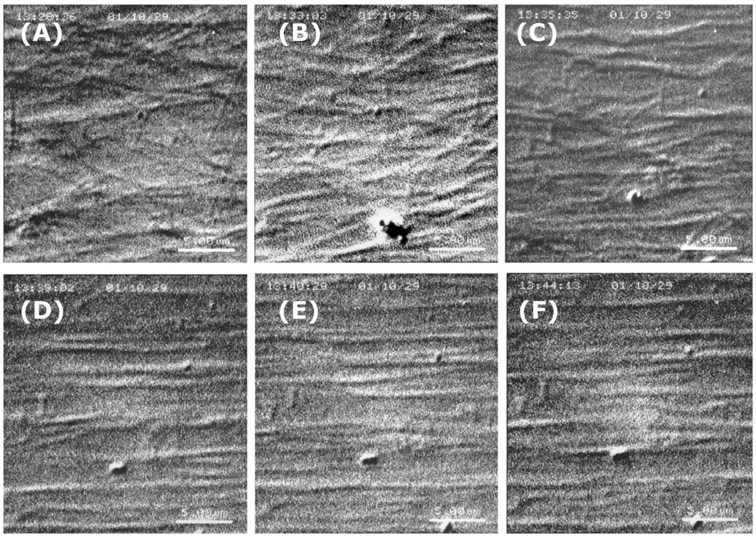

Figure 2.2-4: Isopolar alignment of microtubules. (A) Randomly oriented gliding Microtubules. (B/C) The applied buffer flow turns the microtubules with their minus-ends pointing in the flow direction. (D/E) Microtubules are more and more isoplolar aligned. The kinesin activity is blocked by glutardialdehyde keeping MTs in their position. (F) The chamber is once more washed with a glycine/PBS buffer followed by the experimental buffer solution to maintain the activity of the transport matrix. The white bar corresponds to 5 μm. [adapted from Boehm et al. 2005]

2.2.3.3 Bead preparation and assay

The experiments were performed using carboxylated polystyrene beads (Polyscience Inc., Warrington, PA) with various diameters (see Table 2.2-1). The number of beads in the stock solution was calculated from the mean diameter, the sample volume given by the manufacturer, and the density of polystyrene beads (1.05 g/ml). For the self-binding experiments the number of the smallest beads (D = 0.1 μm) was chosen such that it resulted in a sufficient high number of moving beads even at low kinesin concentration. The bead-stock solution was diluted to 14 pM providing a well defined bead solution where the total bead-surface area is 2.9×10^{11} μm^2/ml. For optical tweezers experiments the bead numbers at comparable bead surface areas for the bigger beads were too high. Thus, the bead working-solution for these sizes had to be diluted (see Table 2.2-1).

Kinesin-coated beads were prepared by mixing the motor protein (final concentrations ranging from 13.5 pM to 270 nM) with a 4 mg/ml BSA/bufferA solution. After 10 min the beads were added, well stirred and left for another 10 min before 5 mM MgATP were added. 10 µl of the bead/kinesin solution were introduced into the chamber and the chamber was sealed as described above.

Donation (beads)	Diameter ± std [µm]	Stock conc. [beads/ml]	Working conc. [pM]	Total bead surface area [μm^2/ml]
0.1	0.1045 ± 0.001	4.22 x 10^{13}	14.0	2.90 x 10^{11}
0.5	0.489 ± 0.013	4.0 x 10^{11}	0.13	6.09 x 10^{10}
1.0	0.984 ± 0.023	5.15 x 10^{10}	0.034	
2.0	2.022 ± 0.046	5.83 x 10^{9}	0.008	

Table 2.2-1: Concentrations and total area of used beads of different diameters. We used four different sizes of carboxylated polystyrene beads. Stock solutions were diluted to obtain approximately the same bead surface area or in the case of the smallest beads, a well defined higher ratio.

The following conditions were realized within the experiments. For the optical tweezers experiments the bead surface area in the chamber was kept constant for every bead size. The bead surface area was approximately 5 times smaller than the one realized for the self binding experiments that used 0.1-µm beads.

The bead transport was observed and forces generated by several kinesin were measured in dependency on the kinesin concentration in solution. In each case the transport of beads was realized along one track.

2.2.3.4 Data analyzes

As explained above, the bead movement was recorded on video tapes. The video sequences (25 frames/sec) were digitized using the imaging analysis system SimplePCI (Compix Ins.), resulting in image sequences of 2 to 5 frames per second. Each picture sequence was analyzed in terms of the covered transport distance and velocity, the numbers of bound and moving beads and the microtubule surface density using a Plug-In for ImageJ[1] (public domain software). By following the movement of the bead, the run length, run time and velocity was calculated.

2.2.3.5 Viscosity and refractive index of the buffer solution

The viscosity of the measurement buffer was determined using a viscosimeter (Lauda, Germany) at a temperature of 25°. A capillary (Ubbelohde, type 1) with a capillary constant of 0.01065 mm^2/s^2 was used. The measurement was repeated three times. The viscosities determined are similar to those for water at this temperature, $\eta = 10^{-3}\ Nm^{-2}$.

The refractive index of the measurement buffer was determined using the refractometer (RE50 Refractometer from Mettler Toledo, Switzerland). About 250 µl of the buffer solution was added to the instrument and the measurement was performed at a temperature of 25° C. The measurement was repeated three times.

2.3 Binding of kinesin to beads

The attachment of kinesin to the carboxylated beads is an irreversible process. Following the protocol of the bead assay and analyzing the binding efficiency of kinesin molecules to the beads in the working solution the molecule-to-bead ratio can be estimated.

The intention was to measure the distribution of molecules on the beads. When the molecules bind to the beads a release or uptake of heat (exothermic or endothermic reaction) is expected. The ITC (Isothermal titration calorimetry, chapter 2.3.1) measures the heat associated with the mixing of two solutions of different compositions. An alternative measurement is based on the load size changes. The bead diameter should increase when the kinesin molecules are

---

[1] The Plug-in for ImageJ was self-written by Dr. Gracia Serral.

attached to the surface. This means a decrease in the diffusion time is expected compared to kinesin-free beads, which can be measured using the DLS (Dynamic light scattering, chapter 2.3.2).

The concentrations of the proteins, beads and solutions used in the DLS-measurements correspond to those in the run length- and force experiments. In the ITC-measurements, due to the measurement sensitivity, many more beads had to be used and therefore higher kinesin concentrations were needed to measure an appropriate signal. The motor-to-bead ratio examined was comparable to the one used during the transport experiments. All measurements were carried out at room temperature (22° - 25° C).

2.3.1 Isothermal titration calorimetry (ITC)

Physical and chemical reactions are accompanied by the release or uptake of heat. Isothermal titration calorimetry (ITC) can be performed to measure the heat changes that take place when associating ligands are mixed and react with their binding partners. It has a big relevance in biochemistry. Interaction strength between ligands and macromolecules such as protein-antigen, antibody-antigen, and hormone-receptor can be determined in their native state [Pierce et al. 1999]. An advantage of the method is the small reaction volume, the high sensitivity (± 20 nW) and fast data acquisition.

The ITC apparatus consist of two separate cells in an adiabatic jacket (see Figure 2.3-1). One is called the reference cell and filled with the buffer solution. The other cell, and called working cell, hosts the same volume of the buffer containing one reactant like vesicles or beads. The second reactant is titrated (typically 5 to 20 µl) to the working cell via a computer-controlled motorized syringe under stirring conditions (rotation of the syringe).

The principle of the ITC is to maintain temperature equilibrium between reference and working cell. The power needed to adjust the temperature difference after the reaction is measured as a function of time. Integrating this power with respect to time yields the heats of reaction of each injection, which is proportional to the number of binding events.

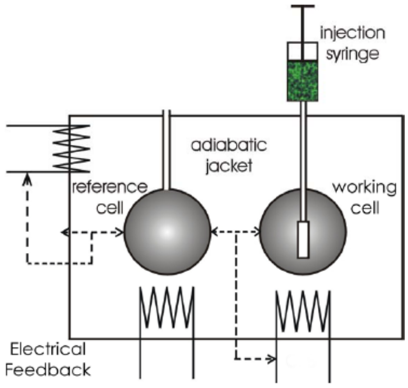

Figure 2.3-1: Diagram of Isothermal titration calorimetry cells and syringe. The apparatus is working in an isothermal and adiabatic environment. This is realized by a differential electrical feedback system. It keeps both working and reference cells at a constant temperature. The third feedback system maintains an equilibrium temperature between the reference cell and the external environment. A syringe with a rotating flat tip injects the reactant into the working cell [the figure was adapted from Sinn 2004].

In this work ITC (VP-ITC MicroCalorimeter from MicroCal, Northhampton, MA) was used to measure non-specific binding of the motor protein kinesin-1 to carboxylated polystyrene beads. One task was to determine the saturation concentration of kinesin. The reference cell was filled with 80 mg/ml BSA/bufferA. The measuring cell contained a BSA/bufferA solution with 0.28 nM beads (0.1 µm in diameter). Both cells hold a volume of 1.4424 ml. In the working cell the reactant was injected via a syringe (total volume of 0.282 ml) driven by a stepping motor. The tip of the syringe is flat and acts as a stirrer. The syringe was rotated with a speed of 310 rpm. The reactant (0.39 µM kinesin) was injected in little aliquots of 20 µl 14 times every 300 s and the released heat was measured as a function of time. The first injection of just 2 µl was ignored. All solutions had been degassed for 20 min and measured at 25° C. Reference measurements were performed using BSA/bufferA as a different injection solution at the same experimental conditions to exclude evolved heat referring to the buffer. The Origin software provided by MicroCal was used to analyze the data.

2.3.2 Dynamic light scattering (DLS)

Dynamic light scattering has proven to be a straight forward method for characterizing the size distribution of particles suspended in a solvent over a size range form 4 nm to several microns. It is based on physical effects that occur when electromagnetic radiation interacts with a material that leads to absorption or scattering of the radiation. Since particles in solution are not static due to Brownian motion, the scattered waves of neighboring particles within the illumination zone will induce constructive and destructive interference. Waves interfere at a distant slit on the face of a photomultiplier detector at a particular scattering angle. The net intensity fluctuates randomly in time where smaller particle show a more rapid fluctuating intensity signal than bigger ones. From the time-dependent intensity signals, the diffusion coefficient can be determined using autocorrelation functions. The diffusion coefficient is needed to calculate the hydrodynamic radius via the Stoke Einstein relation.

In this work, DLS was used to measure the size distribution of carboxylated beads covered with motor proteins. The measurements were performed using the non invasive backscattering ALV-NIBS High Performance Particle Sizer (ALV-Vertriebsgesellschaft m.b.H., Langen, Germany) supplemented with a 2 mW HeNe laser at a wavelength of 632.8 nm and the detector positioned at the scattering angle of 173°. All measurements were carried out at a temperature of 25° C. The analyzed suspensions were prepared as stated in the bead assay (chapter 2.2.3.3). Each suspension was degassed for 15 min to remove air bubbles before 0.8 ml were given to a cuvette (UltraVette, Roth). The cuvette was closed with a sealing film (Parafilm M) to avoid evaporation, fixed to the sample holder and left for 5 min to adjust to the set temperature of 25° C. 5 to 10 measurements lasting 180 s were performed for each kinesin-to-bead ratio. Data signals that showed out of range peaks in the input rate-time diagram where discarded. Such peaks refer to contaminations like dust particles or bead clumps and lead to significant shifts in the bead radius. The data was fitted with a non linear model using the software provided by ALV. The intensity of the unweighted size distribution was obtained by fitting the data with an exponential function. Taking average of the radii at highest intensity, the mean hydrodynamic radius was calculated for each kinesin-to-bead ratio.

Chapter 3

Experimental Results and Discussion

An important issue of molecular biophysics is the complex of the cytoskeleton and its behavior. The cytoskeleton is a network of filamentous protein polymers with motor proteins providing directionality and force needed for transport processes. In mammalian neurons, mainly motor proteins of the kinesin and dynein families carry out fast transport over long distances, for instance in axons. So far, scientific interest has been concentrated on the transport parameters of single motor proteins. Processivity for a dimeric kinesin molecule has been observed, which allows cargo transport over micrometer distances. This is required for the load transport to certain places in the cell in a defined period of time. However, the processivity of single motors is limited. Kinesin-1, for instance, moves about 100 steps, a distance of about 1 µm. When longer walking distances have to be realized more than one molecule has to be involved in the cargo transport, which was the motivation to study the mechanical behavior of several kinesin molecules acting together.

In the presented work, the problem of cooperative behavior of motor proteins during the transport of cargoes is studied *in vitro*, where polystyrene beads of different radii are used to mimic cell organelles. The beads are carried by the motor protein kinesin-1 along a matrix of isopolar aligned microtubules that are fixed to a planar glass surface. Such a matrix of microtubules is a 2D projection of the microtubules in axons of nerve cells. During the studies, where more than one molecule was actively involved in the transport, the following parameters were considered: run length, binding rate, transport velocity, and force exertion.

The results are presented in five main parts.

- In chapter 3.1 properties of the kinesin/microtubule system used are described and characterized.
- The results obtained from the run length-experiments are presented in chapter 3.2. The movement of kinesin-coated beads was analyzed, where the beads would either bind freely, or binding was enforced using optical tweezers. The results obtained include the kinesin concentration- and bead size-dependent run lengths, binding rates of kinesin-coated beads to the track and transport velocities.
- Chapter 3.3 deals with the kinesin concentration-dependent force exertion. Stokes' escape force was measured using an optical single beam trap. The basic principle of the optical trap is presented. Due to different kinesin concentrations on the bead surface the escape force changes.
- Because of unspecific motor-to-bead binding, the experiments were carried out to estimate the number of motors on the bead surface described in chapter 3.4. The methods Isothermal titration calorimetry and Dynamic light scattering were applied to determine the binding energy of molecules and the size change of the bead due to the adsorption of motors, respectively. Additionally, geometrical constraints of the bead size and the molecule structure were taken into account to determine a feasible molecule-to-bead ratio and the effective number of molecules.
- Experimental results combined with theoretical estimates, determine the number of molecules actively involved in the bead transport. The movement properties measured in the run length-experiments and the measured forces are reconsidered and reinterpreted according to these findings in chapter 3.5.

3.1 Properties of the kinesin/microtubules system

Within our study, we used the kinesin/microtubule transport system. The two proteins, kinesin-1 and PC-tubulin are purified from porcine brain. To estimate the molecule number of kinesin in solution a molecular weight, M_{kin}, was considered. The latter was estimated from the molecular weight of KHC, M_{KHC}, and the molecular weight of KLC, M_{KLC}, resulting in 370 kDA ($M_{kin} = 2M_{KHC} + 2M_{KLC}$). The kinesin stock solution had a 2.7 µM molarity which is equivalent to about 1.63×10^{12} molecules/µl.

The critical concentration of tubulin, which determines the minimum tubulin concentration needed for successful microtubule assembly *in vitro*, was measured. The force generation by ATP hydrolysis of kinesin was determined in gliding assays.

3.1.1 PC-tubulin activity

Within cells, i.e., *in vivo*, microtubule shortening and lengthening are active processes determined by cell necessities, e.g. cell division, cell movement and others. Microtubule associated proteins (MAPs) bind to the microtubule surface and promote microtubule assembly [Hirokawa 1994]. *In vitro*, which is the case for experiments performed throughout this work, MAPs are usually removed, because they compete with the motor proteins and influence their motility [Seitz et al. 2002].

To achieve long and stable microtubules *in vitro* MAP-free tubulin (purified PC-tubulin) has to be incubated with GTP and the anticancer drug taxol. The former delivers the necessary energy by hydrolysis, at elevated temperatures (i.e., 37° C). The latter preferentially binds to the polymerized form of the tubulin with exactly one taxoid molecule per tubulin dimer [Diaz and Andreu 1993] and hinders disassembly. Thus, the critical concentration is strongly reduced by taxol application.

An appropriate tubulin concentration for microtubule assembly was determined using turbidity measurements. Tubulin at three different protein concentrations was incubated at 37° C together with equimolar taxol and 0.5 mM GTP. At a wavelength of 360 nm the turbidity was measured as a function of time.

As seen in Figure 3.1-1A, first, an initial lag-phase is observed. This is the so called nucleation phase, where individual tubulin subunits form oligomers that constitute the microtubule nuclei. This is followed by the elongation phase characterized by a rapid microtubule elongation. Free tubulin subunits are added with different kinetics to the microtubule ends until assembly is completed. The system has reached an assembly/disassembly steady state called plateau phase. The turbidity remains constant. It was found that 30 min is an appropriate time to attain complete microtubule polymerization for all the used tubulin concentrations in the presence of taxol. In the absence of taxol (dashed line), no microtubule assembly can be detected. With an increase in the tubulin concentration, an increase in turbidity was measured. That implies more light was scattered and thus more microtubules were built.

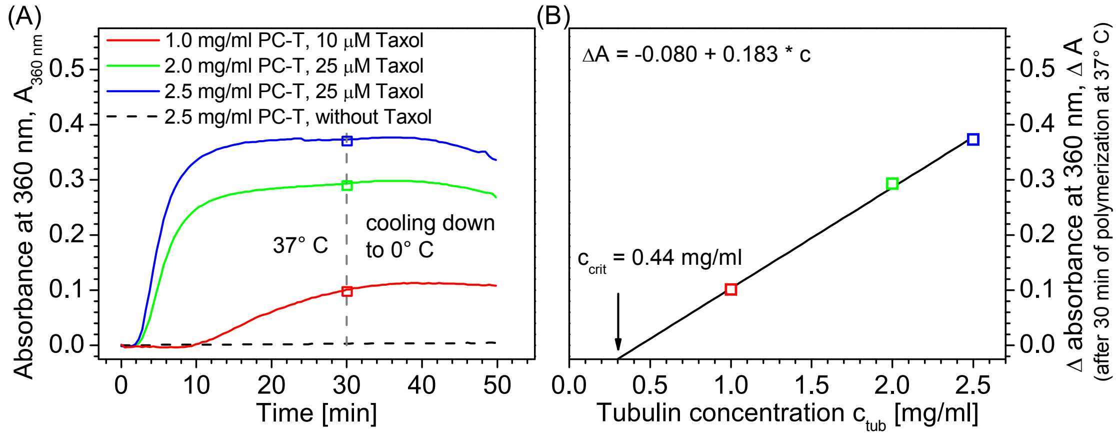

Figure 3.1-1: Critical tubulin concentration measured with the turbidity method. The experiment was performed at a temperature of 37° C for 30 min before cooling the sample down to 0° C. (A) Progress of microtubule polymerization with time depending on the PC-tubulin concentration. The microtubules were either stabilized by taxol (solid line) or the measurements were performed without taxol (dashed line) in the tubulin solution. (B) Change in the turbidity signal after 30 min of polymerization plotted against the PC-tubulin concentration. Linear extrapolation of the data to zero absorbance gives the critical PC-tubulin concentration of c_{crit} = 0.44 mg/ml.

The turbidity signal of each tubulin/taxol solution obtained after 30 min was plotted against the tubulin concentration. Figure 3.1-1B shows that there is a clear linear dependency. Extrapolation to zero absorbance (A_0) gives the lowest tubulin concentration, c_{crit}, at which polymerization is measurable. The analysis shows that more than 0.44 mg/ml of tubulin are needed to observe microtubule assembly. This value is in the same order of magnitude of previous findings [Morejohn and Fosket 1984] and implies that the purified PC-tubulin used for the presented work is free of assembly-incompetent tubulin.

The samples were cooled down to 0° C after 30 min. The starting time is marked with a dashed grey line in Figure 3.1-1A. The microtubule-dependent turbidity values do not decrease. This shows that the microtubules are stable as a result of sufficient taxol/filament interaction.

Based on those results, the purified PC-tubulin stock solutions were diluted to a minimum concentration of 2.5 mg/ml for long time scale assembly of at least 30 min. After this time, microtubules are formed with lengths between 10 and 50 µm and could be used in gliding assay experiments. With even longer assembly times, for instance over night, microtubules of more than 100 µm length were observed under the microscope. Such lengths were preferred for establishing the matrix of isopolar arranged microtubules for the run length-experiments. After the pre-polymerization with equimolar taxol concentration, the microtubule suspension was diluted further to meet the requirements of the experimental approach used.

3.1.2 Microtubule gliding activity

Performing gliding assay experiments, the affinity of the motor protein to its most efficient energy source ATP was measured at room temperature (22 to 25° C). A solution of a constant kinesin concentration (0.34 µM) was incubated with 12 nM taxol-stabilized microtubules before the MgATP was added. The mixture (10 µl) was pipetted onto a slide and covered by a cover slip sized 18 mm x 18 mm, that had been pretreated with 5 mg/ml BSA. Assuming that all kinesin molecules bind to the glass surface, a kinesin density, c^a, of about 3.16×10^3 molecules/µm^2 can be calculated. The average gliding velocity was measured as a function of the MgATP concentration (Figure 3.1-2A, logarithmic scale). The MgATP concentration was varied between 0 and 5 mM. The rate of ATP hydrolysis (one molecule of ATP per 8-nm step), is indirectly measured from the gliding velocity of microtubules. The gliding velocity increased as a function of the MgATP concentration until it reached saturation, following Michaelis-Menten kinetics.

The maximum gliding velocity, $v_{g/max}$, and the dissociation constant, K_m, which is the value for the activation of the kinesin ATPase by microtubules, were obtained using the Woolf-Hanes model, a linear conversion of the Michaelis-Menten model. K_m = 41.1 µM was determined from the x-intercept of the linear fit (see Figure 3.1-2B) was obtained. The maximum gliding velocity is given by the reciprocal slope, $v_{g/max} = 0.963$ µm/s. The results are in agreement with previous studies [Boehm et al. 2000, Howard et al. 1989, Vale et al. 1985].

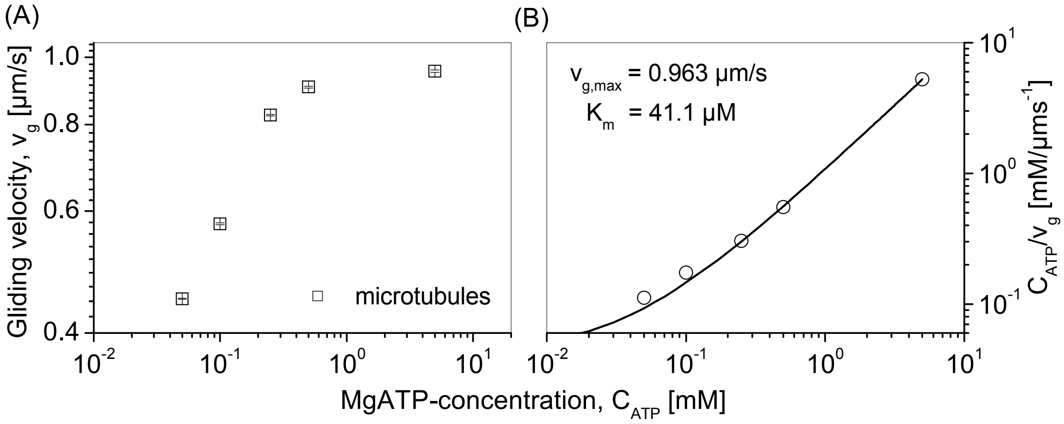

Figure 3.1-2: Relationship between microtubule gliding velocity and MgATP-concentration. Velocities of gliding microtubules were binned into 0.05 µm/s intervals and the average velocities were obtained by applying Gaussian fits to the distributions. The average velocities plotted against the MgATP-concentrations are shown in (A). The progression of the curve follows Michaelis-Menten kinetics. (B) From the linear transform, the Woolf-Hanes model, K_M and v_{max} were derived. The closed line shows the linear fit. Note that logarithmic scale is used in the figures.

Above a concentration of 1 mM ATP, velocities were found to be independent of the ATP-concentration. This ATP-concentration has to be regarded as the saturation concentration for the described conditions. The purified kinesin is active and the microtubules are stable within observation times exceeding one hour. This is important for the *in vitro* experiments, where a stable system is required for long-time experiments.

To perform the motor-number dependent run length and force measurements a kinesin based matrix of long and isopolar aligned microtubules was used. The latter was prepared by orienting kinesin-driven microtubules using a liquid flow. The microtubules move and align in a preferred direction with their minus-ends pointing in the flow direction (see chapter 2.2.3.2). As stated above, for this procedure long microtubule-tracks were favored. Therefore, microtubules were left to assemble for over more than 12 hours. Furthermore, conditions were chosen such as that parallel aligned microtubules show a visible lateral distance of at least the diameter of the observed bead to each other. This ensures bead transport along a single track in the walking direction (see Figure 3.1-3). These conditions were realized using a kinesin concentration of 0.125 mg/ml (0.34 µM), which leads to a density of 5.09 x 10^3 molecules/µm^2 of the glass surface (assuming that all molecules in solution bind). The bead assay was carried out at a MgATP-concentration of 5 mM, which is above the saturation concentration determined.

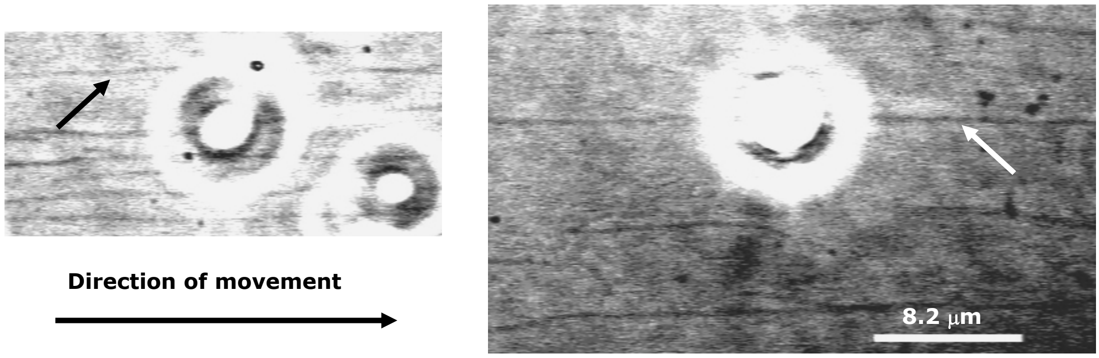

Figure 3.1-3: Bead assay using the kinesin/MT transport system (VE-Ph3 pictures). The microtubules are isopolar aligned and have a lateral side-distance of more than the bead diameter to each other, which ensures bead transport along only a single microtubule track (see arrows). The left picture shows a 0.5-µm bead and the right picture a 2.0-µm bead, which are transported along the marked tracks.

3.2 Run length measurements on beads of different size and motor coverage

Run length, binding rate or binding probability and transport velocity are parameters measured *in vitro* as function of the kinesin-1 molecule concentration.

As an example of measuring the movement properties, the experimental results obtained using small beads (0.1 µm in diameter) are discussed in more detail in the following chapter. The comparison of these data with the results obtained for larger kinesin-coated beads is described in chapter 3.2.2. For the data analysis, just beads with a "clear history" were taken into account. "Clear history" is defined as moving beads that were observed to bind to a microtubule and dissociate without any visible reason. As a consequence of inefficient detection, runs below the limit of 0.25 µm were excluded from the run length-analyzes. For the measurements on binding rates and transport velocities, moving beads with "clear and unclear history" were analyzed. The Latter includes the beads that either moved out of the observation window or beads that moved into strongly bound beads on the microtubule surface or crossing microtubules.

3.2.1 Concentration dependence of motor behavior

The measurements were performed varying the kinesin concentrations between 0.1 and 20.0 µg/ml (0.27 - 54 nM) at a fixed bead size (diameter D = 0.1 µm) and bead concentration (14 pM). In solution, 1 nM kinesin corresponds to about 770 molecules per µm^2-bead surface or 71 kinesins/bead assuming that all molecules adsorb. The movement of the kinesin-coated beads was observed under the microscope. Bead transport from 2 to 5 different locations in the sample was recorded on a tape for 2 to 10 min depending on binding and movement frequencies. The motion of beads was analyzed from image sequences digitized from video tapes. The total number of observed beads per kinesin concentration was between 91 and 333 beads.

3.2.1.1 Average run length

The run length, x_b, of a single kinesin molecule has an exponential distribution [Block et al. 1990, Vale et al. 1996]. All moving beads with "clear history" were binned into intervals of 1 µm to determine the dependence of the kinesin concentration on the average run length, $<x_b>$. The number of moving beads per 1 µm bin, n, was normalized by he total number of all transported beads, N, per kinesin concentration. The obtained bead fraction, n/N, was plotted against the run length. In Figure 3.2-1 the run length-distributions for nine different kinesin concentrations are presented.

In general, with an increase of the kinesin concentration in solution longer walking distances were observed. Where, for example, at a bulk concentration of 0.27 nM kinesin more than 60 % of beads run less than 1 µm, the beads with similar behavior were less than 30 % at a bulk concentration of 13.5 nM. The longest run of 27.67 µm was observed for 6.75 nM kinesin (data not shown). The data determined at the highest motor protein concentration (54 nM) showed a different behavior. According to theory [Lipowsky et al. 2001, Klumpp and Lipowsky 2005], run lengths should increase with the number of motors pulling the bead. Thus, the distribution should shift to higher walking distances. To the contrary, shorter runs were measured again at this motor concentration. About 40 % of the beads were sorted into the 1-µm bin, which are over 10 % more than in the next lower concentration (13.5 nM) analyzed. The idea of overload kinesin concentrations will be discussed in section 3.2.1.3.

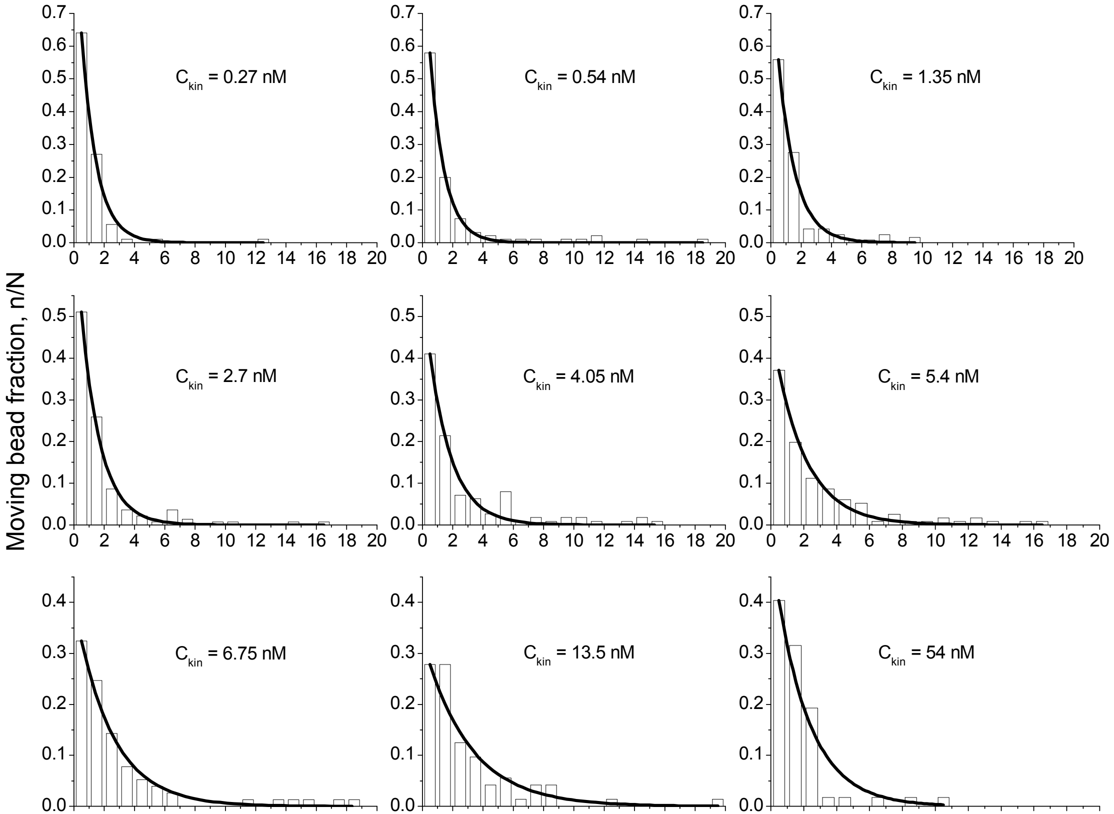

Figure 3.2-1: Histograms of observed run lengths of kinesin-coated 0.1-µm beads with clear history depending on the kinesin concentration. All moving beads were binned into intervals of 1 µm and normalized by the total number of observed moving beads N per kinesin concentration (C_{kin}). Data points above 20 µm run length are not shown. The data was analyzed by applying single exponential decay fits to the run length-distributions (black curves).

The average run length is deduced from an exponential fit to the distribution of the form:

$$\mathbf{n/N} = \mathbf{a}e^{(-\mathbf{x_b}\,/\,<\mathbf{x_b}>)},$$ **Equation 3.2-1**

where a is n/N for beads running less than 1 µm (the first value in the histogram). The average run length, $<x_b>$, was the fitting parameter. The results were plotted against the kinesin concentration (Figure 3.2-2).

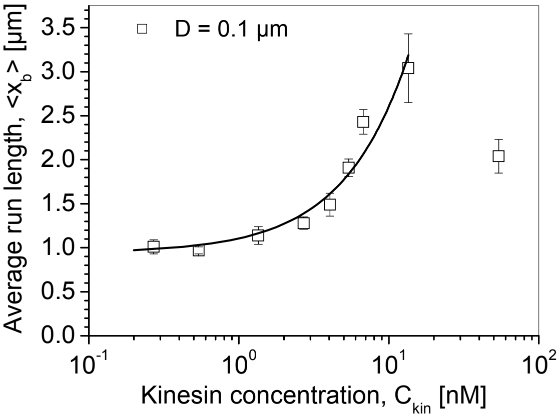

Figure 3.2-2: Average run length (decay constant) as a function of the kinesin concentration. Average run lengths $<x_b>$ were determined by fitting the run length-distributions with single exponential decay functions. The average run lengths, which are given by the decay constants, are plotted against the bulk kinesin concentration (single logarithmic scale). For the first eight motor protein concentrations analyzed, the average run length is nearly proportionally increasing. The decreased run length measured for 54 nM kinesin was significantly different from the other results. This might be due to too many molecules in the working solution that are competing with the bead-bound kinesins for the binding places at the microtubule wall.

In general, a linear increase in the average run length was observed with increasing kinesin concentration, except for the data point at 54 nM kinesin. The maximum averaged run length was measured for 13.5 nM kinesin with a value of 3.04 µm. One can conclude that only a few of the motor molecules were involved in active bead transport. Particularly for lower kinesin concentrations, it is less probable that two motors are close to each other, as the surface area of a bead (3.4×10^{-3} µm^2) is comparable larger. For instance, Block et al. (1990) analyzed kinesin densities (kinesin was purified from squid) between 2 and 130 molecules per µm^{-2}-bead surface (silica beads 0.2 µm in diameter). The measured average run lengths determined at those densities did not change, because the same average number of molecules (mainly one molecule) was involved in load transport over the range of ratios they analyzed. According to run lengths determined, we observed primarily single molecule transport up to a kinesin density of 560 molecules/µm^{-2} bead surface (C_{kin} = 1.35 nM).

3.2.1.2 Binding rate

The binding rate, r_b, of kinesin coated beads to the microtubule was determined by counting the beads that bind and move in a time window of 1 minute with both "clear and unclear history". The number of counted beads was normalized by the total length of all microtubules (µm) seen in the observation window. The results are plotted against the kinesin concentration and shown in Figure 3.2-3.

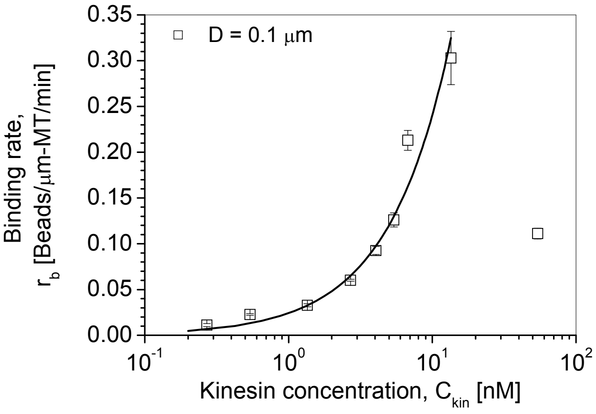

Figure 3.2-3: Curve relating the binding rate to the kinesin concentrations of all moving 0.1-µm beads (clear and unclear history). The frequency of movement (binding rate r_b) within a time window of 1 minute is roughly proportional to the motor protein concentration up to 13.5 nM kinesin working suspension (single logarithmic scale). The total length of all immobilized microtubules (µm) depicted in the particular observation window is used to normalize the counts. The decreased binding rate measured for highest kinesin concentration observed was significantly different from the other results. The behavior is similar to that found for the run lengths.

The binding rate of the kinesin-coated beads is linearly proportional to the kinesin concentration up to 13.5 nM kinesin. The results are in good agreement with previous findings of kinesin-dependent microtubule binding [Schnapp et al. 1992].

Higher kinesin concentrations imply more beads decorated with kinesin molecules and therefore more molecules available for microtubule binding. The data point for the highest motor protein concentration (C_{kin} = 54 pM) again falls out of the general trend and will be discussed in section 3.2.1.3.

3.2.1.3 Average transport velocity

The velocities at defined kinesin concentrations show a Gaussian distribution [Thorn et al. 2000, Seitz and Surrey 2006]. Thus, the results obtained were binned into 0.1-µm/s intervals and the average velocities $<v_c>$ were estimated from the maximum of the Gaussian function fitted to the measured distributions. As an example the velocity distribution of measurements using 5.4 nM kinesin concentration in the working solution is shown in Figure 3.2-4A. In total, 116 beads were analyzed and an average velocity of 0.718 ± 0.013 µm/s (± error of the fit) was calculated.

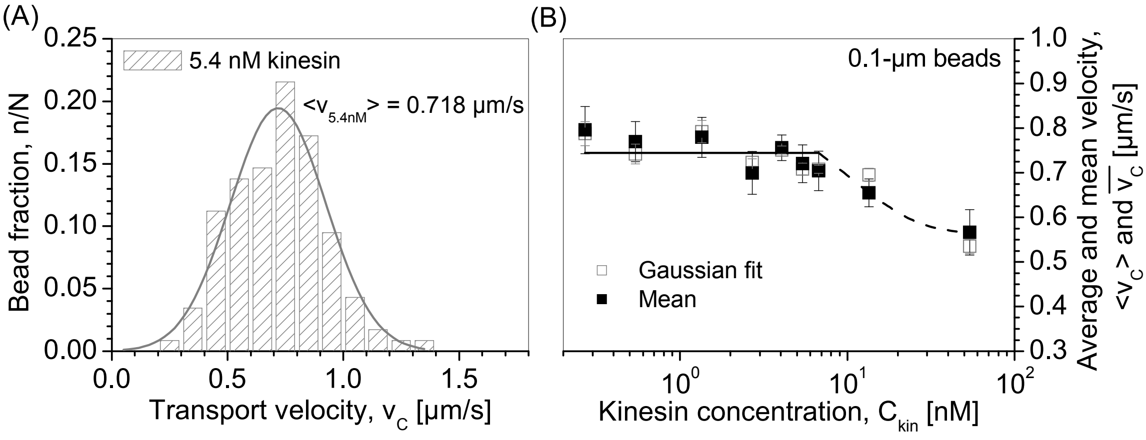

Figure 3.2-4: Dependence of velocity of beads on kinesin concentration. Velocities of moving beads were binned into 0.01 µm/s intervals and the histograms analyzed with single Gaussian distribution functions. (A) As an example, the velocity distribution of beads per 0.1 µm/s bin for a kinesin concentration of 5.4 nM is shown. From the Gaussian fit, an average velocity of 0.718 µm/s was calculated. (B) Average velocities as calculated from the Gaussian fit to the distributions (± error of the fit), and the mean velocities (± error SD) were plotted against kinesin concentration. Although the velocity decreased for comparable high kinesin concentrations (13.5 and 54 nM kinesin, dashed grey line as guide to the eye), transport velocities are motor protein concentration independent at lower motor concentrations in solution, with a mean velocity of 0.744 µm/s (closed line).

In Figure 3.2-4B all observed average velocities are plotted against the kinesin concentration together with the mean values. In agreement with earlier studies on *Drosophila* kinesin-1 [Coy et al. 1999, Seitz and Surrey 2006], the average velocity of kinesin-coated beads did not change significantly with an increase in the motor protein concentration up to 6.75 nM. The mean velocity of 0.744 µm/s is in the order of measured velocities the by these two groups.

In contrast, other groups observed a decrease in the gliding velocity of microtubules with increasing mammalian brain kinesin densities on the glass surface [Hunt et al. 1994, Boehm et al. 2000]. Such a reduction in the transport velocity was observed at higher kinesin concentrations. At the highest motor concentration (54 nM) the beads were transported with an average velocity of 0.535 µm/s, which is much slower.

3.2.1.4 Peculiarities at high motor concentration

The observations at the highest motor concentration (C_{kin} = 54 nM) corroborates the conjunction that too many molecules in solution change the properties of the system. Here we discuss the effect of free motors in dependence on the kinesin concentration.

There must be a saturated state of binding, where the bead surface is completely covered with kinesin molecules. An increase in the motor concentration increases the amount of unbound (free) motors in the solution. These free motors are able to bind to the microtubule too and thus, compete with the bead-bound motors for the binding places on the microtubule [Lipowsky et al. 2001, Klumpp and Lipowsky. 2005, Klumpp et al. 2005]. The molecule overload in solution hinders binding of bead and movement, which was seen within this experiment at the highest observed motor concentration (C_{kin} = 54 nM). Seitz and Surrey (2006) observed similar effects, when they added a second motor construct to kinesin molecules labeled with quantum, but the processivity was unaffected. Different to this we observed a shorter run length again. A possible explanation is that free motors are inactively bound to the microtubule and thus, are obstacles on the track that cannot be overtaken.

From the dissociation constant K_D, which characterizes the binding of free kinesin to β-tubulin of the order of 200 nM [Seitz and Surrey, 2006], free binding sites per motor can be calculated. Dividing K_D by the kinesin concentration in the solution (the motor fraction that is bound to the beads is ignored) results in 4 free tubulin dimers per bound motor. As a further contemplation, we take into account accessible tubulin dimers of immobilized microtubules in the experimental chamber. The concentration of tubulin dimers accessible for kinesin molecules (if 6 protofilaments of a microtubule are considered to be accessible) was in the range of 6 to 32 nM. This results in a range of 2 to 7 kinesin molecules per tubulin dimer, meaning more molecules than available binding places. Forward stepping of kinesin is then hindered by the presence of another motor at the following binding site, which influences the transport.

To sum up, besides the case of the overload conditions explained before, longer runs and more events that are binding were examined with increasing kinesin concentrations. The transport velocity did not change significantly for motor concentrations up to 6.75 nM, but a slightly decrease in the velocity was already measured for a twice higher kinesin concentration in solution.

The stated molecule-to-bead ratios were based on the assumption that all molecules in solution bind. Although these ratios are relative high, we most likely observed single molecule load transport at the lowest kinesin concentrations used. This is confirmed by the observation that at those concentrations, the average run length measured was similar to results observed in single molecule experiments [Howard et al. 1989, Block et al. 1990].

Although the beads we used provide a large surface area in comparison to the size of the kinesin/microtubules transport system, the shape of the loads limits the number of motors being actively involved in load transport (see section 3.4.2). Therefore, the next approach was to perform similar measurements using bigger beads to increase the "active" surface area.

3.2.2 Effect of load size

For comparison to the above results, we used the same bead type, i.e., polystyrene latex beads, but with larger diameters by 0.5, 1.0 and 2.0 µm. For studying the run length, the optical tweezers was used, which allowed a better control of the bead transport. The experimental steps undertaken were as follows. First, a long and bead-free microtubule track was chosen. The track was either a single long microtubule or microtubules aligned and with their opposite ends connected. This construct allowed transport ways of 100 µm length or longer. Then a bead was trapped and placed above a microtubule and the trap was switched off. When a bead was still moving while reaching the end of the observation window, the microscope stage was repositioned to continue the observation and the bead could be followed until it disassociated from its track. Similarly to the experiments with spontaneously binding beads, beads that stopped due to reaching the end of the track or colliding with another bead were not taken into account. Due to the microscope resolution and bead sizes, beads running less than 0.75 µm were discarded, because movement could not be clearly defined. The kinesin concentration was varied between 0.0054 - 2.7 nM, while the bead concentration was kept constant for one bead size. For all bead sizes used the same total bead surface area in solution was realized. 1 nM kinesin corresponds to a ratio of about 3.66 x 10^3 molecules/µm^2-bead surface in the working solution, which, compared to the spontaneously-binding experiments described above, was 5 times higher. As performed for the smallest bead size, the average run lengths and average velocities were determined for the three bead sizes in dependence on the kinesin concentration and the results compared.

3.2.2.1 Average run length

All together, the movement of 448 beads was analyzed for 0.5-µm beads, 601 runs were observed for 1.0-µm beads and 230 for the biggest bead size (D = 2.0 µm). On average, longer walking distances were expected for larger loads at the same motor concentration or molecule surface densities (molecules per µm^2-bead surface).

To analyze and compare the data, individual run lengths of one bead size and kinesin concentration were binned into 1-µm intervals. The cumulative probability distribution is obtained and plotted against the run lengths, see symbols in Figure 3.2-5A.

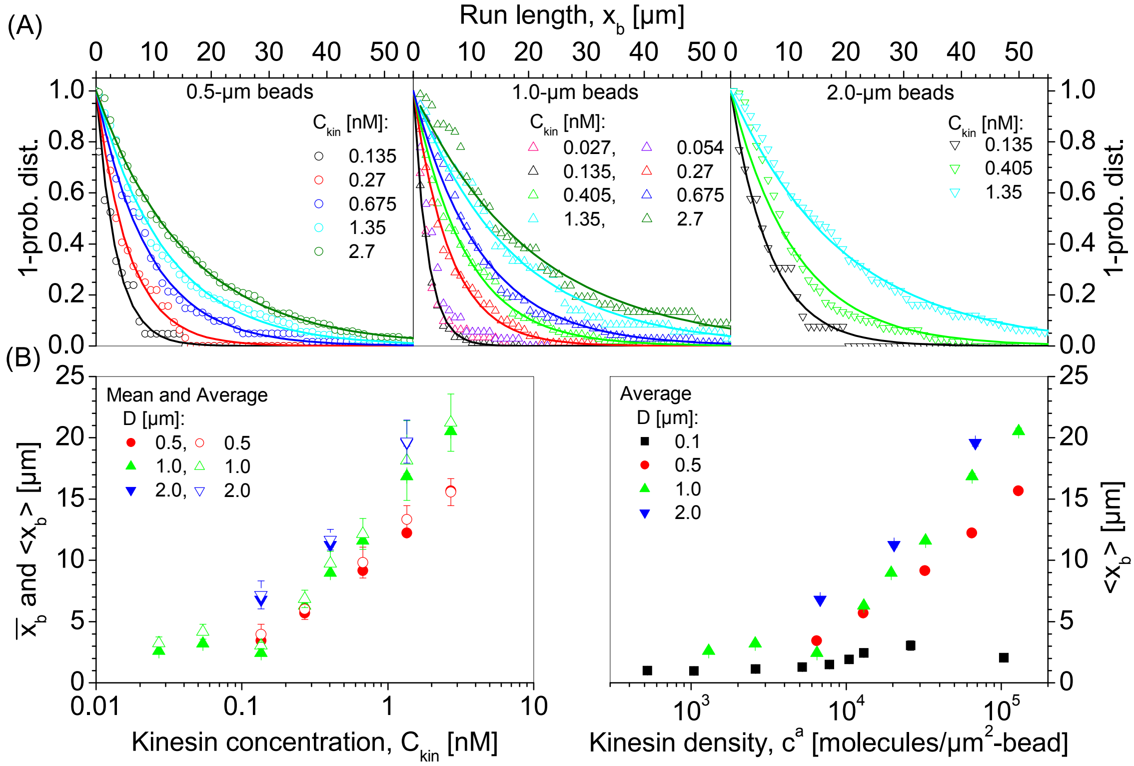

Figure 3.2-5: Run lengths distributions measured for different bead sizes depending on the kinesin concentration and determined mean run lentghs. (A) The 1-probability distributions of induvidual run lengths for the three observed bead sizes (0.5, 1.0 and 2.0 µm in diameter) are plotted against the binned run lengths, the bin size is 1 µm. The solid lines are the results of the single exponential fittings to the motor concentration dependent run length distributions, whereas the decay constant equals the average run lengths. (B) The average run lengths (full symbols, with bars for the error of the fit) together with the mean of the run lengths (empty symbols, with bars for the standard error) per bead size are plotted against the kinesin concentration (left panel) and the molecule density on the bead surface (right panel), assuming that all molecules in solution bind. Longer runs are measured with increasing kinesin concentrations. At similar motor densities on the bead surface longer distances are observed for bigger bead sizes. The data sets are not directly comparable.

The average run lengths were calculated by fitting single exponentials to the probability distributions (solid lines) [Seitz and Surrey 2006], where the exponential decay constant is a measure of the average run length. The kinesin-dependent average run lengths (full symbols) determined for the bead sizes analyzed are shown in Figure 3.2-5B. In addition, the mean of the run lengths, $\overline{x}_b$ (empty symbols), are included in the figure. The results are plotted first, against the kinesin concentration (left panel) and second against the kinesin density on the bead surface area, (right panel), assuming that all molecules in solution bind to the beads. The latter was done to compare the results obtained for the bigger beads with the average run lengths determined using 0.1-µm beads. Within the range of kinesin concentrations used, longer runs were observed for the 0.5- and 2.0-µm beads with increasing motor concentration (left and right panel in Figure 3.2-5B), the probability distributions decay much slower.

This general trend was observed for the 1.0-µm beads too. At low kinesin concentration, $0.027 \leq C_{kin} \leq 0.135$ nM, no significant differences in the run lengths expecting on average the same molecule number carrying the bead was observed. Comparing the results to the binding behavior of kinesin-coated beads to the microtubule at these motor concentrations (see section Figure 3.3-6) single molecule transport can be assumed. Inconsistently to this assumption are the derived average run lengths. Particularly when we compare those values with the results obtained for the smallest bead size (D = 0.1 µm). The run lengths determined for beads 1.0 µm in diameter at low motor concentrations are of similar values as run lengths measured at expected high motor densities on the bead surface of 0.1-µm beads. In this context we should not forget that first, 0.1-µm beads bound spontaneously to the tracks whereas the binding of the larger beads was induced by optical tweezers. Second, it was difficult to differentiate runs shorter than 0.75 µm from single binding events for the larger beads whereas for the smallest observed bead size runs were counted from a distance of 0.25 µm. Average run lengths of the larger bead sizes are therefore slightly overestimated. Moreover, just a small number of 1.0-µm beads were observed moving (32 - 36 beads) at the two lowest analyzed kinesin concentrations.

Nevertheless, at high kinesin concentrations, we determined longer travel distances with increasing bead sizes at similar molecule densities on the bead surface. As an example, we compare the results obtained at a motor density of about 6.8×10^4 molecules per μm^2-bead surface. The 2.0-µm beads have the largest value of 19.58 ± 0.25 µm (± error of the fit) for the average run length. For the 1.0-µm beads an average run length of 16.85 ± 0.25 µm and for the 0.5-µm beads $\langle x_b \rangle = 12.23 \pm 0.11$ µm were measured at similar motor densities. These findings corroborate our belief, that increasing the bead size enlarges the surface, on which kinesin molecules bind, to transport the load together. Concerning the load material, in particular the load shape it can be explained that, using bigger beads a larger area of the beads spans over the microtubule track. In conclusion, more molecules that are attached to the bead surface are able to bind to the microtubule and are probable involved in active load transport, see chapter 3.4.2.

3.2.2.2 Average transport velocity

The second transport parameter we looked at was the velocity. The average velocity was deduced from a Gaussian fit to the binned velocities (0.1 µm/s) for each kinesin concentration and bead size. Additional the mean velocities were analyzed. Similar to the behavior observed for the smallest bead size (0.1 µm), the velocities for each bead diameter were measured to be independent of the kinesin concentration within the error of measurement. The transport velocities of beads of different sizes are plotted against the kinesin concentration, see Figure 3.2-6. For 0.5-µm beads an average velocity of 0.670 ± 0.024 µm/s was measured, 0.610 ± 0.011 µm/s for 1.0-µm beads (N = 528) and 0.622 ± 0.015 µm/s for 2.0-µm beads (N = 196). N is the total number of observed particles.

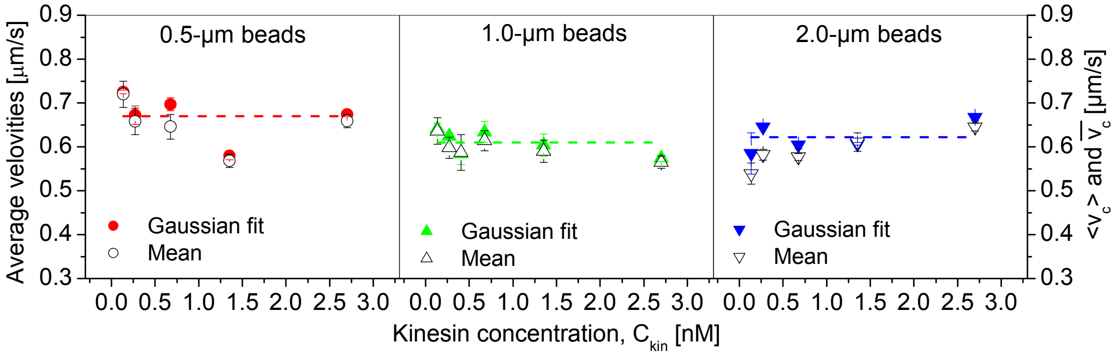

Figure 3.2-6: Average velocities of different bead sizes at different kinesin concentrations. Average velocities as calculated from the Gaussian fit to the velocity distributions (± error of the fit), and the mean velocities (± error SD) were plotted against kinesin concentration. Beads of the same size move at similar velocities independent of the kinesin concentration or number of motors carrying the bead.

The average velocities obtained for the larger bead sizes are approximately the same and somewhat smaller as compared to the velocity measured for the smallest bead size (<v> = 0.744 µm/s for 0.1-µm beads). This observation can be explained by considering the data analyses and the experimental setup. During longer runs, which were observed for the bigger beads, some beads have to change tracks in order to continue their movement because of the limited length of a single microtubule. The step to the following track costs time, which results in a slow down of the average velocity. In this study, an approximate decrease of 0.10 µm/s was measured between the average velocity of the smallest and the biggest bead size. Furthermore, the bigger beads present a heavier load in comparison to the 0.1-µm beads, which could additionally reduce the transport velocity.

The experiments covered kinesin-to-bead ratios, which in the lower limit, correspond to one transporting molecule, as confirmed by the average run length-results of the smallest observed bead size at lowest kinesin concentrations. At the same kinesin concentrations (kinesin density), bigger beads were transported over longer distances implying multi-molecule transport. It is showed that bigger loads, which provide a larger surface area, are transported over distances longer than those observed for smaller beads at the same motor density. Thus, more motors are actively involved in load transport. As already stated, the molecule-to-load binding is unspecific. In chapter 3.5.2 the shown results will be discussed based on experimental results and theoretical considerations concerning the molecule-to-bead binding efficiency, which allow the estimate of motors that are actively involved in the bead transport and furthermore, will allow a comparison of the data sets.

3.3 Force measurements

Optical tweezers are found to be a powerful tool in physics and biology to apply forces in the pN-range. Particles like atoms, molecules and small dielectric spheres can be studied and manipulated without damaging the material [Svoboda and Block 1994, Ashkin 1997].

In this study, optical tweezers were used to prevent polystyrene beads that are covered with kinesin molecules from moving. The force required to escape from the optical tweezers was measured in dependence on the number of motors pulling a bead. The results are shown in the second part of this section. First, the characteristics of the optical tweezers are described.

3.3.1 Characteristics of the optical tweezers and calibration

The optical tweezers used in this work is home-built in a computerized inverted light microscope Axiovert 200M of Zeiss (Jena, Germany) allowing observation in phase contrast and differential interference contrast. In the vertical direction, the microscope focus knob is motorized and computer controlled, allowing displacement of the objective with a 50 nm resolution. The objective used in this work is an oil immersion one with magnification 100× (Plan Apochromat 100×, Ph3, N.A. = 1.4). The microscope is also equipped with a motorized, computer controlled stage (LStep 13, Märzhäuser, Germany) for displacement in the *xy*-plane. A CCD camera (C5985, Hamamatsu) was used for imaging the sample. One of the microscope ports is equipped with an IR camera (LaserCam IIID beam profiler, Coherent, US), for direct visualization of the beam location and quality.

The system is fed by a continuous wave Nd:YAG laser (Spectra Physics, US), wavelength 1064 nm, TEM_{00} mode, with maximum output power of 5 W. The power of the laser beam is regulated by the current supplied to the pumping diode. In addition, the beam power was finely tuned by a half-wave plate positioned at the port where the beam is injected into the microscope. The beam power was measured in front of the objective and in dependence on the rotation angle of the half-wave plate (see Figure 3.3-1). The average loss in power from the Nd:YAG laser head to the pupil of the objective is 86 % at 0° position, 87.5 % at 10° and 89.5 % at 15°. These values were additionally corrected for the power loss caused by the used objective. At a wavelength of 1064 nm, this correction is another 85.5 % [Kraikivsky et al. 2006].

Figure 3.3-1A shows the power-current curves obtained, not taking into account the power losses due to the experimental chamber and the solutions. Calibration of the force was performed by measuring the escape velocity of a bead in a flow. The latter was realized by moving the sample with the motorized stage at a certain velocity (> 0.1 mm/s), while keeping the bead trapped. The displacement velocity of the motorized stage was increased until a critical value $v = v_{esc}$ was reached, at which the particle could no longer be trapped and escaped from the beam. The corresponding trap force is calculated from Stokes' law:

$$F_{esc} = 3\pi\eta D v_{esc} . \qquad \textbf{Equation 3.3-1}$$

For the estimate of F_{esc} for the viscosity $\eta = 10^{-3}$ Nm^{-2} (see chapter 2.2.3.5) and for the bead diameter D = 0.5, 1.0 and 2.0 μm were taken. The measured hydrodynamic Stokes' escape force F_{esc} was found to be linearly proportional to the power of the laser (see Figure 3.3-1C).

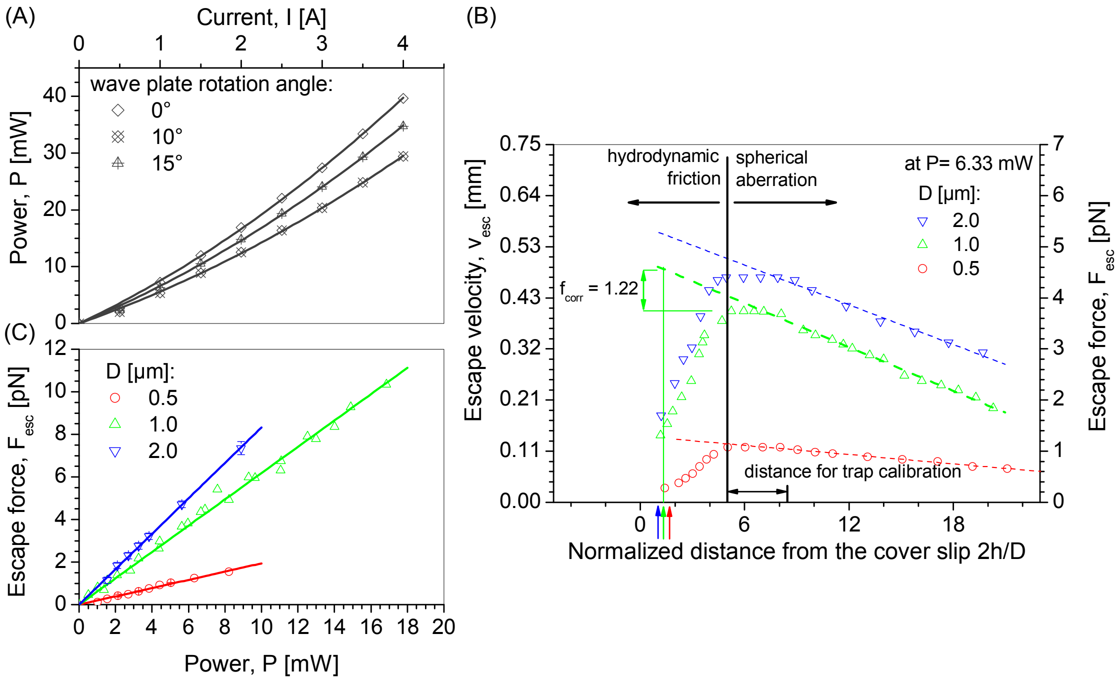

Figure 3.3-1: Calibration curves. (A) The power of the laser beam was measured in front of the objective as a function of the supplied current and the angular position of the half-wave plate. (B) Escape velocities and resultant escape forces were determined for the three beads sizes at different distances h away from the glass surface. The measurements were performed at a constant power of 6.33 mW. At small h the trap efficiency decreases due to hydrodynamic coupling of the particle and the chamber wall. The crossover distance is about 2.5 particle diameters (—). For instance, at distances larger than 15 μm, the 1.0-μm bead cannot be trapped anymore. All experiments, concerning this bead size, were performed at a distance of about 0.66 μm above the cover slip (— for 1.0-μm beads). To determine the escape force at this distance the right branch of the curve was extrapolated to h = 0.66 μm as indicated (dashed green line). The arrows indicate the measurement distance of the other two bead sizes. (C) Force calibration curves were determined for three different bead sizes (D = 0.5, 1.0 and 2.0 μm). Here the maximum escape velocity for each beam power was measured and corrected with a factor deduced from the extrapolation to distances of one particle radius as shown in (B).

As shown in Figure 3.3-1B, the Stokes' force strongly depends on the position of the trapped bead above the glass surface. The distance h is defined as the space between the cover slip and the bead surface. The force is influenced by two effects: Firstly, due to hydrodynamic friction caused by the proximity of the glass surface, the force drops down at small h. Secondly, for large h, the force decreases due to spherical aberrations. The crossover distance is about 2.5 particle diameters. Up to a distance of h = 15 µm above the glass surface, the escape force for 1.0-µm beads was measured and plotted against the corresponding normalized distance 2h/D. At distances between $1 \leq 2h/D \leq 5.5$, the escape force increases with the distance from the chamber wall. This wall effect on the transverse motion of a bead can be corrected by applying a factor to the measured values [Happel and Brenner, 1991]:

$$k = \frac{1}{1 - \frac{9}{16}(D/2h) + \frac{1}{8}(D/2h)^3 - \frac{45}{256}(D/2h)^4 - \frac{1}{16}(D/2h)^5} \quad . \qquad \textbf{Equation 3.3-2}$$

In the limit 2h/D → 1, the hydrodynamic correction for the coupling of the particle with the wall is very sensitive to h. Because of the low accuracy in determining h, we did not attempt to correct the data with the correction factor k. On the other hand, at larger distances, the force is influenced by spherical aberrations [Rohrbach and Stelzer 2002] due to a refractive index mismatch between the glass and the buffer. As stated above, the laser beam is focused with an oil immersion objective. As the focus is moved into the chamber filled with buffer the beam quality deteriorates due to the refractive index mismatch between the immersion oil ($n_{oil} = 1.52$) and the buffer solution ($n_m = 1.334$, see chapter 2.2.3.5).

As mentioned above, the hydrodynamic effect due to the coupling of the particle to the wall is negligible for distances from the glass surface in the range of 2h/D > 5 (no wall effect). Thus, the calibration of the trap was based on the data in this distance range. In particular, the data for 2h/D > 5 was extrapolated down to the distance h at which the experiments were performed (see dashed lines in Figure 3.3-1B). Compared to the maximum value of the escape velocity, v_{esc}, this extrapolation yields a correction factor $f_{corr} = 1.14$ for 0.5-µm beads with $v_{esc,max}$ measured at 2h/D = 1.67, $f_{corr} = 1.22$ for 1.0-µm beads with $v_{esc,max}$ measured at 2h/D = 1.32, and $f_{corr} = 1.20$ for 2.0-µm beads with $v_{esc,max}$ measured at 2h/D = 1.18. Note that the extrapolation correction factor f_{corr} was estimated not for h = 0 but for the particular distance above the glass surface

$h = 2L_{kin} + D_{MT} + D/2$ of the measurement, where L_{kin} is 80 nm and D_{MT} is 25 nm. The data in Figure 3.3-1B was collected for a fixed power of the beam.

To measure the dependence of the escape force on the beam power, the maximum escape velocity was determined and the corresponding correction factor for every bead size applied. Note that these velocities are much higher than the transport velocity of kinesin-coated beads. The resulting force-power calibration curves are shown in Figure 3.3-1C.

3.3.2 Force generation by several motors

Similar to the run length-experiments, kinesin-dependent force generation was observed and measured using the experimental settings described in section 2.2.3. A freely diffusing bead was trapped and positioned above a single microtubule, which appeared to be free of obstacles. The laser power was reduced until the bead could escape from the trap and moved away. The corresponding trap force was recorded. The bead was trapped again and the measurement repeated twice or three times. The average value for the force was determined.

We analyzed between 32 and 47 beads for every kinesin concentration and bead size. The force values obtained were binned into defined intervals, which were depended on different settings of the wave-plate rotation and bead size used.

In the following section, we first discuss the results of the force measured with one bead size (D = 1.0 µm) as a function of the kinesin concentration. Then we compare the force values obtained for different bead sizes at a similar kinesin density per bead surface area.

3.3.2.1 Concentration dependence on force generation

The measurements were performed using beads 1.0 µm in diameter, which were incubated in kinesin solutions at a fixed bead concentration (2.06×10^7 beads/ml). The kinesin concentration was varied between 13.5 pM and 2.7 nM. The trap force was changed in discrete steps. The lowest force values measured correspond to the lowest detectable laser power, $F_{esc} = 0.29$ pN (half-wave plate rotation of 15°), 0.35 pN at 10° rotation and 0.41 pN at 0° rotation.

As mentioned above, only a few beads were observed to escape from the trap at motor concentrations of C_{kin} = 13.5, 27.0 and 54.0 pM. Corresponding escape forces between 0.29 and 1.22 pN were determined (data is not shown). At these motor concentrations, presumably corresponding to single motor experiments (see chapter below), the measured escape force is smaller than expected. In comparison to the known stall force of a single kinesin molecule, $F_s \sim 6$ pN measured by optical tweezers [Svoboda and Block 1994, Kojima et al. 1997, Visscher et al. 1999, Kawaguchi and Ishiwata 2000], the escape forces determined are almost an order of magnitude smaller. Here, it must be pointed out that the force measurements performed by other groups correspond to an experimental scenario that differs from ours. In particular, the stall force measurements imply determining the force needed to stop a walking motor. In this work, the bead was trapped first, i.e., the motor was stopped and then the trapping force was reduced until the motor is released and walks away. In addition to this possible difference between the stall and the escape forces, some concerns about the calibration procedure will be discussed later, see section 3.5.2.

Kinesin dependent escape force-distributions for motor concentrations between 0.135 and 2.7 nM, are shown in Figure 3.3-2. For comparison, individual escape forces determined at different settings of the wave-plate rotation are binned into 0.3-pN intervals where the force distributions obtained for different motor concentrations are plotted in different colors.

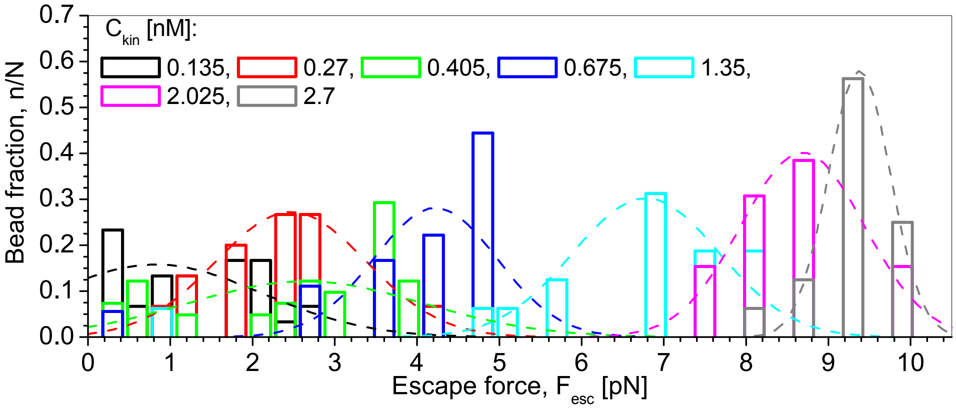

Figure 3.3-2: Force distributions for 1.0-µm beads as a function of the kinesin concentration. The measured escape force were binned into 0.3-µm intervals and normalized by the total number of beads observed at each kinesin concentrations. The dashed lines show the Gaussian fits to these data sets. Kinesin dependent force results suggest multimodal distributions within one kinesin concentration.

In general, at higher motor concentrations higher escape forces are measured. Figure 3.3-3 shows statistical mean force values (black symbols) and the average force values (green symbols) in dependency on the motor concentration. The latter are again the maxima of the Gaussian fits to the force distributions. Other than the distributions shown in Figure 3.3-2, the force values measured were binned according to the setting of the wave-plate rotation (distributions are not shown). Although the distributions are relatively broad, the forces measured for one kinesin concentration are not scattered as the inherent run lengths (see section 3.2.2.1) and their average values are separated from each other. Mean and average forces obtained have similar values and are slightly increasing with increasing kinesin concentrations in solution.

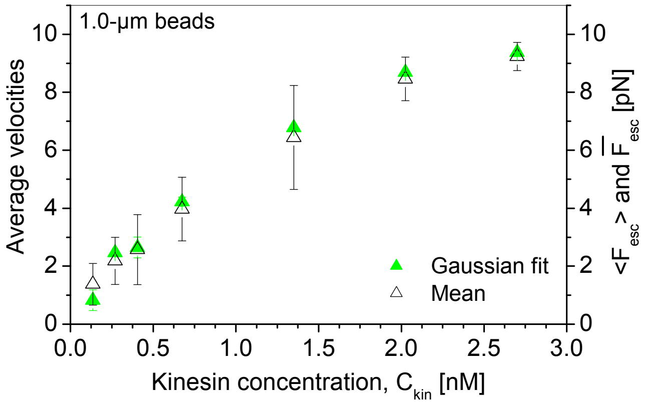

Figure 3.3-3: Average escape forces plotted against the kinesin concentration. To determine the average force values we applied Gaussian fits to the distributions according to the spacing of the applied power for the trap. The average forces (± error of the Gaussian fit) are plotted together with the mean force values (± SD) against the kinesin concentration. The average escape forces increase with the kinesin concentration in solution. An increase in motor-cooperativity is expected.

Considering the results more carefully, one notices that at the lowest motor concentration analyzed (C_{kin} = 0.135 nM) the histogram suggests a bimodal distribution, see black panel in Figure 3.3-4. Individual force values obtained were binned according to the spacing of the applied power of the trap at an angular position of the half-wave plate of 0°. One force peak is determined at approximately 0.5 pN and a second at around 2.5 pN. The latter fits into the force distribution obtained for twice as much kinesin in solution (C_{kin} = 0.27 nM, red bins in Figure 3.3-4).

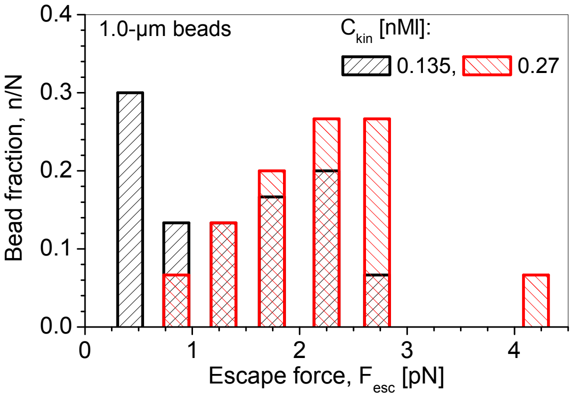

Figure 3.3-4: Force distritribution of 1.0-µm beads at low motor concentration. The force distributions obtained at kinesin bulk concentrations of 0.135 and 0.27 nM are shown. At the lower concentration, two force peaks are determined. The second peak fits nicely into the force distribution obtained for the higher motor concentration of 0.27 nM.

At a kinesin concentration of 0.405 nM (light green bins in Figure 3.3-2) the forces measured are even more scattered and force values could be sorted into three different distributions. The first one is found with a maximum peak of around 0.5 pN. Higher force values fit into the distribution obtained for C_{kin} = 0.27 nM (about 2.5 pN). The third force peak at 3.5 pN might indicate another active motor number or even be assigned to the force distribution determined at C_{kin} = 0.675 nM (dark blue bins in Figure 3.3-2).

Whereas at lower motor concentrations the results are rather scattered and force distributions overlap, only few events that are out of range of the main distribution are determined at the two highest kinesin concentrations observed. In fact, at C_{kin} = 2.025 and 2.7 nM all of the beads escaped at higher forces than those measured before. The force values range from 7.4 to 9.8 pN.

Once again, this behavior is in contrast to the run length results obtained, where distances are much more scattered from one kinesin concentration. For instance, at the highest kinesin concentration observed (C_{kin} = 2.7 nM) run lengths from 1.01 µm up to 81.91 µm were measured, whereas the escape force distribution is relatively narrow (9.24 ± 0.49 pN; mean force ± SD).

Further measurements were performed using 0.5-µm beads. Kinesin concentrations were chosen, for which unbinding events were still observed, $0.135 \leq C_{kin} \leq 0.54$ nM. The measured forces were binned into 0.1-pN intervals at each motor concentration. The normalized distributions obtained are plotted together in Figure 3.3-5A.

The apparent escape forces are comparable to the values found for 1.0-µm beads and are far below the stall force known for one kinesin molecule. The forces measured at fixed motor concentrations are not as widely scattered as those, observed for the bigger beads. Almost all values determined within one motor concentration fit into the main distribution. At the smallest motor concentration observed (C_{kin} = 0.135 nM) a mean force of 0.5 pN, was measured which corresponds to the first force peak obtained at the same motor concentration for the 1.0-µm beads. At the next motor concentration studied (C_{kin} = 0.27 nM) a mean force of about 2.4 pN is determined, corresponding to the main peak at this concentration for 1.0-µm beads. Surprisingly, no significantly higher forces were determined at higher motor concentrations. The force distributions are similar.

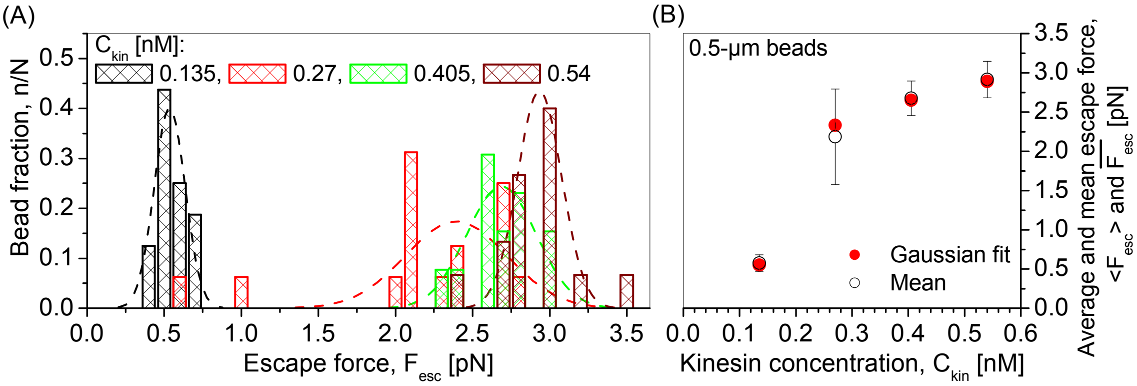

Figure 3.3-5: Force distributions for 0.5-µm beads depending on the kinesin concentration. (A) The measured escape forces were binned into 0.1-pN intervals and normalized by the total number of beads observed at each kinesin concentration. We applied Gaussian fit to the distributions (dashed lines). (B) To determine the average force values Gaussian fits were applied to the distributions according to the spacing of the applied power of the trap. The average forces (± error of the Gaussian fit) are plotted together with the statistical mean force values (± SD) against the kinesin concentration. The escape force increases with the kinesin concentration. For the three higher motor concentrations observed this effect is relatively small.

Comparing the average and mean forces (Figure 3.3-5B), i.e., the maximum of the Gaussian fit and the statistical mean, in dependence on the kinesin concentration it is shown that within the observed motor concentrations two different force values are measured (about 0.5 and 2.5 pN), which can be assigned to two different motor numbers actively carrying the 0.5-μm beads at these concentrations.

Performing force measurements at various kinesin concentration and two different bead sizes it is shown that the escape forces slightly increase with increasing motor concentrations. The results obtained are compared and discussed further in the following section.

3.3.2.2 Effect of load size

Besides the motor concentration in solution, the measured binding probabilities of kinesin coated beads to the microtubules were used as a criterion to compare results from escape force measurements for beads of different sizes (D = 0.5, 1.0 and 2.0 μm) and various kinesin concentrations, see Figure 3.3-7A and B.

First, as an example, the change in the binding probability, p_b, of 1.0-μm beads to the microtubule, which depends on the kinesin concentration, is shown in Figure 3.3-6.
The binding probabilities were determined by counting the binding events of kinesin-coated beads to the microtubule (induced by optical tweezers, see above) normalized by the total number of observed beads per kinesin concentration. It is known that only one kinesin molecule is required for load (bead) transport [Howard et al. 1989, Block et al. 1990]. The binding probability of kinesin-coated beads then corresponds to the Poisson probability that one or more molecules are transporting the bead [Svoboda and Block, 1994]. Our data was fitted to this relation:

$$p_b(C_{kin}) = e^{(-\lambda C_{kin})} \qquad \textbf{Equation 3.3-3}$$

where $p_b(C_{kin})$ is the binding probability, λ is the fitting parameter and C_{kin} the kinesin bulk concentration.

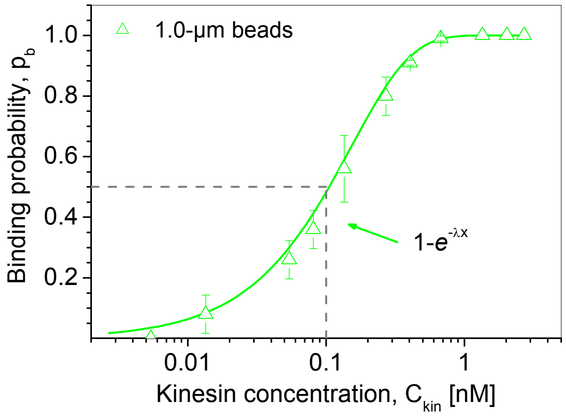

Figure 3.3-6: Binding probability of kinesin-coated beads to the microtubule as a function of the kinesin concentration. The data is fitted to the Poisson probability that one or more molecules are moving the bead. At $p_b \leq 0.5$ single molecule transport is most probable as indicated by the dashed grey lines.

No binding events of beads were observed at a motor concentration of 5.4 pM, but already 8 % of all trapped beads bound to a microtubule at a 2.5 times higher kinesin concentration. As expected and in agreement with former findings fewer beads fail to bind at higher kinesin concentrations until almost all analyzed beads bind ($C_{kin} \geq 0.135$ nM). The knowledge of the binding behavior of kinesin coated beads is used to explore the kinesin concentration, at which one-molecule transport is most likely, $p_b(C_{kin}) \leq 0.5$. Based on this assumption, we consider single motor transport at kinesin concentration less than 0.135 nM. As stated above, no measurement could be performed at low motor concentration due to limits of optical resolution.

For comparison the force results were analyzed at kinesin bulk concentrations, where still no binding of beads to the filament was observed. This was the case for kinesin concentrations up to 0.54 nM for 0.5-µm beads, up to 0.405 nM for 1.0-µm beads and of 0.135 nM for 2.0-µm beads with similar total bead surface areas in solution. At the lowest kinesin concentration observed the mean escape force values determined for different bead sizes are dependent on the bead size, with the highest mean escape force measured for the largest 2.0-µm beads, see Figure 3.3-7A. This is in agreement with run length results determined (see section 3.2.2.1).

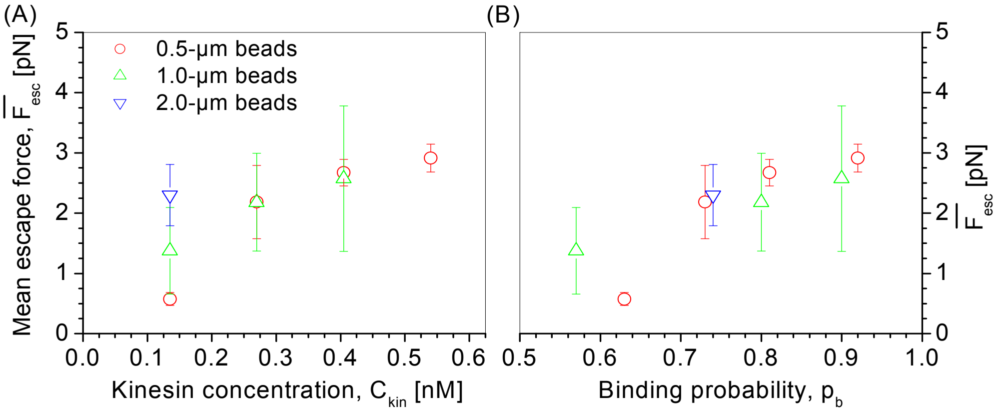

Figure 3.3-7: Mean escape forces of beads of different sizes. Mean escape forces determined for beads 0.5, 1.0 and 2.0 µm in diameter are plotted (A) against the kinesin concentration in solution and (B) against the binding probability of kinesin coated beads to the microtubule. At similar binding probabilities similar forces values are determined and effect of the size of the bead at the smallest observed kinesin concentration is eliminated.

The effect of the bead size is eliminated when the mean escape force values are plotted against the binding probability (see Figure 3.3-7B). At similar binding probabilities similar force values are obtained. Thus, the binding probability seems to be an indicator for the number of motors pulling the beads of various sizes at low motor concentrations. The results suggest at least two possible motor numbers. This is even more obvious when we analyze single force results with respect to the measured binding probabilities and independently of the bead size.

Figure 3.3-8A shows the force distributions obtained for binding probabilities in the range of $0.55 < p_b \leq 0.7$, $0.7 < p_b \leq 0.85$ and $0.85 < p_b < 0.92$. For comparison, single force results are binned into 0.6-pN intervals and normalized by the total number of beads analyzed in the respective binding probability-regimes.

The force distribution obtained at the lowest binding probabilities analyzed (black bins) shows a main force peak at 0.6 pN. At the other two binding probability-regimes, the force distributions do not differ significantly. This becomes more obvious, when the overall force distribution is plotted (Figure 3.3-8B). This was obtained by summing the bead fractions and normalizing the values by the number of included force distributions (three in this case). Applying a Gaussian fit to the distribution results in a force peak at about 2.7 pN (closed line). One can conclude the lowest mean escape force measured, $F_{esc} \sim 0.6$ pN, is the escape force generated by a single kinesin molecule, whereas at an escape force of 2.7 pN two motor proteins on average are actively pulling the bead out of the optical tweezers.

The run lengths measured (> 3 µm) at assumed single molecule transport are above the value know for one kinesin molecule. This effect is already discussed in section 3.2.2.1).

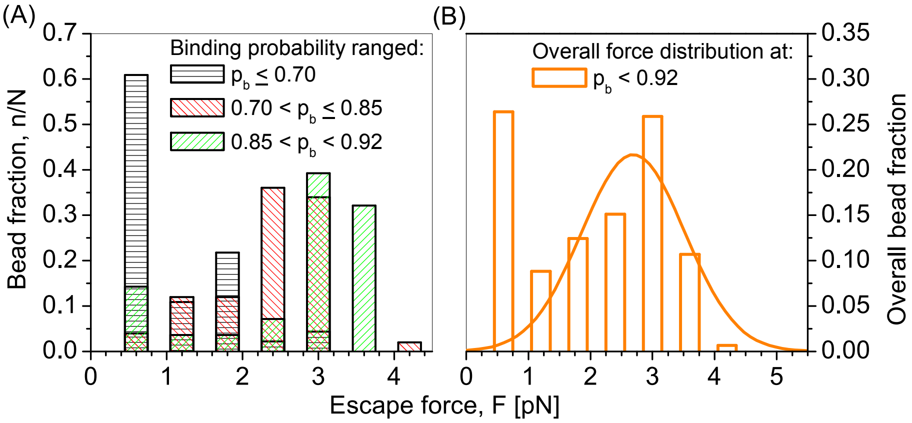

Figure 3.3-8: Force distributions in dependence on the binding probability. (A) Independent of the bead size, single force results that are measured at defined binding probabilities (three different ranges) are binned into force intervals of 0.6 pN. The force distribution obtained at the lowest binding probability-range (black) shows a main force peak at 0.6 pN. The force distributions obtained at the other two ranges are similar. (B) The overall force distribution is determined for binding probabilities below 0.92. The distribution suggests two main force peaks, at about 0.6 and 2.7 pN, implying one and two molecule transport respectively. The latter force value was obtained by applying a Gaussian fit (closed lines) to the force distribution.

The trend is that the mean escape forces increase with the kinesin concentration in the bulk solution suggesting that more molecules are involved in the bead transport at higher motor concentration. For the smallest bead size analyzed (0.5-µm in diameter), we determined distinct distributions at each motor concentration. In contrast to this, for the 1.0-µm beads the data was much more disperse, but it seems that the "out of range" values can be sorted into the distributions obtained for previous and/or following kinesin concentrations. To overcome the problem of unknown molecule concentrations on the bead and furthermore the unknown number of effectively working motors, the binding of kinesin-covered beads to the microtubules were used and found to be an appropriate parameter to characterize the active number of motors active in the transport. If single-molecule transport is assumed at a measured escape force of about 0.6 pN, then the value is far below the stall force obtained from single kinesin molecule-experiments. Above, a certain kinesin concentration (C_{kin} = 0.675 nM) almost all beads that are observed bind to their microtubule tracks and show movement. Hence, the parameter binding probability becomes inapplicable.

In the following chapter, we introduce methods and results addressing the issue of active motor numbers, which may allow a more precise analysis of the data.

3.4 Stoichiometry of kinesin-bead binding

To demonstrate and compare the dependence of run length and force exertion on the kinesin concentration, the data was plotted against the kinesin bulk concentration, also referred to as molecules per bead or molecules per bead surface ratio. The given ratios are based on the assumption that all molecules within the working solution bind to the beads.

As already stated, we used a comparatively high concentration of kinesin molecules with respect to the bead concentration. Literature observations report that a 2:1 molecule per bead concentration ratio should be employed to observe single molecule transport [Block et al. 1990, Coy et al. 1999]. However, our results for run length-experiments show that even at concentration ratios (c^a) as high as 20 molecules/bead, single molecule behavior is observed. For bigger beads, this ratio was even higher. Thus, it is expected that not all molecules in solution are active. Motors do either not bind to the bead at all or, if bound to the bead, they have no hydrolyzing activity.

One approach to determine the kinesin binding efficiency and to estimate the actual binding stoichiometry was to measure the binding heat released when motor molecules attach to the bead surface. This was done using Isothermal titration calorimetry (ITC). Another experimental approach was based on measuring the change of the bead size due to binding of the kinesin molecules. The hydrodynamic radius of proteins and colloids can be measured using Dynamic light scattering (DLS). When proteins bind to beads, the shape and size should change as a result of additional components on the bead surface. The size change is limited by the bead surface area and a saturation state in the increased bead size can be measured. This, together with constraints imposed by the molecular geometry and bead size, allows ascertainment of a realistic, feasible molecule number on the bead surface at a defined kinesin concentration.

This chapter introduces the experimental approaches applied to answer the question about the realistic molecule-to-bead ratio. Further, the experimental results are reconsidered, taking into account geometrical considerations and properties of the used proteins and loads. Both, experimental results and theoretical approaches lead to a concentration dependence of the molecule-to-bead ratio and furthermore a limit for the number of molecules, which are actively involved in the bead transport.

3.4.1 Experimental considerations of kinesin-to-bead binding

The crucial point of the measurements is the non-specific process of kinesin-to-bead binding. To quantify the number of motors attached to one bead two experimental techniques were applied. The first one, ITC, measures the heat release caused by the adhesion of the motor molecules to the bead surface. With an increase in the number of kinesin molecules in the bead solution the signal is expected to decrease due to fewer available binding places on the bead. The second technique is DLS, which measures the hydrodynamic radius or Stokes’ radius of colloidal particles. This method accounts for an expected change of the bead size when motors are bound. Similar to the ITC-measurement, a saturation value is expected when motors create a kind of layer around the bead surface at total coverage conditions and then no more change in the bead radius should be detected.

3.4.1.1 Binding of kinesin molecules to beads (ITC studies)

The isotherm of motor molecule binding to polystyrene bead surfaces, which are modified with carboxyl groups and which were pretreated with BSA, was measured with Isotermal titration calorimetry. The results were obtained by titrating aliquots of an 0.39 µM kinesin solution in 0.28 nM bead solution of 0.1-µm beads, (see section 2.2.3.3 for definition of bead concetration). The choice of these concentration was limited by the amount of protein available. Lower bead concetrations cannot be used because the heat signal would be too low. The heat change measured following the stepwise addition of kinesin molecules into the bead solution was plotted against the molecule-to-bead ratio, which is shown in Figure 3.4-1A (solid squares).

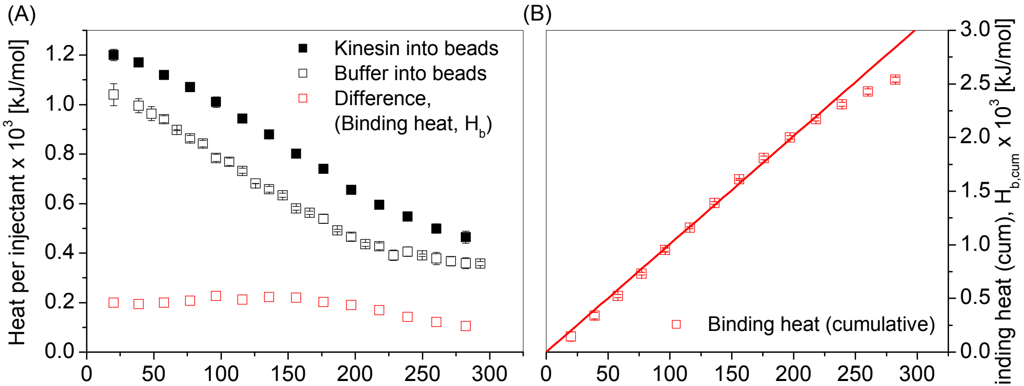

Figure 3.4-1: Heat per injection as a function of the molecule-to-bead ratio. (A) Heat was obtained from integrating the heat flow over time. The reference measurement (open black squares), where buffer solution was injected into the bead solution, was performed to detect dilution effects. The data obtained by injecting the kinesin molecules into the bead solution is also shown (closed black squares). The difference of the two signals is the heat associated with the kinesin molecules binding to the beads (open red squares). (B) The cumulative heat release caused by kinesin binding to polystyrene beads is plotted against the molar ratio.

In order to determine the heat associated with the molecule binding to the beads, the heat of dilution was measured by just titrating the working buffer (bufferA) in the bead solution. The heat values obtained (open black squares in Figure 3.4-1A) were subtracted from the total enthalpy, which was determined by titrating the kinesin solution into the bead solution (closed black squares in Figure 3.4-1A). The difference (open red squares) is denoted as binding heat, H_b. The binding heat for the first injections measured was constant within the error of the measurement indicating that the motors could freely bind with the equal binding probability. This is more obvious when the cumulative binding heat, $H_{b,cum}$, per molecule-to-bead ratio is plotted, see Figure 3.4-1B. A linear fit to the first data points could be performed resulting in a binding heat of about 10 kJ/mol, which is quite a weak bond. At a molar ratio of about 220 molecules per bead a decrease in the binding heat was detected. At this ratio the beads in the measuring cell of the ITC are already satisfactorily covered and it becomes more difficult for the newly injected motors to attach to the bead surface. From this molecule ratio on, the binding heat seems to reduce with every new injection. Total coverage of the beads with kinesin molecules was not observed at the ratios used. As mentioned above, the full coverage (complete bead coverage) was not accessible due to the concentration constraints. At the saturation state, no measurable binding heat could be detected with further kinesin injection.

The experimental setup of the ITC measurements requires a comparatively high concentration of motor proteins due to the sensitivity of the instrument. It implies that enough binding events have to occur to measure a signal per injection. Using the ITC-method, we were not able to reach the concentration of kinesin molecules necessary to create a tightly packed layer around a 0.1-µm bead. From Figure 3.4-1A it is obvious that at the ratios analyzed a similar binding heat was measured, that were for almost every injection of the kinesin solution. This is due to a constant number of motors binding to the bead surface with each injection and results in the linearity of the cumulative binding heat (see Figure 3.4-1B). Only with the last three injections, the released heat measured decreases presumably because the bead surface is becoming saturated with motors.

Compared to the motor-to-bead ratios used in the run length-experiments our ITC-data covers only a small interval of molar ratios. The maximum ratio obtained in the ITC-measurement was less than one-tenth of the maximum ratio analyzed in the run length-experiment. This limit is imposed by the minimum protein concentration necessary for obtaining a strong signal. One can conclude that binding events are expected at molar ratios exceeding 300 molecules/bead. This is in agreement with the results of the run length-experiments, where the longest average run length was observed at a molar ratio of about 965 molecules/bead in solution.

3.4.1.2 Size distribution of kinesin-coated beads (DLS studies)

The Dynamic light scattering (DLS) experiments were performed to measure the change in the mean radius of the beads as a result of the binding of kinesin. DLS measures the hydrodynamic radius of particles. With higher numbers of molecules on a bead, the bead size is expected to increase until the bead is completely covered with motors. When the molecules are tightly packed and extending away from the bead with their total lengths the maximum change in radius should be equal to the size of the kinesin molecule, i.e., about 80 nm.

The measurements were performed at room temperature. The DLS-measurement was performed simultaneously with the transport experiments. No time dependence was detected over the different measurements, i.e., within an incubation time of 2 h. Thus, we can conclude that:

- the time for preliminary incubation of the beads with the kinesin was long enough to complete the absorption process,
- the kinesin molecules bind strongly to the bead surface and similar motor numbers were expected over the period of time the run lengths- and force measurements were performed.

The size-distribution of the reference measurement (— 0) was determined for kinesin-free beads in BSA/buffer. As figures Figure 3.4-2A, B and C demonstrate, a maximum size shift with increasing kinesin concentration as compared to the reference is observed. For the lowest concentrations (0.27 and 0.54 nM) the shift is relatively small compared to the size distribution of kinesin-free beads. This slight change can be attributed to the few molecules bound, but it is most likely that some beads are still motor protein-free, because the slopes of the three curves are similar. For the kinesin concentration of 0.135 nM no detectable difference from the reference solution was observed, either because that no molecules bound or because of the insufficient technique sensitivity. With increasing concentration, the distribution curves shift to larger radii. The shape of the distributions does not change, which reflects homogenous binding to all beads in the sample and no clustering of kinesin molecules.

The small peak with an average hydrodynamic radius of 3.73 ± 0.03 nm can be attributed to the BSA-molecules (bovine serum albumin). Because of its large number of accessible amino acids, BSA adsorbs strongly to the surface of particles, forming a closely packed layer known to promote kinesin binding. The measured hydrodynamic radius is in agreement with results obtained from gel filtration chromatography experiments [Andrews 1970]. For the observed bead concentrations, BSA seems to be in excess, which is why a peak in the DLS measurements appears. After we doubled the bead concentration and thus, doubled the particle surface area accessible, the BSA-peak was no longer detected. Similar was observed when the concentration of BSA was halved at a bead concentration used during the run length-experiments. The bead size did not change under this conditions compared to the reference measurement. One can conclude that a stable layer of BSA is formed on the bead surface and BSA molecules in excess do not bind to the beads. The fact of all BSA molecules bound to the bead can be excluded because even at a dilution of BSA to one-eighties of the initial concentration size changes due to the molecule were measured.

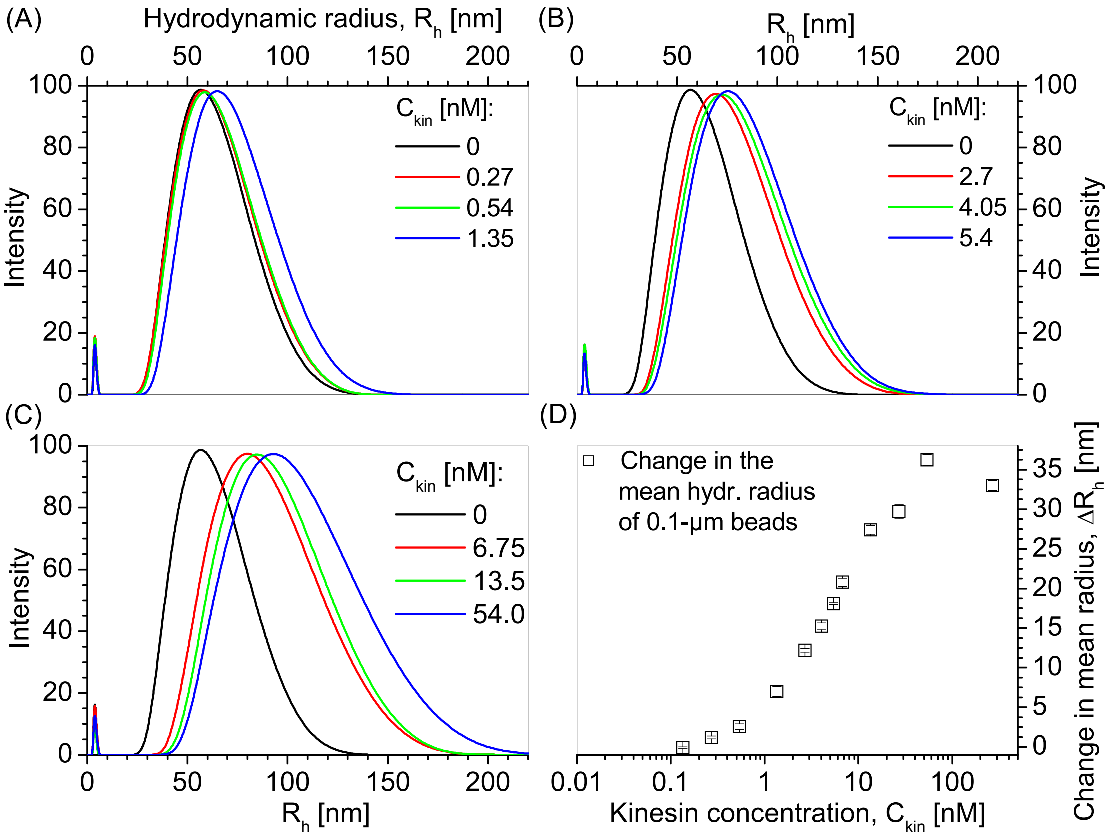

Figure 3.4-2: Kinesin density dependent change in the hydrodynamic radius R_h of the 0.1-µm beads analyzed via DLS. Figure (A), (B), (C) show the unweighted size distribution intensities. The changes of the mean radii as compared to the size of kinesin-free beads (— 0) were plotted against the kinesin concentration pictured in plot (D). As expected, an increase in the bead size (bead size change) could be observed for higher molecule numbers in the working solution at a constant bead concentration. The values tend to saturate at high kinesin concentrations indicating complete bead coverage with the motor protein (single logarithmic scale).

Kinesin molecules alone could not be detected in the BSA/bead solutions, although free molecules in solution were expected at higher kinesin concentrations. In comparison to the other two components, BSA and beads, the molecule number of kinesin in solution is too low (less than one-fifties of the BSA molecules) to be detected by light scattering instruments. This is confirmed by results from BSA-bead-binding measurements. Where changes of the bead size were observed at comparable low BSA concentration to the initial concentration, already at one-half BSA concentration free BSA molecules could not be detected.

Measurements of bead-free solutions (in absence of BSA) with kinesin at 6.75 nM concentration showed a weak peak at a hydrodynamic radius of 9.67 ± 0.76 nm, but reference measurement of the plain buffer did not show a peak in this size range. We conclude that this signal is due to the kinesin molecules in the buffer solution. The size is inside the range given by Bloom et al. (1988) as corresponding to bovine brain kinesin molecules (with kinesin light chains) in their folded state at an axial ratio of 20:1. The fully extended molecule has an axial ratio of 40:1 [Hackney et al. 1992].

The average hydrodynamic radius of the reference measurement (kinesin-free bead solution), $\langle R_0 \rangle$, was subtracted from all mean values, $\langle R_{ch} \rangle$. The change in the bead radius,

$$\Delta R_h = \langle R_{ch} \rangle - \langle R_0 \rangle, \qquad \textbf{Equation 3.4-1}$$

was plotted against the kinesin concentration (see Figure 3.4-2 D). As already stated and apparent from the distribution curves, the bead size increases with the kinesin concentration. For the two highest motor protein concentrations analyzed (54 and 270 nM), no change in the radius was observed. That implies that at such concentrations the beads are completely covered with kinesin molecules. According to our assumption this change in the radius should correspond to the extended length of the kinesin molecule. From the slope of the curve, we deduce a maximum change in the radius, $\Delta R_{h,max} = 34.61$ nm, which less than the half length of the kinesin. This fact will be discussed later (Figure 3.4-4).

The previous results demonstrate that with higher molecule-to-bead ratios the hydrodynamic radius of 0.1-µm beads increases due to more molecules bound to its surface. We were able to determine a maximum kinesin concentration of 54 nM, at which saturation of the bead surface occurs, but no unbound kinesin molecules could be detected in the bead solution.

Similar behavior was found for 0.5 and 1.0-µm beads, too. Performing experiments with bigger beads required the usage of higher kinesin concentrations (higher molecule-to-bead ratios), because of the larger area for adsorption provided by larger beads. Thus, motor-dependent size changes of 2.0-µm beads were not studied as they required very high motor concentrations to observe size dependence.

The kinesin dependent results of the DLS-measurements for all three bead sizes were plotted against the kinesin-to-bead ratio in solution. The changes in the hydrodynamic radii are shown in Figure 3.4-3. The curve shapes are similar. The hydrodynamic radius and thus the change in radius increases until it reaches saturation. Saturation was observed for the smallest bead size used (see above) and for the 0.5-µm beads. For the latter the maximum change in the radius was larger ($\Delta R_{h,max}$ = 51.18 nm) by about 16.6 nm as compared to the smaller beads. Although no saturation was measured for 1.0-µm beads for the kinesin concentrations used the radius at saturation is expected to be larger.

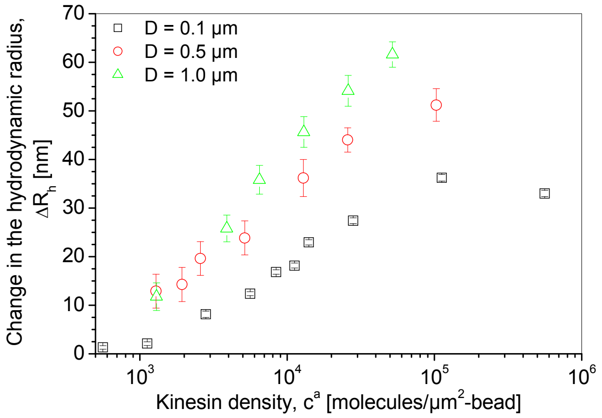

Figure 3.4-3: Bead size and kinesin density dependent change in the mean hydrodynamic radius. The kinesin concentration dependent bead radii were normalized by the measured kinesin-free bead radii and were plotted against the molecule-to-bead surface density. For the two bigger bead sizes used higher molecule densities had to be chosen to measure a change in the radius. In addition, it was observed that with increasing bead sizes the maximum change in the hydrodynamic radius increased as well (single logarithmic scale).

The increase in $\Delta R_{h,max}$ with the beads size could be explained as follows. The curvature of beads decreases with increasing sizes. When the rod-like kinesin molecule binds with its cargo binding site to the bead surface, the rod itself has more space to explore and bend. Thus, the molecule density per unit of area away from the bead surface is different for different bead sizes. A certain distance away from the bead surface the molecules are less densely packed for small beads than for large beads (see scheme in Figure 3.4-4; both beads are decorated with kinesin molecules at saturated conditions, meaning full coverage of kinesin molecules on the bead surface). And therefore, the change of hydrodynamic radius of smaller beads is smaller than the one of bigger beads at similar kinesin molecule densities on bead surfaces. The binding space a molecule requires can be described as a frustum with the smaller area towards the bead surface. According to our measurements, the area away from the bead is larger for smaller beads. Conversely, the height of the "frustum" is smaller when the volume space a molecule requires is independent of the bead size.

It should not be forgotten that the DLS signal intensity depends on the refractive index difference between particle and medium. Thus, a less densely envelope of molecules has a lower refractive index difference and will effectively result in smaller differences of the particle radius.

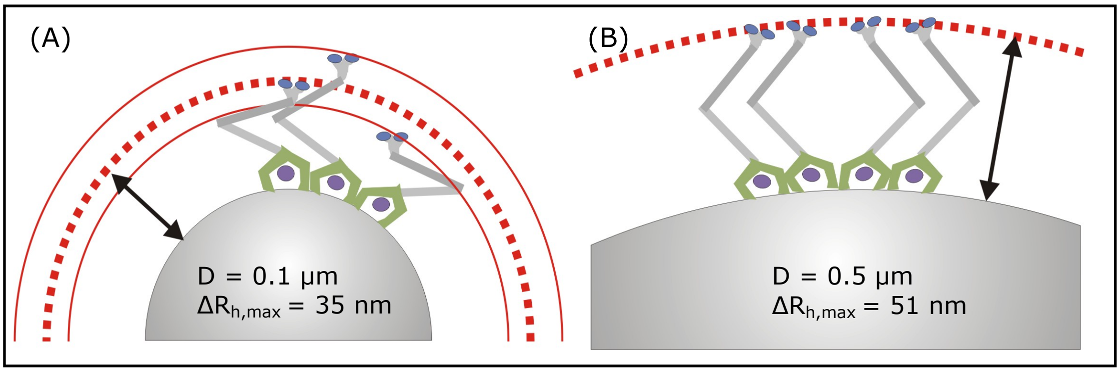

Figure 3.4-4: Scheme of molecules bound to curved surfaces. At full coverage of a bead with motor molecules, the space explored by the molecules decreases. The bigger the bead, the less flexible the motor can be. The motor is more elongated. Even though the same conditions are realized on the bead surface, different maximum changes in the hydrodynamic radius should be measured. Scheme (A) shows a bead about 0.1 µm in diameter with motors of an approximate length of 80 nm. The dashed red lines represent the distribution of new sizes of the bead due to the bound molecules. Scheme (B) shows a five times bigger bead. It demonstrates that the bound molecules have less space for bending and thus at total coverage the mean change in the radius must be bigger.

The results of the DLS measurement show changes in the bead size that depend on the kinesin concentration. Based on the assumption that there is no further interaction between the adsorbed molecules and the molecules in solution, and that kinesin builds a constant coating on the bead surface at full coverage, the resulting volume change was fitted using the Langmuir-adsorption model (see following chapter 3.4.2.1). At higher kinesin concentrations, a point is reached where the bead is fully coated. Adding more motors will not increase the bead size, hence the levelling out is observed in the graph. This results in the maximum kinesin concentration or the molecule-to-bead ratio. The maximum molecule-to-bead ratios in solution (c^b) determined are up to about 1 x 10^4 molecules/bead for the smallest observed bead size (D = 0.1 µm) and 7.8 x 10^4 molecules/bead for 0.5-µm beads, assuming that all kinesins in solution bind to the bead. The molecule-to-bead ratio for the biggest bead size analyzed with DLS (D = 1.0 µm) was not measured but was approximated according to the progression of the fitting curve, see the following chapter.

3.4.2 Geometrical constraints on kinesin-to-microtubule binding

Isothermal titration calorimetry and Dynamic light scattering were performed to determine the kinesin concentration dependent number of molecules binding to the bead surface. With ITC, we characterized the enthalpy because of molecule binding. At small molecule-to-bead ratios, a constant heat release for every consecutive binding event was measured. The signal decreased at a ratio of about 220 molecules per bead, suggesting exhaustion of the binding space (see Figure 3.4-1). Because of the relatively large kinesin concentration required, a saturation state was not reached. The latter was obtained by measuring the kinesin concentration dependent radius change of the beads with DLS. The corresponding molecule-to-bead ratios will be analyzed and discussed in the following chapter where, additionally, will be taken into account geometrical parameters of the motor and the load.

3.4.2.1 Maximum molecule number on the bead surface – comparison of experimental results and theoretical approaches

All experiments were performed using BSA-pretreated polystyrene beads as load material. The beads are assumed to be monodisperse and spherical at each bead size. For calculations, the sizes measured for beads covered with BSA (reference measurement) were used. To estimate the maximum number of kinesin molecules that can bind to the bead surface, N_{max}, following relation was used:

$$A_b / A_{mol} = N_{max} , \qquad \textbf{Equation 3.4-2}$$

where A_b is the bead surface area and A_{mol} the area the kinesin molecule requires for binding. Kinesin binds to its cargo via the cargo domains (CD) and, in our case, also the KLCs (kinesin light chains), as suggested from the electrophoresis (see section 2.1.3.1) and DLS-measurements of single kinesin molecules [Bloom et al. 1988]. The KLCs have a fan-like structure and surround the two cargo domains (see Figure 3.4-5).

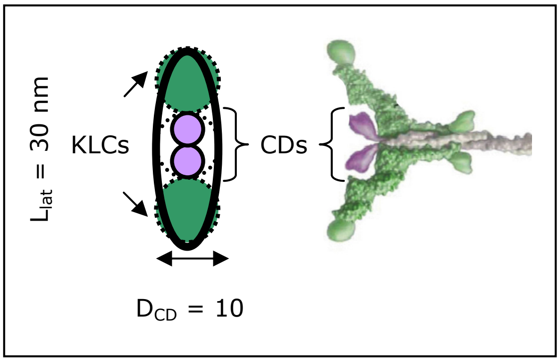

Figure 3.4-5: Scheme of the top view of kinesin cargo domains (CDs) and kinesin light chains (KLCs) forming the cargo binding site. The binding area of the KLCs and CDs can be represented as an ellipsoid area. The area is defined by the lateral extension of the fan-like KLCs and the size of the CDs. The side view of the cargo binding site of the kinesin molecule is adapted from Vale [Vale 2003].

Kinesin is composed by two KLCs, surrounding CDs of total diameter ~ 10 nm. During binding the projection area occupied by a kinesin molecule, A_{mol}, can be approximately represented as an area of 10 nm x 30 nm (diameter of the KHC cargo binding site, D_{CD}, times the lateral extension of the combined sizes of KLCs and CDs (cargo binding site), L_{lat} [Amos 1987, Mandelkow and Mandelkow 2002, Vale 2003] characterized as follows:

$$A_{mol} = \frac{L_{lat}\,D_{CD}}{4}\pi\,. \qquad \textbf{Equation 3.4-3}$$

Dividing the bead area by the molecule area the maximum number of molecule per bead, N_{max}, is calculated for each bead size used (see Table 3.4-1).

DLS measurements. As already stated, the DLS measurements determine the change in the hydrodynamic radius R_h as a result of the bound kinesin molecules. This corresponds to a volume change, $\Delta V = V_h - V_0$, where V_h is the volume obtained from the measured R_h, and V_0 is the volume of the kinesin-uncovered bead. According to the assumption, the volume increment should be proportional to the number of the bound kinesin molecules. ΔV was plotted against the kinesin molecule-to-bead ratio, c^b, which is derived from the kinesin concentration rescaled by the bead concentration. The dependence was fitted using the Langmuir adsorption model:

$$\Delta V(c^b) = V_{max}\frac{c^b}{c^b + K_{1/2}}, \qquad \textbf{Equation 3.4-4}$$

where $K_{1/2}$ is the molecule-to-bead ratio at which half of the total change of the volume is measured and V_{max} is the maximum change of the volume at molecule saturation on the bead surface. The latter parameter, V_{max}, is proportional to the maximum number of molecules which can bind, N_{max}, as calculated previously (Equation 3.4-1). According to the Langmuir model the current number of adsorbed molecule per bead, c^b, was rescaled to:

$$N_b = N_{max}\frac{c^b}{c^b + K_{1/2}}\,. \qquad \textbf{Equation 3.4-5}$$

In Figure 3.4-6A the volume change based on the results from the DLS-measurements is plotted against the molecule-to-bead ratio for all bead sizes (D = 0.1, 0.5 and 1.0 µm) analyzed.

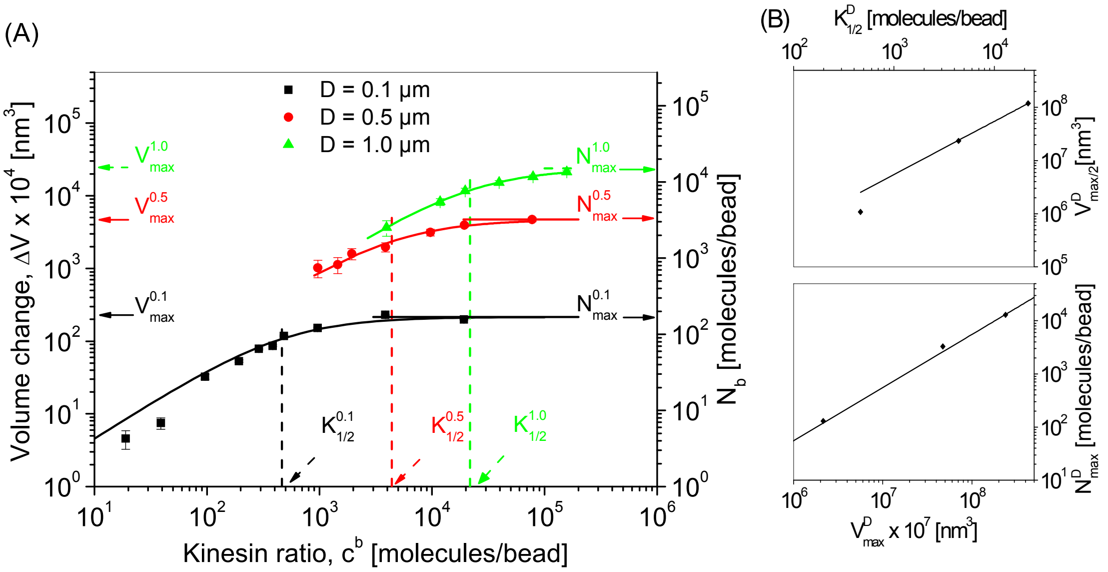

Figure 3.4-6: Volume change of beads due to bound kinesin molecules. (A) The volume change was calculated from the results obtained from DLS and plotted against the molecule-to-bead ratio assuming all molecules have bound to the bead surface. The data is fitted with the Langmuir-adsorption model and rescaled to the accessible molecule number on the bead surface (see right axis). For 1.0-µm beads, the fit was used to determine the maximum change in the volume. (B) The dependence of observed volume changes at half-maximum for the three observed bead sizes (upper figure) and linear dependence of accessible molecule numbers on the bead surface to the maximum volume changes determined is shown.

For the two smaller bead sizes, the parameter V_{max} is fixed at measured maximum change in radius at saturation conditions (horizontal solid line) while performing the Langmuir model. The only fitting parameter was $K_{1/2}$, the binding constant at half-maximum volume change. Two fitting parameters, V_{max} (horizontal dashed line) and $K_{1/2}$, are used to analyze the volume change of the 1.0-µm beads. The left axis in the diagram shows the calculated volume change. The solid curves are the fits according to Equation 3.2-2 and the vertical dashed lines show the kinesin ratios, $V_{1/2}$, at half-maximum volume change.

The bead size dependent relations of the parameters obtained are shown in Figure 3.4-6B. We plotted the half-maximum of the volume change, $V_{max,2}$, against the derived rate constants (upper figure) and the assumed maximum accessible number of molecules on the bead surface against the maximum volume change obtained (lower figure). This results in the already assumed proportional dependence of the average number on the bead to the volume change, which allows us to determine the total number of motors at the bead as a function of the kinesin ratio in solution. Respectively, we can calculate the volume of one kinesin molecule by dividing the maximum volume change by the maximum number of molecules assumed and estimate the length of the motor, which should be equal to the radius change at the maximum. Dividing the volume of one molecule by A_{mol} (see Equation 3.4-3) results in a motor length of 60 - 80 nm, which is a little higher than the measured values ($\Delta R_{h,max}$ = 35 - 62 nm, see Figure 3.4-2). Note that as a simplification a cylindrical volume space (instead of frustum) is assumed, which explains higher values.

The calculated parameter, N_{max}, that is bead size dependent, and parameters $K_{1/2}$ and V_{max} that are determined with DLS-measurements for the bead sizes analyzed (D = 0.1, 0.5 and 1.0 µm) are shown in Table 3.4-1. The measurement error was between 5 and 12 % for $K_{1/2}$ and 1.5 % for V_{max}.

D [µm]	N_{max}	V_{max} [nm^3]	$K_{1/2}$ [kin/nm^2]
0.1	130	2.15×10^6	464
0.5	3300	4.71×10^7	4400
1.0	1.3×10^4	2.38×10^8	21750
2.0	5.3×10^4	no analyses	

Table 3.4-1: Parameters obtained from estimates and DLS-data fits. In dependence on the bead size, the calculated maximum accessible number of molecules on the bead surface is shown; the maximum volume change and the kinesin ratio at half-maximum volume change that was observed by applying the Langmuir-adsorption model to the kinesin ratio-dependent mean volume change are also displayed.

It is shown, that only a small fraction of molecules in the working solution binds to the bead surface. Even at the lowest kinesin concentrations observed just 20 % of the molecules in solution attach to the bead surface. Thus, free motors are left in solution and could be competing with bead-bound motors for free binding places on the microtubules and therefore influence the transport properties.

ITC-measurements. If the measured cumulative binding heat is plotted against the derived volume changes for similar molecule-to-bead ratios in solution ($19 \leq c^b \leq 289$ molecules/bead) it is observed that the values are proportional to each other, see Figure 3.4-7. This allows the comparison of the DLS-based analyses obtained for the smallest bead size observed (D = 0.1 µm) with the result obtained from the ITC-measurements in dependence on the kinesin ratio.

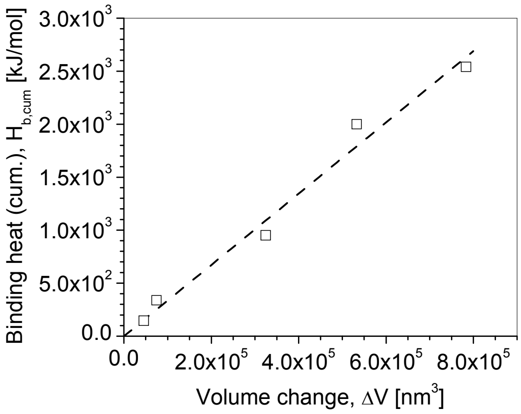

Figure 3.4-7: Comparison of the cumulative binding heat with the volume change. The obtained cumulative binding heat (ITC-measurement) is plotted against the measured volume change (DLS-data) at similar molecule-to-bead ratios in solution. The cumulative binding heat is proportional to the volume change.

In Figure 3.4-8A the ITC-data marked with red squares and the data determined with DLS (black squares) are shown.

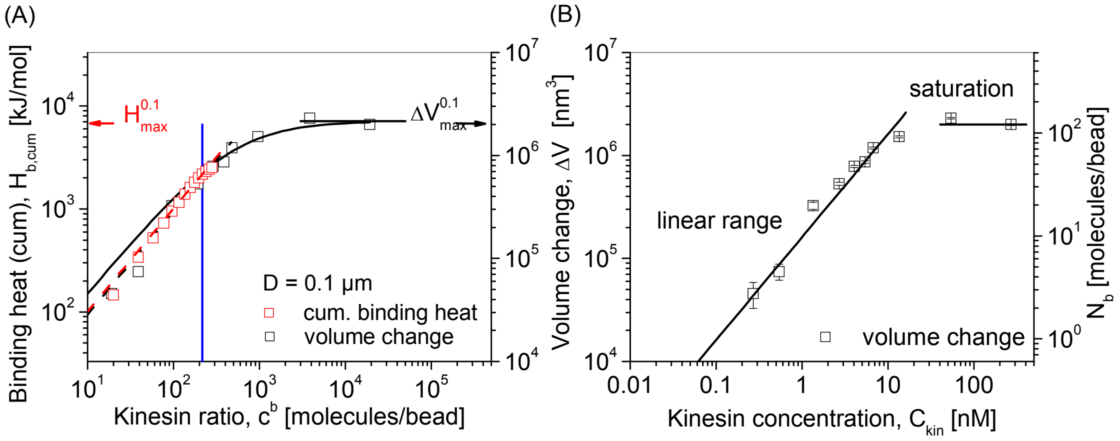

Figure 3.4-8: Comparison of the DLS-based analyses with the results determined using ITC. (A) Kinesin number dependent cumulative binding heat determined using ITC (red symbols, left axis) and volume change according to the measured radius changes of the beads determined with DLS (black symbols, right axis) are plotted against the molecule-to-bead ratio in solution. The solid black curve shows the fitting curve to the volume change based on the Langmuir-adsorption model. Because a linear behavior is expected for the volume change and the binding heat, the maximum binding heat can be obtained. At low kinesin concentrations the molecule-to-bead binding is approximately linear. Linear fit was performed up to a kinesin ratio corresponding to the result obtained in the ITC-measurement (blue line). (B) Volume change (left axis) and corresponding molecule number on the bead surface (right axis) is plotted against the kinesin concentration. In the low kinesin concentration range the volume change is assumed to be proportional to the number of molecules that bind to the beads

The molar ratio accessed in the ITC- measurement was much smaller than the in the DLS-measurement and the corresponding run length-experiments, because of comparably high kinesin concentration that are required to measure the binding heats. Furthermore, the cumulative binding heat was observed to change linearly with the molar ratio (dashed red line) whereas the Langmuir model was fitted to the DLS-results (solid black line). The blue, vertical line marks the molecule-to-bead ratio up to which a linear cumulative binding heat was observed with ITC (logarithmic scale is used in the figure). The proportionality of both data sets allows to perform a linear fit to the DLS-results at the same molecule-to-bead ratios (up to $c^b \sim 200$ molecules/bead; see dashed black line). The result is satisfactory. Within the error of measurement, both interpretations of the DLS results (Langmuir model and line fit) are valid to rescale the molecule-to-bead ratio for low kinesin concentrations. At linear dependence 11 molecules per 1 nM bulk concentration attach to the beads for an assumed maximum of 130 molecules per bead in the low motor concentration range (up to 6.75 nM) (see Figure 3.4-8B).

For large kinesin concentrations, it is shown that molecule absorption to the bead surface follows the Langmuir-adsorption model. The same behavior of the curve behavior should be observed with ITC, the cumulation binding heat is assumed to saturate at higher kinesin ratios. Thus, a maximum binding heat can be determined. In the measurement it leads to an energy release of about 6.5×10^3 kJ/mol. At a maximum number of 130 molecules it is a binding heat of about 50 kJ/mol or 19 k_BT per kinesin molecule, which is five times stronger than initially deduced from the results of the ITC measurements (see section 3.4.1.1). This value for the binding heat is comparable to strength of the non covalent bonds. The value is above the energy required for a kinesin molecule to perform a step against a 7 pN load (up to ~ 12 k_BT) [Schnitzer et al. 2000, Block et al. 2003]

Binding efficiency of motors to the bead surface. Additional measurements and considerations allow the rescaling of the bead size-dependent molecule-to-bead ratios. It is obtained by replacing the measured change in the volume of each bead size due to the attached kinesin molecules by an estimated limited maximum number on the bead surface in the Langmuir adsorption equation. Based on this relation we obtained a corrected molecule-to-bead ratio. This number however, is not compulsory equal to the number of molecules that are actively involved in the bead transport. This issue will be discussed in the following section.

3.4.2.2 Effective molecule number

Binding efficiency of motors to the microtubules. Besides the binding efficiency of the kinesin molecule to loads, another constraining factor needs to be taken into consideration for the correct estimate of the number of molecules involved in load-transport. Due to the different shapes and sizes of loads and both, the structures and dimensions of the microtubules, not all molecules that are attached to a bead functionally cooperate with the microtubule. The scheme in Figure 3.4-9 demonstrates these geometrical limitations. It is drawn approximately in scale with kinesin molecules transporting a 0.1-µm bead (scheme A/B) along a microtubule. For comparison, additionally, the section of a 0.5-µm bead is drawn in scheme B.

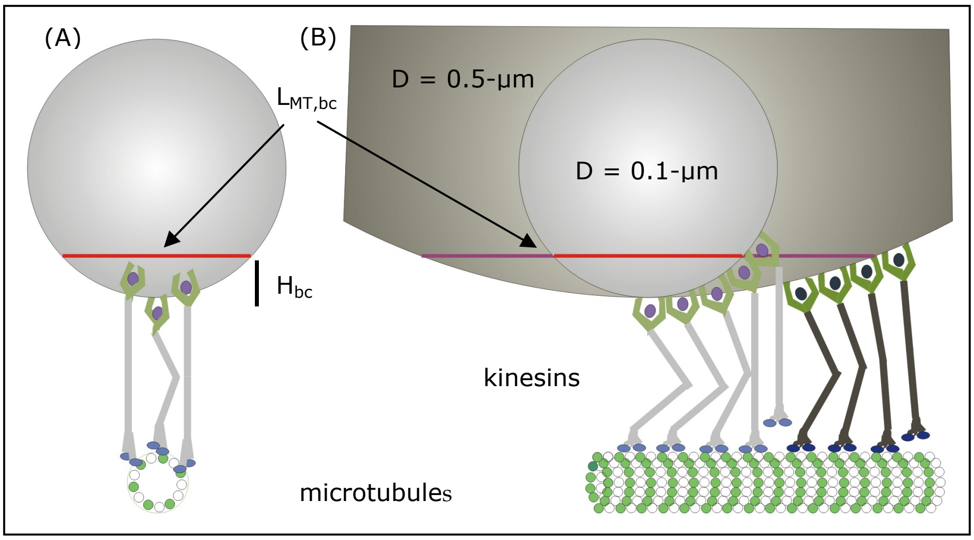

Figure 3.4-9: Schemes of the bead transport along a microtubule with kinesin molecules as carriers. The cartoons show the front view (A) and side view (B) of the bead-kinesin-microtubule complex. The schemes are draw approximately to scale with the real sizes. Each bead has a diameter of 0.1 µm; $L_{MT,bc}$ is the diameter and H_{ac} the height of the bead cap (bc). The second bead (larger half bead) in figure B is five times bigger to demonstrate that at similar molecule flexibility, which is defined by H_{bc}, the radius of the accessible bead cap increases and therefore more molecules can be actively involved in the load transport at once.

The number of motors, actively involved in the bead transport, is mainly limited by the length and flexibility of the kinesin molecule. By molecule flexibility, we consider the ability of the motor to perform movement while being squeezed, stretched or internally bent by a load. This ability must be implied because a load of a certain size and thus curvature is transported. Looking at the lengths of the molecules depicted in scheme B, the outer molecules appear in full length while the molecules in the middle are bent.

This area of the bead, where attached motors are able to bind to the microtubules, is denoted as bead cap (bc) and defined by the height of the cap, H_{bc}, given by the length and flexibility of the molecule and the diameter of the bead.

The flexible region between the rigid coils 1 and 2 allows kinesin bending (kinesin structure, see section 1.3.1). However, if the cargo binding site comes close to the motor domain, movement cannot be performed. It is assumed that the molecule can be bend to at most 16 nm (20 % of the molecule length) while still being able to move. Performing channel height dependent gliding assays an average essential height of 100 nm was measured [Stracke et al. 2000]. Subtracting the value obtained from the total length of the kinesin/microtubule system (80 nm + 25 nm) and a slot allowing for shifts of MTs along the channel walls leaves 5 nm for possible bending of the motor. Thus, for the height of the bead cap with motors involved in the transport, a motor bending of $4\ \text{nm} \leq H_{bc} \leq 16\ \text{nm}$ corresponding to 5 to 20 % is defined. Furthermore, in our experimental design, only beads transported along one microtubule were analyzed. The maximal length of a microtubule fraction which allows kinesin molecules bound to a bead to attach to the filament, $L_{MT,bc}$, is equal to the diameter of the bead cap and is described by:

$$L_{MT,bc} = 2\sqrt{H_{bc}\left(\frac{D}{2} - H_{bc}\right)}\ . \qquad \textbf{Equation 3.4-6}$$

Consequently, the projection of the bead cap on a microtubule track has an area of:

$$A_{MT,bc} = L_{MT,bc}D_{MT}\ , \qquad \textbf{Equation 3.4-7}$$

where D_{MT} is the diameter of the microtubules (D_{MT} = 25 nm), see Figure 3.4-10.

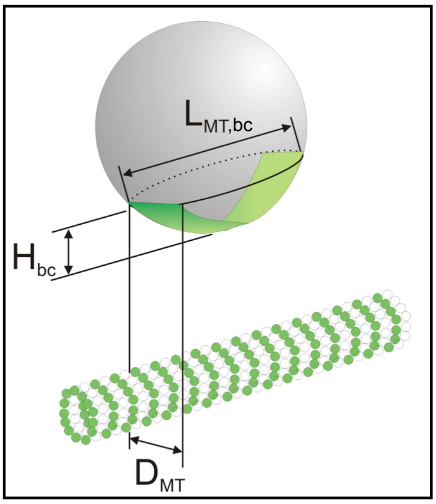

Figure 3.4-10: Sketch of the projection of the microtubule on a 0.1-µm bead (to scale). The molecules that bind to the "activity area" are assumed to be actively involved in the bead transport. The area, $A_{MT,ac}$ is defined by the diameter of the bead cap that depends on molecule flexibility and the diameter of the microtubules.

The number of motors that are bound in this projection area ("activity area"), N_{eff} (bead size dependent), that are actively involved in bead transport, is calculated by:

$$N_{eff} = \frac{A_{MT,bc} N_b}{A_b}, \qquad \textbf{Equation 3.4-8}$$

where N_b is number of adsorbed molecules per bead as determined from the DLS-measurement and A_b is the bead surface area (covered with BSA). This leads to a certain percentage of the total numbers of molecules adsorbed on the beads, which are actually situated in the "activity area". It is between 2.86 – 5.34 % for 0.1-µm beads, 0.33 – 0.59 % for 0.5-µm beads and 0.12 – 0.21 % for 1.0-µm beads for the molecule flexibility assumed. Thus, when a 0.1-µm bead is fully covered with kinesin molecules at maximum 4 to 7 out of all the 130 molecules should be involved in the transport, between 11 and 16 motors, when 0.5-µm beads are observed and 15 to 27 molecules for 1.0-µm beads.

The maximum numbers obtained are now compared to the values estimated from kinesin-tubulin-binding stoichiometries. For instance for a 0.1-µm bead, at an allowed motor bending of 4 nm (5 %) the accessible lengths of the microtubule is 39 nm. According to the binding properties of the kinesin-1 molecule (kinesin preferentially binds to the β-tubulin, see section 1.3), a single molecule requires one tubulin-dimer (8 nm) for binding with one of the motor heads. For movement conditions, the Stoichiometry is even lower. Seitz and Surrey (2006) performed measurements using GFP-labeled *Drosophila* kinesin molecules in the presence of AMP-PNP or ATP. For walking motors (in the presence of ATP) lower fluorescence signals and thus lower binding events were measured as compared to the static bound once (in the presence of AMP-PNP). They consider a maximum kinesin density for active motors of at most one molecule per two tubulin dimers and at least one kinesin dimer per four tubulin dimers (one motor per 16 and 32 nm microtubule respectively), which is half of the density measured for the static situation. However, cooperative movement of kinesin molecules along several protofilaments is likely. The motor domain of kinesin-1 has a size of 4.5 x 4.5 x 7 nm^3 [Kull et al. 1996]. This implies that laterally every second protofilament (4 nm in diameter) could be covered with a motor domain simultaneously. In our experiments the microtubules are immobilized on the glass surface, so that at maximum only at maximum 3 protofilaments are accessible for several motors side by side. From this, it follows, 15 tubulin-dimers are available at the considered track length of 39 nm. Thus, at most 7 and at least 3 molecules could freely move at maximum, which is consistent with the results obtained previously.

Based on the results from the ITC- and DLS-measurements and the assumption that the number of molecules on the bead is limited due to the size of the cargo binding site of the kinesin molecule (full coverage of the bead surface), the initial molecule number in solution was converted to a feasible molecule number on the bead surface. In addition an "activity area" on the bead was defined. Only the fraction of motor that is bound in this area can be actively involved in the bead transport. Combining the results of all three bead sizes, the transport properties were reinterpreted in dependence on effective molecule numbers ranging from 1 to 15 and 1 to 27, see following section.

3.5 *Transport by several motors*

3.5.1 Average motor number - Comparison with the theoretical model

For the smallest bead size observed ($D = 0.1\ \mu m$) we estimate the effective number of kinesin molecules transporting the bead along one microtubule track using two independent methods [Beeg et al. 2006].

One is based on results from DLS-measurements. Different from the analyses explained above, the range of probable number of motors pulling the bead is calculated assuming a linear bead volume change depending on the kinesin concentration. It was shown that within the experimental error (ITC, DLS) the rescaling of the molecule-to-bead ratio can be done in this way for low kinesin concentrations (see section 3.4.2). The same limits were used for molecule bending (4 to 16 nm). The estimated range of the number of motors involved, N_{eff} varies between 1.1 and 4.0 molecules, and is drawn as the shaded region in Figure 3.5-1.

Second, the measured run length distributions of the 0.1-µm beads (see Figure 3.2-2) were analyzed with an extended version of the model for motor cooperation [Klumpp and Lipowsky 2005]. The extension considers a truncated Poisson distribution of the motor number corresponding to experimental conditions. For one motor concentration, many beads are averaged that are most likely transported by different numbers of motors. The run lengths distributions for a bead that is pulled by several motors depends on the single transport parameters: velocity, unbinding and binding rate, kinesin bulk concentration and a parameter c_0, which is defined as the number of active motors per kinesin bulk concentration. The fitting parameters are the binding rate and c_0. The best fit was obtained for motor concentrations up to 6.75 nM (2.5 µg/ml), resulting in a binding rate of $\pi_{ad} = 5.1\ s^{-1}$ and a number of active motors $c_0 = 0.79$. The number of active motors obtained based on the parameter c_0, open squares in Figure 3.5-1 is in the range of numbers obtained from the DLS measurements including geometrical constraints, $0.47 \leq c_0 \leq 1.18$. For the motor bulk concentration analyzed the average motor number, N_{av}, varies between 1.1 and 3.2 motors, with at maximum 2 to 7 motors cooperatively carrying a bead. The estimated binding rate of $5.1\ s^{-1}$, is well in agreement with previous findings ($\pi_{ad} = 4.7\ s^{-1}$) determined for kinesin binding to a membrane tube [Leduc et al. 2004].

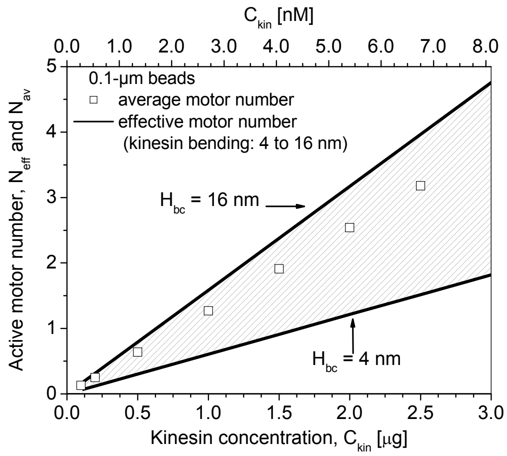

Figure 3.5-1: Number of molecules actively involved in the transport in dependence on the kinesin concentration. Two independent methods were used to determine the number of active molecule involved in bead transport. The one based on the data from the DLS-measurement is plotted as a shaded region limited by the assumption for motor bending. The symbols show the data obtained from fitting the measured run length distributions with the theoretical model. The fitting results lie within the range determined from the DLS-measurements and geometrical constraints.

Using to different methods, the number of active motor carrying the bead could be determined. The active motor number, N_{eff} and N_{av}, are of similar value. The active motor number obtained from fitting the theoretical run length distributions N_{av} corresponds to N_{eff} at allowed motor flexibility of 12 % or 9.6 nm.

3.5.2 Run length, transport velocity and escape force as function of the active motor number

For comparison, previously shown results for the run lengths, transport velocities and escape forces were plotted as a function of the active motor number, N_{eff}. For the smallest beads size (D = 0.1 µm) the numbers, obtained from the theoretical fitting (previously denoted as N_{av}), were used. For the 0.5 and 1.0-µm beads, the number of active motors was deduced from DLS measurements according to geometrical constraints imposed by the projected microtubule area and 12 %-flexibility of the motors.

In Figure 3.5-2A, the average run lengths calculated from exponential decay fits to the probability distributions of run lengths (see sections 3.2.1.1 and 3.2.2.1) and in

Figure 3.5-2B the mean transport velocities (see section 3.2.1.3 and 3.2.2.2) are plotted as a function of the number of active working motors.

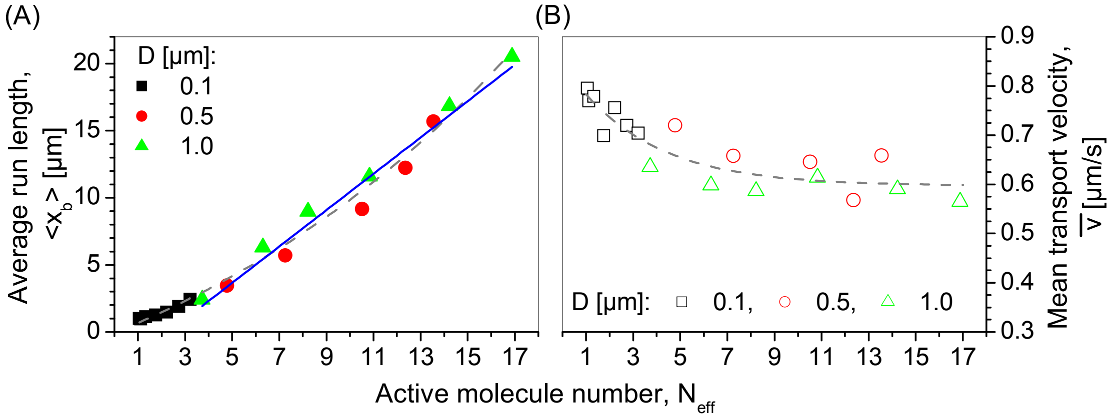

Figure 3.5-2: Average run length and mean velocities as a function of the active number of molecules involved in load transport for different bead sizes. For the 0.1-µm beads the active number, N_{eff} (previously donated as N_{av}), were obtained from fitting the theoretical run length distributions to the experimental histograms. For the bigger beads N_{eff} was determined using DLS-measurement results and geometrical constraints allowing for a motor bending of 12 %. (A) For similar active motor numbers, similar mean run length were determined independent of the bead size. The mean run length increases with the active kinesin number. For the results of the bigger beads a simple approximation is a linear dependence of the run length with an increment of 1.35 µm per molecule (closed blue line). (B) The mean velocities show a slight decrease with increasing the active molecule numbers from about 0.8 µm/s down to 0.6 µm/s. The velocity values show a larger scatter at similar motor numbers for the different bead sizes, as compared to the average run lengths. The dashed grey lines are a guide to the eye.

It is obvious, that the effect of bead size is eliminated and all data sets collapse onto a master curve (dashed grey lines in Figure 3.5-2A/B). The average run length increases with the number of active motors, while single-molecule transport was observed only with the 0.1-µm beads. In the single-molecule transport, an average run length of 1 µm and a mean velocity of about 0.8 µm/s are measured, which is in agreement with previous findings [Howard et al. 1989, Block et al. 1990, Coy et al. 1999]. Because of the limited optical resolution it was difficult to distinguish runs shorter than 0.75 µm from single binding events. Thus, single-molecule transport could not be detected for the bigger beads. Assuming an approximately linear increase of the mean run lengths with the active number from more than 3 cooperating molecules, an increment $\Delta x_b/N_{eff}$ of 1.35 µm per kinesin molecule is derived (see closed blue line in Figure 3.5-2A).

The measured mean velocities are showing a larger scatter at similar active motor numbers. The general trend observed is a decrease from 0.8 to 0.6 µm/s for higher molecule numbers. As discussed before (section 3.2.1.4), this is presumably due to inhibition of adjacent binding sites occupied by free kinesins. The tubulin dimer is either blocked by a bead-free kinesin motor or another motor walking in front that is also cooperating in the bead transport. Waiting for the motor-bead unbinding which creates a free binding place for the next motor walking behind, slows the transport down. Furthermore changing microtubules during the transport process (in the walking direction), because of the limited length of a microtubules can decrease the velocity. It could explain the higher mean velocities for the smaller beads where long runs were rarely. This is an interesting subject for further studies.

Besides the decrease in motility a decrease in the average run length and binding rate was observed for the smallest bead size at highest kinesin concentrations. The latter suggests an overload: there are too many free kinesin molecules in solution at high motor concentrations in solution that interfere with the bead motility, see therefore section 3.2.1.4. Most likely this occurs, as confirmed by the DLS measurements, which show a saturation of the effective bead diameter (section 3.4.1.2).

Plotting the measured escape forces against the active number of motors pulling the bead, see Figure 3.5-3, a similar trend as for the run length results is found. In the molecule range observed, comparable escape force values were determined for same motor numbers, independent of the diameters of the kinesin-carrying beads. Minor variations, e.g., for small motor numbers, are due to the specific force distributions. Whereas the force distributions for the smaller beads (D = 0.5 µm) are unimodal, multimodal force distributions were observed for the larger ones. According to the curve progression, a linear dependence of the mean escape force on the number of active molecule can be assumed and suggesting an increase of 0.622 pN every additional kinesin molecule, $\Delta F_{esc}/N_{eff}$ is determined. Note that analyzes of the force values in dependence on the binding probability ($p_{b > 1}$) of kinesin-coated beads resulted in lower numbers (see section 3.3.2.2). For an escape force of about 0.6 pN single-molecule transport was assumed, N_{eff} is ranged between 3 and 5 molecules. For assumed two-molecule transport (F_{esc} = 2.7 pN), N_{eff} varies from 6 to 10 molecules.

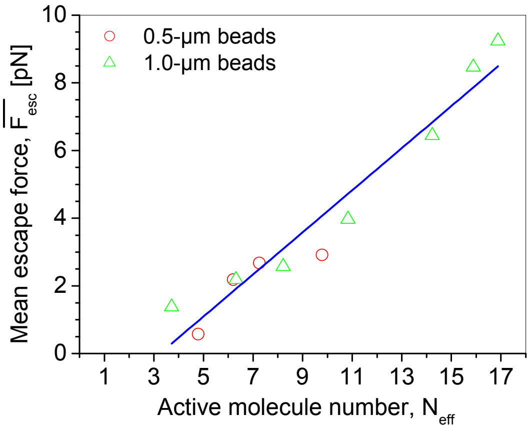

Figure 3.5-3: Mean escape force as a function of the effective molecule number. Independent of the bead size, an increase of the mean escape forces is observed for higher numbers of molecules actively involved in transporting the bead. The blue line is a linear fit (see text for details).

We measured relatively small escape forces. More than 10 motors are actively pulling the bead out of the trap at escape forces comparable to the stall force measured for a single motor. The stall force is the force needed to stop a walking motor. The escape force is the optical trap force at which the motors can pull the bead out of the trap. The latter is measured throughout this work, and obtained by first trapping the bead, i.e., stopping the motor and then reducing the trapping force until the motor is released and walks away. The escape of beads was optically detected. Compared to the fast motility of molecular motors, the laser power is reduced slowly. Thus, the force measured is not representing the initial/starting condition (active number). It is more likely that some motors already detached from the microtubules, which would result in lower force values. According to this, the active numbers obtained from the comparison of the escape forces to the binding probabilities p_b are preferred.

To calibrate the force, separate measurements with free beads (not coated with motors) were performed. The beads were trapped in solution and the escape velocity at fixed trap power (i.e., trap force) was determined. The escape velocity in this case was set by the microscope stage. Note that these velocities (> 0.1 mm/s) are much higher than the average transport velocity of kinesin-coated beads (0.6 – 0.8 µm/s). Thus, the force calibration was performed at a different velocity range. Unfortunately, we could not perform the force calibration for lower escape velocities due to the limits imposed by the motorized stage of the microscope. However, the calibration experiments were performed carefully (see section 3.3.1) to derive the effective force that a bead experiences close to the chamber wall, where the force is mainly influenced by hydrodynamic friction in this limit

In conclusion, transport parameters of kinesin-driven beads were determined in dependence of the active number of molecule. At small kinesin concentrations, single molecule transport was observed showing a typical run length of 1 µm. Several kinesin molecules have to cooperatively transport a bead for larger run lengths or forces to be observed. This is supported by the experimental results obtained *in vitro*. At maximum an average run length of about 20 µm was measured, a transport distance which is rather common *in vivo*, where cargo transport in axons usually spans tens of micrometers or even up to one meter [Goldstein and Yang 2000]. Single-molecule transport could be characterized by alternating directed movement with Brownian motion according to defined molecule processivity and unbinding rates of the molecule, which strongly reduces the transport velocity [Lipowsky et al. 2001, Nieuwenhuizen et al. 2002]. Beside the realization of fast cargo transport over long distances, cooperative transport of several molecules is more easily accessible to regulatory mechanisms. By activating/deactivating cargo-bound motors or regulating cargo surface coverage with motors, the transport parameters can be finely tuned in contrast to having only an on/off state for a single molecule. Furthermore, the understanding of such processes is an interesting step towards the invention of biotechnological devices, like biomimetic sorting systems [Unger et al. 2004] in the micrometer range that involves molecular motors as transporters.

Chapter 4

Conclusion and Outlook

The aim of this work was to study the transport properties of cooperating biomotor molecules. The protein used was kinesin-1 *in vitro*. We have investigated the influence of the number of motor molecules cooperatively carrying a load in dependence on the transport parameters run length, binding rate or binding probability, velocity and force generation.

The experiments were performed in an experimental chamber of isoplolar aligned microtubules that were immobilized on the microscopic glass surface. This approach allows studying transport along non-crossing microtubules and distances exceeding the length of a single microtubule. The latter is expected when several motors are involved in the load transport. Polystyrene beads of various sizes, which were incubated in kinesin solutions of various concentrations, were used as load material during which the bead concentration was kept constant to achieve different motor molecule densities on the bead surface. Throughout the experiments, the smallest beads (0.1-µm in diameter) were left to spontaneously bind to the microtubules, whereas for the beads with larger sizes (D = 0.5, 1.0 and 2.0 µm) the binding was mediated by the use of optical tweezers. The results obtained were found to be independent of the experimental procedure used.

First, we have studied various transport characteristics and their dependence on the kinesin concentration:

(i) run lengths,

(ii) binding events of kinesin-coated beads to the microtubule track (binding rate and binding probability), and
(iii) transport velocities.

(i) The experiments covered kinesin-to-bead ratios that correspond to one transporting molecule. This was confirmed by the average run length-results of the smallest bead size observed at the lowest kinesin concentration. In these experiments, the change in the average run lengths due to different kinesin concentrations was comparatively small (section 3.2.1.1). Bigger beads that were incubated at similar kinesin concentrations (same kinesin surface densities on the beads) were transported over longer distances, implying many-motor transport (section 3.2.2.1). Even though the motor density is kept constant, the projected area of a microtubule on the bigger beads is larger and therefore more motors should be able to bind to the track and longer runs should be observed.

(ii) The parameter binding rate is defined by the number of beads binding per µm microtubules per minute (section 3.2.1.2), where the binding probability is designed as the fraction of beads binding to the microtubules when the bead is trapped with an optical tweezers and brought close to the track. In both cases, more binding events were observed with increasing kinesin concentrations. The binding probability as a criterion to estimate the number of motors involved in the transport is applicable only in the low and intermediate motor concentration range, because at a high motor density almost all beads bind to the microtubules and exhibit movement (section 3.3.2.2).

(iii) The average velocity was measured to be independent of the kinesin surface concentration for the bigger beads (D = 0.5, 1.0 and 2.0 µm), see section 3.2.2.2. For low kinesin concentrations, similar behavior was found for the transport velocity of the smallest bead size (D = 0.1 µm) observed (section 3.2.1.3). However, for the smallest beads the average velocity is slightly larger than the velocities measured for the bigger beads. All values determined lie within the velocity range measured by other groups.

An exception was observed for 0.1-µm beads at the highest motor concentration. For all three parameters determined different trends were obtained. On average, shorter runs, fewer binding events and a slow down in the transport velocity were observed. This could be explained by an excessive coverage and thus presence of free motors in solution which, presumably, interact with the microtubule as well. That causes an overload and potential jamming along the tracks, see section 3.2.1.4.

Second, we investigated the force generation using optical tweezers in dependence on the motor number. Based on Stokes' law the escape force was determined, the force at which a kinesin-coated bead leaves the optical tweezers and moves away (section 3.3.1). With increasing motor concentrations higher escape forces were measured (section 3.3.2.1). In the lower motor concentration range, where the binding probability was an efficient criterion, overall force distributions for different bead size resulted in two main force peaks at about 0.6 and 2.7 pN. These two escape force values can be related to 1 and 2 molecule transport respectively (section 3.3.2.2). The values obtained for the escape force are below the known stall force for a single kinesin molecule ($F_s \sim 6$ pN). The trend of forces increasing with the number of molecules transporting the bead is quite pronounced.

In our experimental design, the kinesin molecules bind unspecifically but tightly to the bead surface. To characterize the active motor number for every kinesin concentration we used two additional techniques:

(i) Isothermal titration calorimetry (ITC), and
(ii) Dynamic light scattering (DLS).

(i) With ITC-measurements, the binding heat of kinesin molecules released while attaching to the bead surface was determined (section 3.4.1.1). Limited by the high motor concentration needed to get a strong signal, only similar binding heats in the covered motor concentration range were determined at kinesin densities up to 289 molecules/bead. Saturation and thus full coverage of the beads, however, could not be observed needed to extract information about the equilibrium constant characterizing the binding process.

(ii) DLS was used to measure the change in the bead hydrodynamic diameter due to kinesin molecules attached as compared to that as a free bead (section 3.4.1.2). We observed increasing size changes with increasing motor concentrations. The resulting effective volume change depends on the kinesin bulk concentration. For the smallest bead size observed, we determined a linear dependence on the effective volume change for the low motor concentration range. The Langmuir adsorption model was used to fit the data measured for the bigger beads. We further assumed that the resulting bead volume change is proportional to the average number of bound motors. At saturation, the bead is fully covered and the maximum number of occupation sites on the bead surface can be estimated by considering a well defined surface area covered by a single kinesin molecule. At lower concentrations the number of motors can then be estimated from the concentration dependence of the beads volume change.

The cumulative binding heat and the change in the bead volume due to the binding of motor proteins on the bead surface are proportional to each other. This allows the extrapolation of the cumulative binding heat to obtain the value at full coverage of the bead surface with kinesin molecules (N_{max} = 130 molecules/bead). From this assumption a binding heat of about 50 kJ/mol or 19 k_BT per kinesin molecule is derived, see section 3.4.2.1.

The beads are big compared to the size of kinesin (L_{kin} = 80 nm). Thus, only a small fraction of all the molecules bound to the bead surface are potentially able to bind to the microtubule as well. To calculate this fraction, several constrains were taken into account:

- allowed bending (flexibility) of the motor protein,
- size and structure of the track, where the movement along only one microtubule was analyzed, and
- curvature of the bead surface.

Implementing these geometrical constrains into the analysis of the results obtained from the DLS-measurements gives an effective motor number, i.e., the number of motors pulling the load. It is found, that in the concentration range studied, between 1 and 7 motors are involved in the transport of 0.1-µm beads (section 3.4.2.2). In addition, a second method was used to estimate the average number of active motors. The increase in the run lengths was analyzed in a quantitative fashion by comparing the measured run length distributions for the smallest bead size with a theoretical model. This model is adapted to the experimental conditions allowing for several motor numbers transporting the beads for a defined motor concentration. The average number of active motors obtained is in agreement with the effective motor numbers (section 3.5.1).

Motivated by these findings, the average run length results, transport velocities and mean escape forces were again analyzed in dependence on the active motor numbers then determined (section 3.5.2). It is shown, that the effect of bead size is eliminated. All run length- and escape force-data collapse onto master curves, where the average run length increases with the number of active motors by about 1.35 µm per active motor in the molecule range observed, and an increase of the escape force of about 0.622 pN was estimated. For small motor numbers, that are actively transporting a bead, the transport velocity is of the same value of approximately 0.8 µm/s. With increasing number of active motors the motion decelerates down to 0.6 µm/s.

In summary, it is shown in a quantitative fashion that the run length and the escape force increase with the number of motors involved in the bead transport and shown to exceed the known values for a single kinesin-1 transport.

An interesting challenge for future experiments is the development of a transport system where one can directly control the number of active motors and thus the transport parameters. A first step to this approach would be the preparation of the load material to allow motor binding on a restricted part of the surface area. New results show that it is possible to pattern surfaces with nanodots in a controlled fashion, for instance equally spaced nanodots of a controlled surface concentration [Glass et al. 2004, Gorzolnik et al. 2006]. The nanodots can be modified in a way that each of them binds a single motor molecule. Using such patterned particles with well-defined motor coverage would provide an alternative way to control the number of motors involved in the bead transport. However, even in this case one has to consider the geometrical constraints on the fraction of motors, which can be directly in contact with a long and narrow microtubule, and thus be involved in the bead displacement.

An alternative approach may present the possibility of using chemically bound motor assemblies, i.e., groups of 2, 3 or more motors attached to protein scaffolds [Diehl et al. 2006]. Attaching these assemblies to latex beads in the limit of very dilute incubation concentrations (e.g. corresponding to attaching one assembly to a single bead), would provide a load with an exact number of motors pulling.

Appendix

Abbreviations

ADP	Adenosine-5'-(trihydrogen diphosphate)
AMP-PNP	Non-hydrolysable ATP analogon
ATP	Adenosine-5'-triphosphate
bc	Bead cap
BCIP/NBT	5-Bromo-4-chloro-3-indolyl phosphate/Nitro blue tetrazolium
BSA	Bovine serum albumin
CCD	Charge-coupled device
CD	Cargo domain of the kinesin motor
conc.	Concentration
cryo-EM	Cryo-electron microscopy
CS	Color solution
Dr	Direction of movement
ddH_20	double distilled water
DEAE-cellulose	Diethylaminoethyl cellulose
DLS	Dynamic light scattering
DMSO	Dimethylsulfoxid
DNA/RNA	Desoxy-ribose nucleic acid/ Ribonucleic acid
DTT	Dithiothreitol
EDTA	Ethylenediaminetetraacetic acid
EGTA	Ethylene glycol tetraacetic acid
EPR	Electron paramagnetic resonance
ER	endoplasmatic reticulum
FA/SA	First-/Second antibody
FIONA	Fluorescence imaging with one-nanometer accuracy
FPLC	Fast protein liquid chromatography
FRET	Fluorescence resonance energy transfer
G-, F-actin	Globular-, Filamentous-actin
GDP	Guanosin-5'-diphosphate
GTP	Guanosin-5'-triphosphate
IF(P)	Intermediate filament (protein)
ITC	Isothermal titration calorimetry

KHC	Kinesin heavy chain
KLC	Kinesin light chain
MAP(s)	Microtubule-associated protein(s)
MD	Motor domain
MgATP	Equimolar magnesium ions and adenosine triphosphate
MT	Microtubule
MTOC	Microtubule-organizing centre
N-/C-terminal	Amine-/carboxyl terminal end, extremity of the amino acid chain of a protein or peptide
N.A.	Numerical aperture
Nd:YAG laser	neodymium-doped yttrium aluminum garnet
PA	Primary antibody
PBS	Phosphate-buffered saline
PC-tubulin	Phosphocellulose purified tubulin
Pe	Pefabloc
Pi	Phosphatase
Pr	Processivity
SA	Secondary antibody
SD	Standard deviation
SDS-PAGE	Sodium dodecyl sulphate-Polyacrylamide gel electrophoresis
SP	Streptavidin-biotinylated alkaline phosphatase
TEM	Transmission electron microscopy
TRIS	Trishydroxymethylaminomethane
TWEEN	Polysorbate
VE	Video enhanced
VE-DIC	Video enhanced-differential interference contrast
VE-Ph	Video enhanced-phase contrast

List of symbols

a	n/N for beads running less than 1 µm
A_0	Zero absorbance
$A_{360\ nm}$	Absorbance at 360 nm
ΔA	Absorbance value after 30 min of microtubule assembly at 37° C
A_b	Bead surface area
A_{mol}	Area the kinesin molecule requires for binding
$A_{MT,bc}$	Projection of the bead cap on a microtubule track
c^a	Motor density per µm^{-2} surface area, assuming that all beads in solution bind to the surface area
c^b	Kinesin-to-bead ratio, assuming that all beads in solution bind to the bead
C_{ATP}	ATP concentration
C_{kin}	Total kinesin concentration in the working solution
C_{crit}	Lowest tubulin concentration at which polymerization is measurable
c_0	Number of active motors per kinesin bulk concentration
D	Bead diameter
D_{CD}	Diameter of the cargo domain
D_{MT}	Diameter of the microtubules
f_{corr}	Extrapolation correction factor for calibrated escape forces, at 2h/D > 5, to the distance of measurement
F_{esc}	Stokes' escape force
$<F_{esc}>$	Average escape force derived from Gaussian fits to the force distributions
$\overline{F}_{esc}$	Mean escape force
$\Delta F_{esc}/N_{eff}$	Increase of the escape force per active motor
F_s	Stall force
h	Space between the cover slip and the bead surface
H_b	Difference of the binding heat
$H_{b,cum}$	Cumulative binding heat
H_{bc}	Height of the bead cap which is equal to the flexibility of the motor
I	Current
k	Hydrodynamic correction for the coupling of the particle with the wall
$K_{1/2}$	Molecule-to-bead ratio at which half of the maximum change of the volume is measured

K_D	Dissociation constant which characterizes the binding of free kinesin to β-tubulin
K_m	Dissociation constant, value for the activation of the kinesin ATPase by microtubules
k_bT	Thermal energy (k_b-Boltzmann constant)
L_{kin}	Length of the kinesin-1 molecule
L_{lat}	Lateral extension of the cargo binding site composed of two kinesin light chains and the cargo domain
$L_{MT,bc}$	Maximal length of a microtubule fraction which is within reach for kinesin molecules attached on one bead
M_{KHC}	Molecular weight of the kinesin heavy chain (monomer)
M_{kin}	Molecular weight of the tetrameric kinesin-1 molecule
M_{KLC}	Molecular weight of the kinesin light chain (monomer)
n	Number of binding and/or moving beads per bin or observed motor concentration
n_{oil}, n_m	refractive index of the immersion oil respectively the buffer solution (medium)
n/N	Bead fraction
N	Total number of transported or observed beads
N_{av}	Average actively transporting motor number obtained from the theoretical fit to the run length distribution
N_b	Number of adsorbed molecules per bead as determined from the DLS-measurement
N_{max}	Maximum number of molecules that can bind to the bead surface
N_{eff}	Number of motors that are bound to the bead and in contact with the microtubule
P	Power
p_b	Binding probability, corresponds to the Poisson probability that one or more molecules are transporting the bead
r_b	Binding rate defined by the number of beads binding to a microtubule per µm microtubule and per minute
R_h	Hydrodynamic radius
$\langle R_0 \rangle$	Average hydrodynamic radius of beads in a kinesin-free bead solution
$\langle R_{ch} \rangle$	Average hydrodynamic radius of beads covered with kinesin molecules
ΔR_h	Change in the bead radius due to bound motors
$\Delta R_{h,max}$	Maximum change in the hydrodynamic radius
v_{esc}	Velocity at which the bead escaped from the optical trap
$v_{esc,max}$	Maximum escape velocity at a distance from the glass surface of 2h/D > 5 (no wall effect)
v_g	Gliding velocity
$v_{g/max}$	Maximum gliding velocity
$\bar{\mathbf{v}}$	Mean velocity of active motors
$\langle v \rangle$	Average velocity of a defined bead size, independent of the motor concentration
v_C	velocity of beads depending on the kinesin bulk concentration in solution
$\bar{v}_C$	Mean velocity of beads depending on the kinesin bulk concentration in solution
$\langle v_C \rangle$	Average velocity of beads depending on the kinesin bulk concentration in solution (rmotor density on the bead surface)

V_0	Volume of the uncovered bead
V_h	Volume obtained from the measured hydrodynamic radius
V_{max}	Maximum change of the volume at molecule saturation on the bead surface
ΔV	Volume change
x_b	Run length of a kinesin-coated bead
$\overline{x}_b$	Mean run length kinesin-coated beads
$<x_b>$	Average run length kinesin-coated beads
$\Delta x_b/N_{eff}$	Increase of the run length per active motor
λ	Fitting parameter of the Binding probability function
π_{ad}	Binding rate of kinesin molecules to the microtubules
η	Dynamic viscosity of the buffer solution
1-prob.dist.	1-probability distributions of induvidual run lengths

List of figures and tables

Bibliography

Alberts B, Bray D, Lewis J, Raff M, Roberts K, and Watson JD. Molecular biology of the cell. Garland Publishing, Inc., New York, 2002 (4rd ed.).

Allen RD, Allen NS, and Travis JL. Video-enhanced contrast, differential interference contrast (AVEC-DIC) microscopy: a new method capable of analyzing microtubule-related motility in the reticulopodial network of *Allogromia*. *Cell Motil.* 1:291–302 (1981).

Allen RD. New observations on cell architecture and dynamics by video-enhanced contrast optical microscopy. *Annu. Rev. Biophys. Chem.* 14:265–290 (1985).

Amos LA. Kinesin from pig brain studied by electron microscopy. *J. Cell Sci.* 87:105-111 (1987).

Andrews P. Estimation of molecular size and molecular weights of biological compounds by gel filtration. *Methods Biochem. Anal.* 18:1– 53 (1970).

Asbury CL, Fehr AN, and Block SM. Kinesin moves by an asymmetric handoverhand mechanism. *Science* 302:2130–2134 (2003).

Ashkin A. Acceleration and trapping of particles by radiation pressure. *Phys. Rev. Lett.* 24:156-159 (1970).

Ashkin A, Dziedzic JM, Bjorkholm JE, Chu S. Observation of a single-beam gradient force optical trap for dielectric particles. *Opt. Lett.* 11:288-290 (1986).

Ashkin A. Optical trapping and manipulation of neutral particles using lasers. *Proc. Natl. Acad. Sci. USA* 94:4853-4860 (1997).

Ashkin A, Schutze K, Dziedzic JM, Euteneuer U, and Schliwa M. Force generation of organelle transport measured in vivo by an infrared laser trap. *Nature* 348:346-348 (1990).

Beeg J, Klumpp S, Dimova R, Serral Gracià R, Unger E, and Lipowsky R. Transport of beads by several kinesin motors. *Biophys. J.*, in press

Block SM, Asbury CL, Shaevitz JW, and Lang MJ. Probing the kinesin reaction cycle with a 2D optical force clamp. *Proc. Natl. Acad. Sci. USA* 100:2351-2356 (2003).

Block SM, Goldstein LS, and Schnapp BJ. Bead movement by single kinesin molecules studied with optical tweezers. *Nature* 348:348-352 (1990).

Bloom GS, Wagner MC, Pfister KK, and Brady ST. Native structure and physical properties of bovine brain kinesin and identification of the ATP-binding subunit polypeptide. *Biochem.* 27:3409-3416 (1988).

Boehm KJ, Stracke R, Baum M, Zieren M, and Unger E. Effect of temperature on kinesin-driven microtubule gliding and kinesin ATPase activity. *FEBS Letters* 466:59-62 (2000).

Boehm KJ, Stracke R, Mühlig P, and Unger E. Motor protein-driven unidirectional transport of micrometer-sized cargoes across isopolar microtubule arrays. *Nanotechnol.* 12:238-244 (2001).

Boehm KJ, Beeg J, Meyer zur Hörste G, Stracke R and Unger E. Kinesin-driven sorting machine on large-scale microtubule array. *IEEE Transaction on Advanced Packaging* 28:571-576 (2005).

Brady ST. A novel brain ATPase with properties expected for the fast axonal transport motor. *Nature* 317:73-75 (1985).

Bray D, and Bunge MB. Serial analysis of microtubules in cultured rat sensory axons. *J. Neurocytol.* 10:589–605 (1981).

Burton PR. Microtubules of frog olfactory axons: their length and number/axon. *Brain Res.* 409:71-78 (1987).

Case RB, Pierce DW, Hom BN, Hart CL, Vale RD. The directional preference of kinesin motors is specified by an element outside of the motor catalytic domain. *Cell* 90:959–966 (1997).

Coy DL, Wagenbach M, and Howard J. Kinesin takes one 8nm step for each ATP that it hydrolyzes. *J. Biol. Chem.* 274:3667–33671 (1999).

Diaz JF, and Andreu JM. Assembly of purified GDP-tubulin into microtubules induced by taxol and taxotere: reversibility, ligand stoichiometry, and competition. *Biochemistry* 32: 2747-55 (1993).

Diehl MR, Zhang K, Lee HJ, and Tirrell DA. Engineering cooperativity in biomotor-protein assemblies. Science 311:1468-1471 (2006).

Fan J, Griffiths AD, Lockhart A, Cross RA, and Amos LA. Microtubule minus ends can be labeled with a phage displayed antibody specific to alpha-tubulin. *J. Mol. Biol.* 259:325-330 (1996).

Gittes F, Meyhofer E, Baek S, and Howard J.Directional loading of the kinesin motor molecule as it buckles a microtubule. *Biophys. J.* 70:418-429 (1996).

Glass G, Arnold M, Cavalcanti-Adam EA, Blümmel J, Haferkemper C, Dodd C, and Spatz JP. Block copolymer micelle nanolithography on non-conductive substrates. *New J. Phys.* 6 101 (2004).

Goldstein LS, and Yang Z. Microtubule-based transport systems in neurons: the roles of kinesins and dyneins. *Annu. Rev. Neurosci.* 23:39-71 (2000).

Gorzolnik B, Mela P, and Moeller M. Nano-structured micropatterns by combination of block copolymer self-assembly and UV photolithography. *Nanotechnol.* 17:5027-5032 (2006).

Gross SP, Welte MA, Block SM, and Wieschaus EF. Coordination of oppositepolarity microtubule motors. J. Cell Biol. 156:715–724 (2002).

Grummt M, Woehlke G, Henningsen U, Fuchs S, Schleicher M, and Schliwa M. Importance of a flexible hinge near the motor domain in kinesin-driven motility. *EMBO* 19:5536-5542 (1998).

Hackney DD, Levitt JD and Suhan J. Kinesin undergoes a 9S to 6S conformational transition. *J. Biol. Chem.* 267:8696-8701 (1992).

Happel J, and Brenner H. Low Reynolds Number Hydrodynamics. Kluwer Academic Publishers, Dordrecht, The Netherlands (1991).

Heald R, Tournebize R, Blank T, Sandaltzopoulos R, Becker P, Hyman A, and Karsenti E. Self-organization of microtubules into bipolar spindles around artificial chromosomes in Xenopus egg extracts. *Nature* 382:420-425 (1996).

Heidemann SR, Landeers JM, and Hamborg MA. Polarity orientation of axonal microtubules. *J. Cell Biol.* 91:661-665 (1981).

Hill DB, Plaza MJ, Bonin K, and Holzwarth G. Fast vesicle transport in PC12 neurites: velocities and forces. *Eur. Biophys. J.* 33:623–632 (2004).

Hirokawa N, Pfister KK, Yorifuri H, Wagner MC, Brady ST, and Bloom GS. Submolecular domains of bovine brain kinesin identified by electron microscopy and monoclonal antibody decoration. *Cell* 56:867-878 (1989).

Hirokawa N. Microtubule organization and dynamics dependent on microtubule-associated proteins. *Curr. Opin. Cell Biol.* 6:74-81 (1994).

Hirokawa N. Organelle transport along microtubules - the role of KIFs. *Trends Cell Biol*. 6:135-141 (1996).

Howard J, Hudspeth AJ, and Vale RD. Movement of microtubules by single kinesin molecules. *Nature* 342:154-158 (1989).

Howard J. Mechanics of the motor proteins and the cytoskeleton. Sinauer Associates, Inc., Sunderland, 2001.

Hua W, Young EC, Fleming ML, and Gelles J. Coupling of kinesin steps to ATP hydrolysis. *Nature* 388:390–393 (1997).

Hunt AJ, Gittes F, and Howard J. The force exerted by a single kinesin molecule against a viscous load. *Biophys. .J.* 67:766-781 (1994).

ImageJ. public domain software: http://rsb.info.nih.gov/ij

Inoué S. Video Microscopy. 1986, New York: Plenum Press.

Kawaguchi K, and Ishiwata S. Temperature dependence of force, velocity, and processivity of single kinesin molecules. *Biochem. Biophys. Res. Commun.* 272:895-899 (2000).

King SJ, and Schroer TA. Dynactin increases the processivity of the cytoplasmatic dynein motor. *Nature Cell Biol.* 2:20-24 (2000).

Klumpp S, and Lipowsky R. Cooperative cargo transport by several molecular motors. *Proc. Natl. Acad. Sci.* U S A 102: 17284-17289 (2005).

Klumpp S, Nieuwenhuizen TM, Lipowsky R. Self-organized density patterns of molecular motors in arrays of cytoskeletal filaments. *Biophys. J.* 88:3118-3132 (2005).

Kojima H, Muto E, Higuchi H, and Yanagida T. Mechanics of single kinesin molecules measured by optical trapping nanometry. *Biophys.J* 73:2012-2022 (1997).

Kozielski F, Sack S, Marx A, Thormählen M, Schönbrunn E, Biou V, Thompson A, Mandelkow EM, and Mandelkow E. The crystal structure of dimeric kinesin and implications for microtubule-dependent motility. *Cell* 91:985-994 (1997).

Kraikivski P, Pouligny P, and Dimova R. Implementing both short- and long-working-distance optical trapping into a commercial microscope. *Rev. Sci. Instrum.* 77:113703 (2006).

Kreis T, and Vale R (editors). Guidebook to the cytoskeletal and motor proteins. Sambrook and Tooze Publishing Partnership, New York, 1999 (2nd ed.).

Kull FJ, Sablin EP, Lau R, Fletterick RJ, and Vale RD. Crystal structure of the kinesin motor domain reveals a structural similarity to myosin. *Nature* 380:550-555 (1996).

Kural C, Kim H, Syed S, Goshima G, Gelfand VI, and Selvin PR. Kinesin and dynein move a peroxisome *in vivo*: A tug-of-war or coordinated movement? *Science* 308:1469–1472 (2005).

Kuznetsov SA, Gelfand VI. Bovine brain kinesin is a microtubule-activated ATPase. *Proc. Natl. Acad. Sci. U S A* 83:8530-8534 (1986).

Laemmli UK. Cleavage of structural proteins during the assembly of the head of bacteriophage T4. *Nature* 227:680-685 (1970).

Lawrence CJ et al. A standardized kinesin nomenclature. *J. Cell Biol.* 167:19-22 (2004).

Leduc C, Campàs O, Zeldovich KB, Roux A, Jolimaitre P, Bourel-Bonnet L, Goud B, Joanny J-F, Bassereau P, and Prost J. Cooperative extraction of membrane nanotubes by molecular motors. *Proc. Natl. Acad. Sci. USA* 101:17096–17101 (2004).

Levi V, Serpinskaya AS, Gratton E, and Gelfand V. Organelle transport along microtubules in *Xenopus melanophores*: Evidence for cooperation between multiple motors. *Biophys. J.* 90:318–327 (2006).

Lipowsky R, Klumpp S, and Nieuwenhuizen TM. Random walks of cytoskeletal motors in open and closed compartments. *Phys. Rev. Lett.* 87:108101 (2001).

Lowry OH, Rosebrough NJ, Farr AL, and Randall RJ. Protein measurement with the Folin phenol reagent. *J Biol. Chem.* 193:265-275 (1951).

Luby-Phelbs K. Cytoarchitecture and physical properties of cytoplasm: volume, viscosity, diffusion, intracellular surface area. *Int. Rev. Cytol.- Survey Cell Biol.* 192:189-221 (2000).

Mandelkow E, and Mandelkow EM. Kinesin motors and disease. *Trends Cell Biol.* 12:585-591 (2002).

Meyhofer E, and Howard J. The force generated by a single kinesin molecule against an elastic load. *Proc. Natl. Acad. Sci.* U S A 92:574-578 (1995).

Miller RH, and Lasek RJ. Crossbridges Mediate Anterograde and Retrograde Vesicle Transport along Microtubules in Squid Axoplasm. *J. Cell Biol.* 101:2181–2193 (1985).

Mitchison T, and Kirschner M. Dynamic instability of microtubule growth. *Nature* 312:237-242 (1984).

Morejohn LC, and Fosket DE. Taxol-induced rose microtubule polymerization in vitro and its inhibition by colchicine. *J. Cell Biol.* 99:141-147 (1984).

Mueller-Reichert T, Chrétien D, Severin F, and Hyman AA. Structural changes at microtubule ends accompanying GTP hydrolysis: information from a slowly hydrolyzable analogue of GTP, guanylyl (α,β) methylenediphosphonate. *Proc. Natl. Acad. Sci. USA* 95:3661-3666 (1998).
Nieuwenhuizen TM, Klumpp S, and Lipowsky R. Walks of molecular motors in two and three dimensions. Europhys. Lett. 58:468-474 (2002).

Okada Y, and Hirokawa N. A processive single-headed motor: kinesin superfamily protein KIF 1A. *Science* 283:1152-1157 (1999a).

Okada Y, and Hirokawa N. Mechanism of the single-headed processivity: Diffusional anchoring between the k-loop of kinesin and the C terminus of tubulin. *Proc. Natl. Acad. Sci. USA* 97:640-645 (1999b).

Pierce MM, Raman CS, and Nall BT. Isothermal titration calorimetry of protein-protein interactions. *Methods* 19:213-221 (1999).

Pizon V, Iakovenko A, Van Der Ven PF, Kelly R, Fatu C, Furst DO, Karsenti E, and Gautel M. *J Cell Sci.* 115:4469-82 (2002).

Rice S, Lin AW, Safer D, Hart CL, Naber N, Carragher BO, Cain SM, Pechatnikova E, Wilson-Kubelek EM, Whitaker M, Pate E, Cooke R, Taylor EW, Milligan RA, and Vale RD. A structural change in the kinesin motor protein that drives motility. *Nature* 402:778-783 (1999).

Rohrbach A, and Stelzer EHK. Trapping forces, force constants, and potential depths for dielectric sheres in the presence of spherical abberations. *Applied Physics* 41:2494-2507 (2002).

Romberg L, Pierce DW, Vale RD. Role of the kinesin neck region in processive microtubule-based motility. J Cell Biol. 140:1407–1416 (1998).

Schiff PB, Fant J, and Horwitz SB. Promotion of microtubule assembly in vitro by taxol. *Nature* 277:665-667 (1979).

Schliwa M (ed.). Molecular motors. WileyVCH, Weinheim, 2003.

Schliwa M and Woehlke G. Molecular motors. *Nature* 422:759-765 (2003).

Schnapp BJ, Vale RD, Sheetz MP, and Reese TS. Single microtubules from squid axoplasm support bidirectional movement of organelles. *Cell* 40:455-62 (1985).

Schnapp BJ, Reese TS, and bechtold R. Kinesin is bound with affinity to squid axon organelles that move to the plus-end of microtubules. *J. Cell Biol.* 119:389-399 (1992).

Schnitzer MJ, and Block SM. Kinesin hydrolyses one ATP per 8nm step. Nature 388:386–390 (1997).

Schnitzer MJ, Visscher K, and Block SM. Force production by single kinesin motors. *Nat. Cell Biol.*2:718-723 (2000).

Scholey JM, Heuser J, Yang JT, Goldstein LS. Identification of globular mechanochemical heads of kinesin. *Nature* 338:355-357 (1989).

Seitz A, and Surrey T. Processive movement of single kinesins on crowded microtubules visualized using quantum dots. *EMBO J.* 25:267-277 (2006).

Seitz A, Kojima H, Oiwa K, Mandelkow EM, Song YH, and Mandelkow E. Single-molecule investigation of the interference between kinesin, tau and MAP2c. *EMBO J.* 21:4896-4905 (2002).

Shelanski ML, Gaskin F, and Cantor CR. Microtubule assembly in the absence of added nucleotides. *Proc. Natl. Acad. Sci. U S A* 70:765-768 (1973).

Sinn C. PhD-thesis, Universität Potsdam (2004).

Stracke R, Boehm KJ, Burgold J, Schacht HJ, and Unger E. Physical and technical parameters determining the functioning of a kinesin-based cell-free motor system. *Nanotechnol.* 11:52-56 (2000).

Svoboda K, and Block SM. Biological applications of optical forces. *Annu.Rev. Biophys. Biomol. Struct.* 23:247-285 (1994).

Svoboda K, Schmidt CF, Schnapp BJ, and Block SM. Direct observation of kinesin stepping by optical trapping interferometry. Nature 365:721–727 (1993).

Taniguchi Y, Nishiyama M, Ishii Y, and Yanagida T. Entropy rectifies the Brownian steps of kinesin. *Nat. Chem. Biol*. 1:342-347 (2005).

Thorn KS, Ubersax JA, and Vale RD. Engineering the processive run length of the kinesin motor. J. Cell Biol. 151:1093–1100 (2000).

Tilney L, and Portnoy DA. Actin filaments and the growth, movement, and spread of the intracellular bacterial parasite, *Listeria monocytogenes*. *J. Cell Biol.* 109:1597-1608 (1989).

Tilney LG, Bryan J, Bush DJ, Fujiwara K, Mooseker MS, Murphy DB, and Snyder DH. Microtubules: Evidence for 13 protofilaments. *J. Cell Biol.* 59:267-275 (1973).

Tomishige M, Stuurman N, and Vale RD. Single-molecule observations of neck linker conformational changes in the kinesin motor protein. *Nat. Struct. Mol. Biol* 13:887-894 (2006).

Unger E, Boehm KJ, and Vater W. Structural diversity and dynamics of microtubules and polymorphic tubulin assamblies. *Electron Microsc. Rev.* 3:355-395 (1990).

Vale RD, Reese TS, and Sheetz MP. Identification of a novel force-generating protein, kinesin, involved in microtubule-based motility. *Cell* 42:39-50 (1985).

Vale RD. Direct observation of single kinesin molecules moving along microtubules. *Nature* 380:451-453 (1996).

Vale RD, and Fletterick RJ. The design plan of kinesin motors. *Annu. Rev. Cell Dev. Biol.* 13:745-777 (1997).

Vale RD, and Milligan RA. The way things move: Looking under the hood of molecular motor proteins. *Science* 288:88-95 (2000).

Vale RD. The molecular motor toolbox for intracellular transport. *Cell* 112:467-480 (2003).

Vater W, Boehm KJ, and Unger E. A simple method to obtain brain microtubule protein poor in microtubule-associated proteins. *Acta Histochem. Suppl.* 33:123-129 (1986).

Verhey KJ, Lizotte DL, Abramson T, Barenboim L, Schnapp BJ, and Rapoport TA. Light chain-dependent regulation of Kinesin's interaction with microtubules. *J. Cell Biol.* 143(4):1053-1066 (1998).

Vissher K, Schnitzer MJ, and Block SM. Single kinesin molecules studied with a molecular force clamp. *Nature* 400:184-189 (1999).

Wang HW, and Nogales E. Nucleotide-dependent bending flexibility of tubulin regulates microtubule assembly. *Nature* 435:911-915 (2005).

Weingarten MD, Lockwood AH, Hwo S, and Kirschner MW. A protein factor essential for microtubule assembly. *Proc. Natl. Acad. Sci. U S A* 72:1858-1862 (1975).

Weiss DG, and Maile W. Principles, practice, and applications of video-enhanced contrast microscopy. Electronic Light Microscopy. (ed.) SDM, New York: Wiley-Liss. 105-140 (1992).

Yang JT, Laymon RA, and Goldstein LS. A three-domain structure of kinesin heavy chain revealed by DNA sequence and microtubule binding analyses. *Cell* 56:879-889 (1989).

Yildiz A, Tomishige M, Vale RD, and Selvin PR. Kinesin walks handoverhand. *Science* 303:676–678 (2004).

Acknowledgements

First, I would like to thank Prof. Reinhard Lipowsky and thank Prof. Frieder W. Scheller for the support, patience and guidance throughout this work, and for giving me the chance to do a PhD in Biochemistry.

Many thanks to Prof. Eberhard Unger and Dr. Böhm for introducing me to the world of kinesin, lending me support when ever biochemical questions arose.

Special thanks to my supervisor Dr. Rumiana Dimova for stimulating discussions, critical reviews and comments, time, patience and for her humor.

I thank Dr. Stefan Klumpp for helping me understand some theoretical physics and for translating the terminology of this field for a layman. Furthermore, I thank Dr. Ruben Serral Gracia for the writing this little program that did great work for me. I thank Dr. Gaby Meyer zur Hörste and Dr. Pavel Kraikivsky for the introduction to the world of traps.

Thanks to all former and current members of our MembraneLab and the rest of the Theory-people. Especially I thank Petra Gutjahr, Andrea Grafmüller and Conny Sinn for their friendship and patients. Thanks to my incomparable office mate Said Aranda and to Chris Haluska for making me smile and "get lucky". Furthermore thanks to Vesko Nikolov, Andreas Richter who showed me there is more to the Institute than work.

Many thanks to the members of the molecular cytology group of the IMB-Jena (now FLI-Jena) for companionable freezing in the cold room.

Ein weiterer Dank gilt meinen Freunden. Im speziellen Danke ich meiner Familie für Ihre Unterstützung, Aufmunterung und Hilfe. Grazie mille!